TECHNISCHE UNIVERSITÄT WIEN

DIPLOMARBEIT

Spiking efficiency of electrically stimulated pyramidal cells: a modeling study

zur Erlangung des akademischen Grades

Diplom-Ingenieur

im Rahmen des Studiums

Biomedical Engineering

eingereicht von

Dusan Cvetkovic
Matrikelnummer 01527614

ausgeführt am Institut für Analysis und Scientific Computing
der Fakultät für Mathematik und Geoinformatik der Technischen Universität Wien

Betreuung
Ao.Univ.Prof. Dipl.-Ing. Dr.sc.med. Dr.techn. Dr.rer.nat. Frank Rattay
Dipl.-Ing. Dr.techn. Paul Werginz

Wien, Dezember 2022

Abstract

During electrical stimulation of the pyramidal cell (PC), the spiking efficiency increases from 0 to 1 at the lower threshold and decreases from 1 to 0 at the upper threshold as the stimulus amplitude increases. Spiking efficiency as a function of stimulus amplitude follows a sigmoidal or reverse sigmoidal shape, respectively.

Many modeling studies examine the threshold and origin of spike i.e., action potential (AP) initiation in PCs in relation to different positions and configurations of the stimulation electrode using deterministic models in which the spiking efficiency as a function of the stimulus amplitude reduces to the step function. Fewer studies deal with modeling that includes a stochastic component in the model. Here, this was achieved by injecting a maximum-sodium-conductance-dependent noise current into each compartment with an active membrane. The spiking efficiency was examined in relation to different positions and configurations of the stimulation electrode, where the threshold and origin of AP initiation were observed, and the geometric and electrophysiological properties of the model were changed. Dynamic range (DR) and relative spread (RS) were used to measure the increase in spiking efficiency with a stimulus intensity. A simplified geometry of the PC was used, with two basic electrophysiological configurations. The first is a standard model that contains three voltage gated active channels: high-threshold $Na_v1.2$ and low-threshold $Na_v1.6$ sodium and fast K_v potassium channels. The second is an extended model that additionally contains two potassium channels, slow non-inactivating potassium current K_m and calcium dependent K_{Ca}, then high-voltage activated Ca_v channel and internal calcium concentration mechanism Ca_{cm}.

The following can be concluded from the simulation experiments in this thesis. In general, a larger DR is expected by stimulating more excitable parts of the PC, with a few exceptions. It seems that when stimulating highly excitable parts of the PC, there is a competition between responsiveness and noisiness, which can reduce DR. DR is the largest between the unmyelinated axon and the first node of Ranvier, and the smallest at the dendrite. In addition to the geometric and electrophysiological properties of the cell, the activating function and the origin of AP initiation should also be considered for the prediction of DR. Additional channels in the extended model have almost no effect on the threshold, and a slightly larger, but still small, effect on the DR.

Kurzfassung

Während der elektrischen Stimulation der Pyramidenzelle (PC) steigt die Feuerungswahrscheinlichkeit von 0 auf 1 an der unteren Schwelle und fällt von 1 auf 0 an der oberen Schwelle, wenn die Stimulusamplitude zunimmt. Die Feuerungswahrscheinlichkeit als Funktion der Stimulusamplitude folgt einer sigmoidalen bzw. umgekehrt sigmoidalen Form.

Viele Modellierungsstudien untersuchen die Schwelle und Entstehungsort des Aktionspotentials (AP) in PCs in Bezug auf verschiedene Positionen und Konfigurationen der Stimulationselektrode (wie in dieser Arbeit), aber unter Verwendung deterministischer Modelle, in denen die Feuerungswahrscheinlichkeit als Funktion der Stimulusamplitude auf die Sprungfunktion reduziert wird. Weniger Studien befassen sich mit der Modellierung, die eine stochastische Komponente in das Modell einbezieht. Hier wurde dies erreicht, indem in jedes Segment mit einer aktiven Membran ein von der maximalen Natriumleitfähigkeit abhängiger Rauschstrom injiziert wurde. *Dynamic range* (DR) und *relative spread* (RS) wurde verwendet, um die Erhöhung der Feuerungswahrscheinlichkeit mit zunehmender Stimulusintensität zu messen. Es wurde eine vereinfachte Geometrie der PC mit zwei grundlegenden elektrophysiologischen Konfigurationen verwendet. Das erste ist ein Standardmodell, das drei spannungsgesteuerte aktive Kanäle enthält: hochschwellige $Na_v1.2$ und niederschwellige $Na_v1.6$ Natrium- und schnelle K_v Kaliumkanäle. Das zweite ist ein erweitertes Modell, das zusätzlich zwei Kaliumkanäle enthält, einen langsamen, nicht inaktivierenden Kaliumstrom K_m und ein calciumabhängiges K_{Ca}, dann einen hochspannungsaktivierten Ca_v-Kanal und einen internen Calciumkonzentrationsmechanismus Ca_{cm}.

Folgendes kann aus den Simulationsexperimenten in dieser Arbeit geschlossen werden. Im Allgemeinen wird ein größeres DR erwartet, indem erregbarere Teile des PC stimuliert werden, mit wenigen Ausnahmen. Es scheint, dass es bei der Stimulierung hocherregbarer Teile des PC zu einem Wettbewerb zwischen Reaktionsfähigkeit und Rauschen kommt, was DR reduzieren kann. DR ist zwischen dem nicht-myelinisierten Axon und dem ersten Ranvier-Node am größten und am Dendriten am kleinsten. Neben den geometrischen und elektrophysiologischen Eigenschaften der Zelle sollten auch die sogenannte *activating function* und Entstehungsort des AP für die Vorhersage von DR berücksichtigt werden. Zusätzliche Kanäle im erweiterten Modell haben fast keinen Einfluss auf den Schwellenwert und einen geringen Einfluss auf das DR.

Acknowledgments

First of all, I would like to express my deep gratitude to my supervisor, Prof. Frank Rattay, who introduced me to and got me interested in the world of neuroscience. I liked his approach to supervision, where he was always there to help or offer guidance, but he also gave me a lot of freedom in terms of directing the further development of the thesis.

I am also very thankful to Dr. Paul Werginz for all his support, help, useful advice and time invested. Communication with him was excellent and his suggestions made the models and simulations better and more efficient.

I would also like to thank Dr. Andreas Fellner who, together with Prof. Rattay, introduced me to the world of computer simulations, which I immediately became interested in. Much of the knowledge and ideas acquired from him contributed to this work, especially at its beginning.

Thanks should also go to the employees from the dean's office of the Faculty of Mathematics and Geoinformation who were very kind and helpful with organizational matters.

I owe a debt of gratitude to my dear family, who encouraged me to study in Austria and supported me throughout my studies. I also owe a great deal to my closest friends who believed in me and made the past years more joyful.

Finally, the most special thanks to my girlfriend Fatima, who was my companion throughout this bachelor-master's journey. Not only did I have her enormous emotional support and love, but our conversations and idea sharing were very productive and valuable in helping me to shape and refine this research.

List of Abbreviations

(-)	Cathodic
(+)	Anodic
(+/-)	Anodic followed by cathodic
AIS	Axon initial segment
AP	Action potential; spike
ATP	Adenosine triphosphate
CNS	Central nervous system
DR	Dynamic range
HH	Hodgkin-Huxley
PC	Pyramidal cell
PNS	Peripheral nervous system
RGC	Retinal ganglion cell
RS	Relative spread

Contents

1 Introduction to Morphology and Physiology of Nerve Cells

This section serves for a better understanding of the nervous system in general, nerve cells and their anatomy, especially pyramidal cells, and the understanding of the mechanisms responsible for the creation and transmission of signals.

1.1 Nervous System

The nervous system is a complex part of the body through which electrical signals are rapidly transmitted through the body. The basic building block of the nervous system are nerve cells, also called neurons. There are more than 100 billion neurons in the human brain (Purves, et al., 2005). They are connected and form a network (Rattay, 1990). These networks can be on the one hand simple, consisting only of the same type of nerve cells. Such simple and undifferentiated neurons are found in primitive invertebrates. On the other hand, neurons in humans are highly differentiated in their shape and function according to their purpose in the body (Rattay, 1990).

According to Ferrante (2018) two main parts of the nervous system are central nervous system (CNS) and peripheral nervous system (PNS). The CNS consists of the brain and spinal cord and the PNS consists of the spinal and cranial nerves that branch off from the spinal cord and spread through all parts of the body. Spinal cord connects the brain with the PNS and therefore with the rest of the body. Spinal cord transmits motor information from the CNS to the PNS. In the opposite direction it transmits sensory information from the PNS to the CNS.

1.2 Neurons

As already mentioned in section 1.1 neurons are the smallest building block of the nervous system. According to their purpose and direction of signal transmission

neurons in PNS are divided into motor neurons and sensory neurons (Rattay, 1990). Motor neurons, also referred to as efferent neurons, are responsible for the transfer of information from the CNS to the body whereas sensory neurons, also referred to as afferent neurons, are responsible for the transfer of information from the body to CNS.

Neurons consist of a cell body called soma and one or multiple extensions, which are also called processes, attached to it (Rattay, 1990). Extensions can vary greatly in their number and geometry depending on the type of nerve cell. (Purves, et al., 2005). Neurons with only one extension are called unipolar neurons. There are also bipolar neurons, which have two extensions and multipolar neurons which have more than two extensions. There are two types of extensions called axon or nerve fiber and dendrite. Axon is responsible for transferring outgoing information up to one meter away from the soma and it is usually longer than other extensions (Rattay, 1990).

Referring to Ferrante (2018) dendrites are usually shorter than axons. They can be of different shapes and lengths and can branch out. Their main task is receiving information from other neurons via synapses.

Figure 1 shows a neuron consisting of a cell body called a soma, a dendrite, a myelinated axon and an axon terminal. The direction of signal propagation is also shown, which generally starts from the area of dendrites, continues through the soma and axon, and reaches the axon terminal, where the signal is transmitted to other cells via synapses.

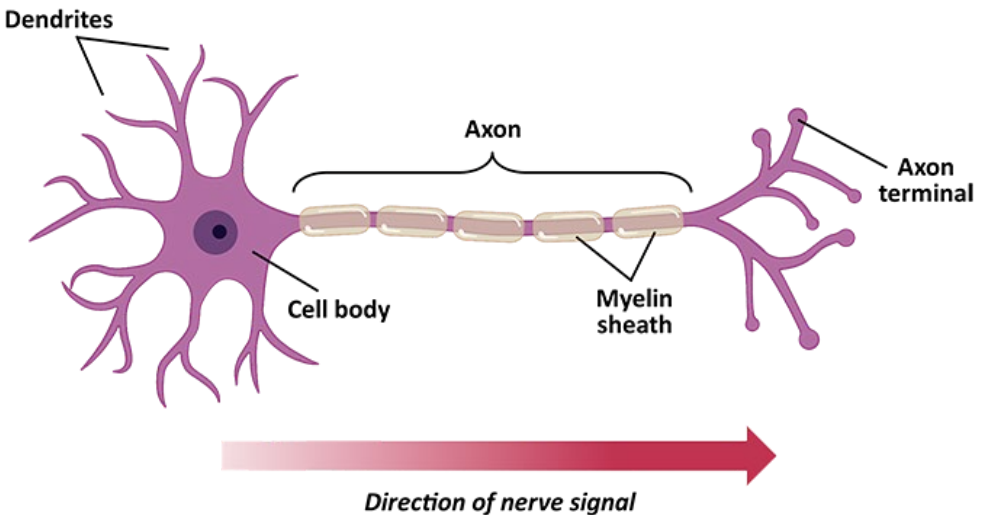

Figure 1: Anatomy of neuron. The cell body called the soma can be seen on the left. Also represented are dendrites. Going to the right, the axon is shown, and it is coated with myelin. The axon terminal is shown all

the way to the right. The red arrow indicates the usual direction of signal propagation. Figure form National Institute of Neurological Disorders and Stroke (n.d.).

1.2.1 Myelin

Unless otherwise noted, the following description of the myelin is based on descriptions from books of Bolsover, et al. (2003) and Ferrante (2018).

Myelin is an insulating sheath around the axon that enables the rapid transmission of action potentials through the nerve cell. Most human nerve cells are covered with myelin. Myelin is made by glial cells, also known as Schwann cells, which wrap around axons, often many times. Myelin is essentially a fatty sheath around the axon that serves as an insulator. It does not cover the entire axon, but is periodically interrupted by nodes of Ranvier, or short nodes. The node is a short part of the axon ($1 - 3\ \mu m$) that is not covered with myelin and its cell membrane is in direct contact with the extracellular fluid. Up to the next node, the axon is covered with myelin and that part is called the internode. The length of the internode is much longer than the length of the node. In myelinated neurons, the length of the internode is about 100 times the diameter resulting in internodal lengths up to $2\ mm$ (Rattay, 1990).

Action potential (AP) can be initiated by electrical stimulation in the membrane of the node. This is due to the large number of voltage-gated sodium channels located there. When an AP occurs, voltage-gated sodium channels open and the transmembrane potential increases. The charge created inside the cell cannot leave the cell until the next node due to insulator properties of myelin. There the membrane depolarizes to the threshold and the voltage-gated sodium channels open and a new action potential occurs. The same process is repeated from node to node. In this way, the AP jumps from node to node, instead of being conducted continuously through the axon, which enables faster AP transmission.

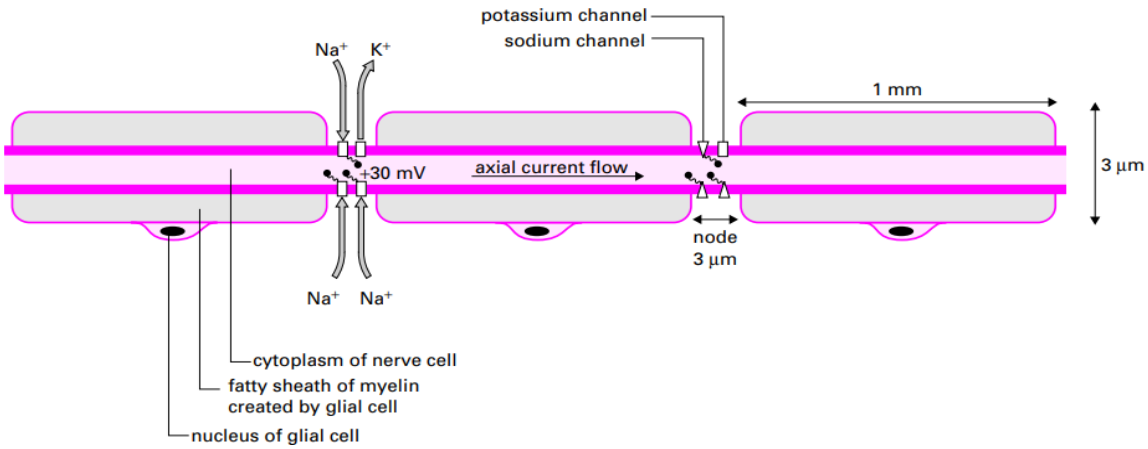

Figure 2: Myelinated axon. Two nodes and three internodes are visible. Figure from Bolsover, et al. (2003).

Figure 2 shows three internodes covered with myelin, where the Schwann cell nucleus is also visible, and two nodes containing voltage-gated ion channels.

1.2.2 Synapses

Synapses are located at the end of the axon terminal region. Their role is to transmit information between two neurons or between neuron and muscle fibers or glands (Rattay, 1990). Most often, the terminal presynaptic region of the axon makes "contact" with the postsynaptic dendrite but can also rarely with the soma (Purves, et al., 2005). The word contact is put in quotation marks because for many synapses there is no physical contact between the presynaptic and postsynaptic region. Instead, signals are transferred via a narrow gap called synaptic cleft between presynaptic and postsynaptic cells. Special molecules are secreted into the synaptic cleft from the presynaptic terminal and bind to receptors in the postsynaptic region. There are two types of synapses, chemical and electrical (Purves, et al., 2005). Chemical synapses are responsible for this type of synaptic transmission. A rarer type of synaptic transmission is carried out through electrical synapses. In electrical synapses, the presynaptic and postsynaptic regions are very close to each other and are connected via gap junctions, which allow passive flow of ionic current.

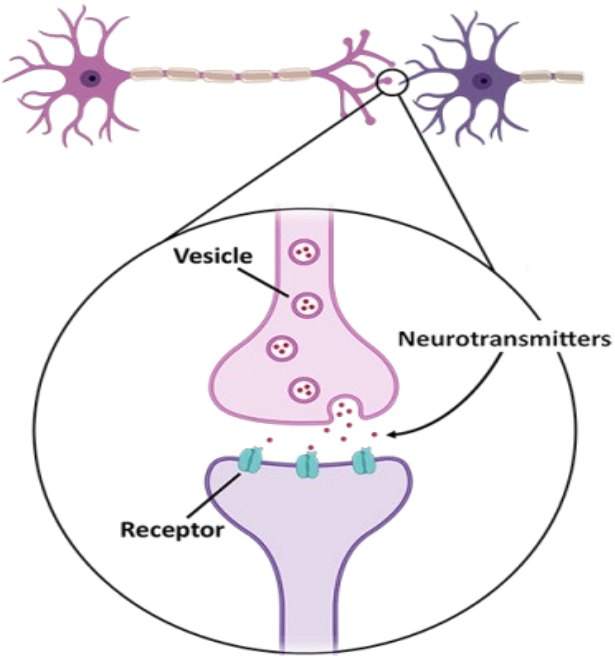

Figure 3: A chemical synapse between the axon terminal of one neuron and the dendrite of another neuron. The signal is transmitted via neurotransmitters. Figure from National Institute of Neurological Disorders and Stroke (n.d.).

Figure 3 shows a chemical synapse between the axon terminal of one neuron and the dendrite of another neuron, where a neural signal passes from one neuron to another. When the signal reaches the axon terminal of the first cell, the neurotransmitter is released into the synaptic cleft. Neurotransmitters bind to the receptors of the next cell, so it is possible for the signal to be transmitted further through that cell. However, note that in general the input signal is an AP while the postsynaptic signal is of much smaller amplitude.

1.2.3 The Cell Membrane

Cell membrane in this section is described according to its description from the book by Ferrante (2018).

The neuron membrane, like other cells membrane, is composed of a phospholipid bilayer. As the name suggests, it consists of two layers of phospholipids. A phospholipid has a hydrophilic head that attracts water and a hydrophobic tail that repels water. The hydrophobic layer does not allow ions to pass through the membrane. This leads to a difference in the concentration of ions on both sides of the cell membrane, which is also called a concentration or chemical gradient. Due to the small thickness of the cell membrane, ions outside the cell and ions inside the cell act on each other. Since ions are charged particles, this difference in concentration leads to the generation of voltage. This voltage is called the transmembrane voltage and in the resting state it is about $-70\ mV$.

The phospholipid bilayer has a three-layered structure in which the two outer hydrophilic layers are conductors, and the inner hydrophobic layer is non-conductive. This structure is responsible for capacitive properties of the cell membrane.

Many protein structures are embedded in the phospholipid bilayer that form channels through which ions can pass. These structures are responsible for resistive properties of the cell membrane. So, one can say that electrical characteristics of the phospholipid bilayer are equivalent to a resistor and capacitor in parallel connection.

1.2.4 Ion Channels

The ion channels in this section are described as in the books by Bolsover, et al. (2003) and Ferrante (2018).

Given that there are several different ion channels, they electrically behave like resistors connected in parallel. Ion channels are such that they do not pass all ions, on the contrary, they can pass one or multiple ions according to their dimensions and charges. The movement of charged particles, unlike non-charged particles, is not only affected by the concentration gradient, but also by the direction and strength of the transmembrane voltage.

There are two types of ion channels, nongated and gated. Nongated channels are continuously open. Gated channels are occasionally open. There are again two types of gated channels, voltage-gated and ligand-gated. The conformation of voltage gated channels is controlled by the membrane voltage, while in ligand gated channels the binding of a specific ligand controls the conformation.

Figure 4 shows a voltage-gated sodium channel and how it works. Its gating mechanism contains activation and inactivation gates. The activation gate opens when the depolarization exceeds a certain threshold and an influx of sodium ions occurs. After about 1 ms, the inactivation gate closes the channel and sodium ion influx stops. After this cycle, the channel remains closed for some time before the next depolarization can open the activation gate again. In Figure 4 inactivation gate is shown as an inactivation plug.

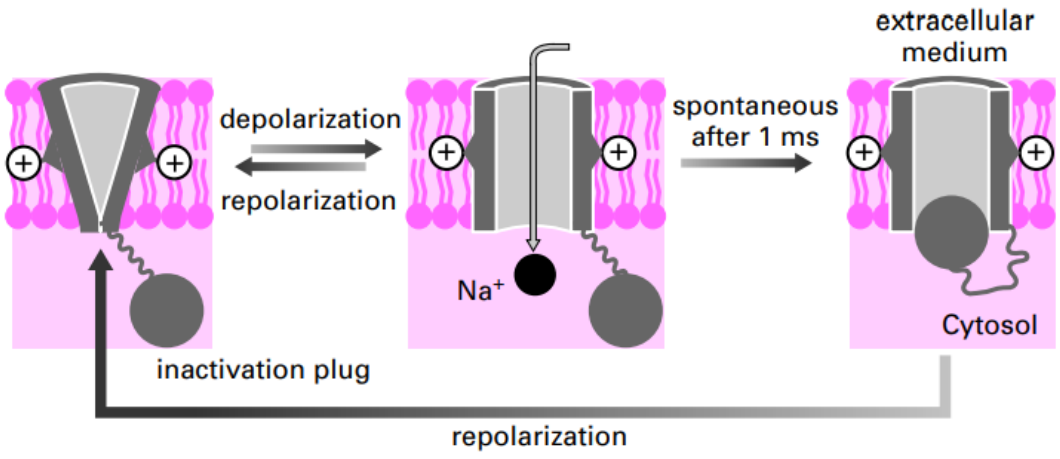

Figure 4: Voltage-gated sodium channel. An influx of sodium ions occurs if the depolarization exceeds a certain threshold. After 1 ms, the inactivation gate closes, which is represented by a gray ball that clogs the channel. After that, repolarization occurs, the channel remains closed and the next depolarization can open the activation gate only after a certain time. Figure from Bolsover, et al. (2003).

1.3 Action Potential

The sources of information for the description of action potential in this section are the books from Rattay (1990), Kaniusas (2012) and Ferrante (2018).

Action Potential (AP) is the rapid rise of transmembrane potential. AP is possible only in excitatory cells that, in addition to nongated, have gated ion channels. AP is responsible for the rapid transfer of information through neurons and therefore through the entire body.

While the cells are at rest, only nongated channels are opened, most of which are potassium channels. Due to the concentration gradient of potassium ions, of which there are about forty times more intracellular than extracellular, potassium ions tend to leave the cell. Since potassium ions are positively charged, and the inside of the cell is negatively charged, the electrical gradient acts in the opposite direction. Unlike potassium ions, the ratio of extracellular to intracellular concentrations of sodium ions is twelve to one. In this case, the chemical gradient drives sodium ions into the cell. As already said above, the inside of the cell is more negative than the outside. Since sodium ions are positively charged, the electrical gradient that acts on them also drives them inward. Chemical and electrical gradients determine the direction of ion movement in case of sudden opening of voltage gated channels. In case of opening of voltage gated potassium channels, ions would move in the direction of the net difference of those two gradients. In the case of voltage gated sodium channel opening, both chemical and electrical gradients would drive sodium ions inward.

When the electrical and chemical gradients are equal, an equilibrium is reached in which the influx of ions equals the efflux. Influx means inward movement of ions or molecules into a cell through the cell membrane, and efflux is the opposite. The transmembrane potential that then arises is called the equilibrium potential, and for a specific ion it can be calculated using the Nernst equation, which calculates the equivalent voltage gradient based on the concentration of the specific ion inside and outside of the cell:

$$E(ion) = \frac{RT}{ZF} \ln \frac{[outside]}{[inside]} \qquad (1.1)$$

$E(ion)$ is the equilibrium potential of a particular ion, R is the gas constant, T is the temperature in Kelvin, Z is the valence of the ion, and F is the Faraday constant. The square brackets indicate the ion concentration outside and inside.

Since the total membrane potential is affected by more than one ion, the Nernst equation is not sufficient. Therefore, the Goldman-Hodgkin-Katz equation is used, which, in addition to the concentration of ions on one and the other side of the cell membrane, also considers the permeability of ions, which is proportional to the number of channels through which ions can pass:

$$Vm = \frac{RT}{F} \ln \frac{P_K[K^+]_o + P_{Na}[Na^+]_o + P_{Cl}[Cl^-]_i}{P_K[K^+]_i + P_{Na}[Na^+]_i + P_{Cl}[Cl^-]_o} \qquad (1.2)$$

V_m is transmembrane potential. As with the Nernst equation, the square brackets represent the ion concentration, and the letters o and i in the subscript indicate whether the concentration is outside or inside the cell, respectively. P is the permeability of a certain ion. The Goldman-Hodgkin-Katz equation considers sodium, potassium and calcium ions.

Transmembrane resting potential is $-70\ mV$. The equilibrium potential of potassium ions is $-98\ mV$, which is much closer to the transmembrane resting potential than that of sodium ions, whose equilibrium potential is $+67\ mV$. The reason for this is the much higher permeability of potassium ions than sodium ions. Since the equilibrium potential of both sodium and potassium ions is different from the transmembrane resting potential, the ions move in the direction of their chemical gradient. If this movement of ions continued without any correction mechanisms, the transmembrane potential would reach a value of $-30\ mV$. In that case, the cell would not be excitable and would not be able to generate an AP. Sodium and potassium pumps return ions against their chemical gradient and use ATP for this. The pump pumps out three sodium ions and pumps two calcium ions into the cell. In this way, the transmembrane resting potential of $-70\ mV$ is maintained.

The AP consists of three stages. These are depolarization, repolarization and hyperpolarization. In order to cause an AP, the transmembrane potential must reach the threshold value required for depolarization. Gating mechanisms enable these three phases and therefore AP. Voltage gated sodium channels have 2 gates, an activation and an inactivation gate. Voltage gated potassium channels have only an activation gate.

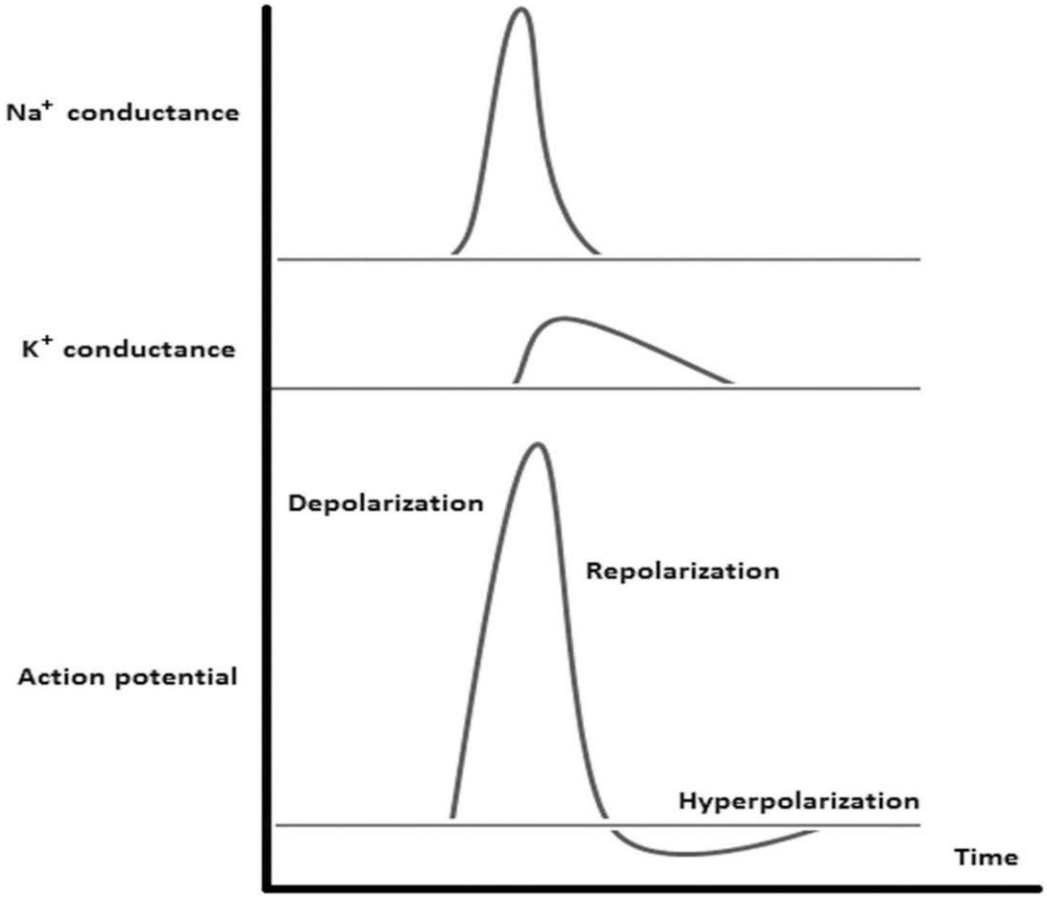

Figure 5: Top: sodium conductance as a function of time. During depolarization, the sodium ion conductance increases rapidly, reaching a maximum that is also the maximum of the action potential until the inactivation gate stops it. Middle: potassium conductance as a function of time. Conductance of potassium ions increases with a delay compared to sodium ions. It leads to repolarization. At one point, it even exceeds the transmembrane resting potential and leads to hyperpolarization. Bottom: action potential (transmembrane potential) as a function of time. Three phases of the action potential can be seen, namely depolarization, repolarization, and hyperpolarization. The thinner horizontal line represents the transmembrane resting potential. Figure and description from Ferrante (2018).

As said, depolarization is induced when the transmembrane voltage reaches a certain limit. Then the activation gates of the voltage gated sodium channels open and sudden influx of sodium ions into the cell occurs. During depolarization, the membrane becomes the most permeable to sodium ions. The permeability of sodium ions becomes 12 times higher than the permeability of potassium ions and even 5000 times higher than in the resting state. Accordingly, the transmembrane voltage increases, its polarity changes from negative to positive and goes towards sodium ion equilibrium potential. Transmembrane potential does not reach value of sodium ion equilibrium because after about 1 ms, when the transmembrane voltage reaches its peak value of about $+30\ mV$, the inactivation gates stop sodium influx, and the potassium activation gates open and potassium efflux occurs. The way voltage-gated sodium channel works is shown in Figure 4. From that moment, repolarization begins and the transmembrane voltage returns to its resting state. The efflux of potassium ions brings the

transmembrane potential to its resting state and this is where the repolarization phase ends. Efflux of potassium ions does not end there because voltage gated potassium channels remain open for several ms and hyperpolarization occurs. The value of the transmembrane voltage exceeds the value of the resting potential and reaches a value of about $-90\ mV$. Although at this moment the voltage gated sodium channels are in their resting state, a fairly large depolarization is required to trigger a new AP. This phenomenon allows the transmission of AP in one direction. Finally, the voltage gated potassium channels return to their resting state and the transmembrane voltage reaches its resting value.

This whole process can be seen in Figure 5.

1.4 Pyramidal Cell

Pyramidal cells (PC), also referred to as pyramidal neurons, are found in the six-layered neocortex, the majority part of the cerebral cortex of all mammals. They make up about $70-85\%$ of neurons there. They play a role in many advanced cognitive functions, but also in driving muscles, etc. They consist of a triangular or cone-shaped soma, two types of dendrites, apical and basal, and an axon that often has collateral branches. Axons can be very long, as in pyramidal cells in layer 5 of the motor cortex that drive muscles. Apical dendrites are usually longer and emerge in a conical fashion from the pointy end of the soma. Basal dendrites are usually shorter and emerge from the basal end of the soma. (Bekkers, 2011; Bitanihirwe & Woo, 2021)

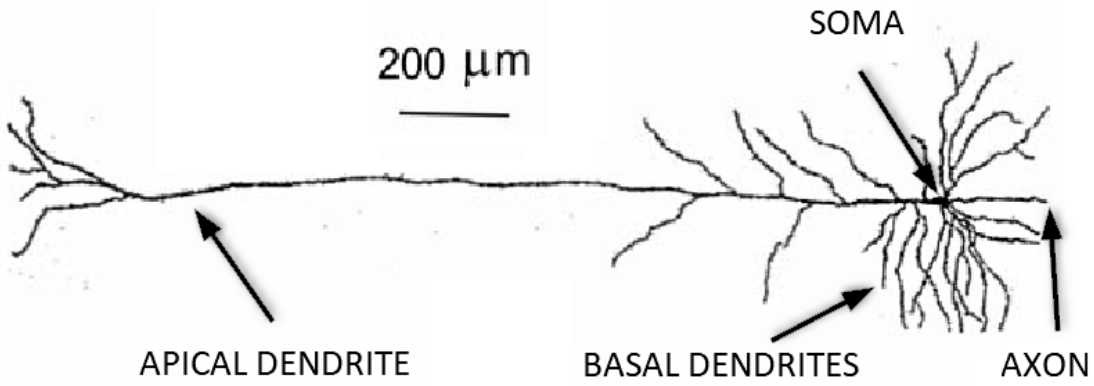

Figure 6: Neocortical layer 5 pyramidal cell. Camera lucida drawing. Figure modified from LaBerge (2005).

First described PCs are “giant” PCs in the brain, called Betz cells (named after Vladimir Alekseyevich Betz), which is a group of neurons in the layer 5 of the medial sensory-motor cortex and they have diameters of $70-100\ \mu m$, which makes them

the largest neurons in the cerebral cortex (Bitanihirwe & Woo, 2021). Neocortical layer 5 PC can be seen in Figure 6.

1.4.1 Electrical Stimulation of Pyramidal Cells

As already mentioned above, pyramidal cells located in the cortex have different roles, from contribution in cognitive to motor functions. Thus, artificial electrical stimulation of PCs has the potential for various applications which could restore lost functions or treat disease symptoms. For example, in the case of blindness where both photoreceptors and all other retinal cells are damaged (lost its function) one option for vision restoration is electrical stimulation of pyramidal cells in the visual cortex (Fried & Lee, 2016; Liu, et al., 2022). Another application of cortex electrical stimulation could be reduction of seizures in patients with epilepsy (Foutz & Wong, 2022) or reduction of Parkinson's disease symptoms (Valverde, et al., 2020). Furthermore, cortical electrical stimulation may be generally used for the improvement of cognitive and motor function in the aging brain (Summers, et al., 2016).

2 Introduction to Nerve Cell Modeling

In order to get insight in modeling of the nerve cells, the Hodgkin-Huxley model, which serves as the basis for many other nerve cell models, is presented. Additionally, two ways of stimulating modeled cells (intracellular and extracellular electrical stimulation) are described.

2.1 Hodgkin-Huxley Model

In order to better understand the mechanisms used later in this thesis, it is important to understand the basics of the Hodgkin-Huxley (HH) model (Hodgkin & Huxley, 1952). The kinetics of most of the channels used in this thesis is based on this model.

Back in 1952, Alan Hodgkin and Andrew Huxley created a mathematical model that describes the ionic mechanisms that further describe electrical behavior of the membrane and thus are responsible for the creation and conduction of the action potential in squid giant axons. In 1963, they received the Nobel Prize in Physiology or Medicine for this work[1].

The electrical circuit presented in Figure 7 describes the electrical behavior of the nerve cell membrane. There are two ways for current to pass through the membrane (Hodgkin & Huxley, 1952). The first is through charging the membrane capacity. The second is that the ions pass through resistors in parallel with the capacitor. Thereby almost all the current injected into the cell passes the membrane in the form of ionic currents as pointed out by Rattay (1990). Only short and sharp spikes of current at the beginning and at the end of the injection pass the membrane in the form of capacitive currents. That is why great attention is paid to ionic channels in modeling. This can be seen in the four main equations of the Hodgkin-Huxley model.

[1] https://www.nobelprize.org/prizes/medicine/1963/summary/

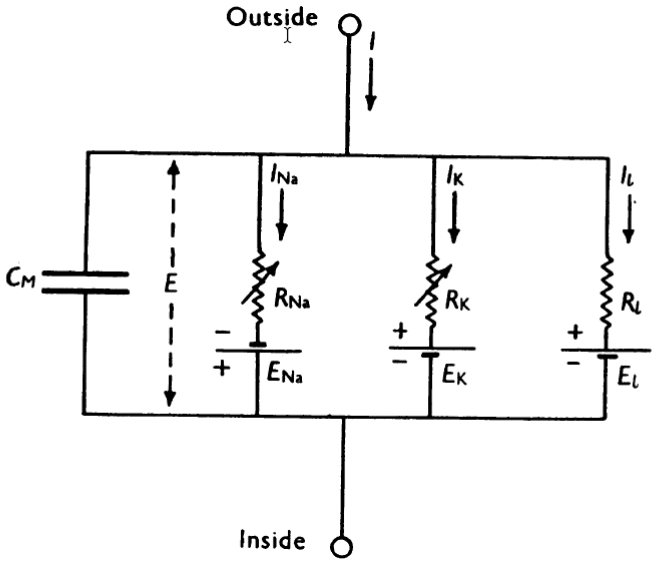

Figure 7: Electrical circuit equivalent for a patch of cell membrane. Conductances for sodium, potassium and leakage channels are given as $g_{Na} = 1/R_{Na}$, $g_K = 1/R_K$, and $g_L = 1/R_L$, where g_{Na} and g_K vary with time and membrane potential. Other components are constant. Figure and description from Hodgkin & Huxley (1952).

The equations that fully describe the Hodgkin-Huxley model are taken from the book written by Rattay (1990):

$$\dot{V} = [-g_{Na}\, m^3\, h\, (V - E_{Na}) - g_K\, n^4\, (V - E_K) - g_L\, (V - E_L) + i_{st}]/c \tag{2.1}$$

$$\dot{m} = [-(\alpha_m + \beta_m)m + \alpha_m]k \tag{2.2}$$

$$\dot{n} = [-(\alpha_n + \beta_n)n + \alpha_n]k \tag{2.3}$$

$$\dot{h} = [-(\alpha_h + \beta_h)h + \alpha_h]k \tag{2.4}$$

V is the reduced voltage, which represents the difference between the intracellular and extracellular potential, reduced by the resting voltage of the cell. The voltage generated by the different concentration of ions on both sides of the membrane is given as E_{Na} and E_K for sodium and potassium ions, respectively, while E_L represents the leakage voltage. The units of all voltages are given in mV. Maximum conductances are given as g_{Na}, g_K, and g_L for sodium, potassium, and leakage channels, respectively, and the units are $k\Omega^{-1}cm^{-2}$. Stimulating current density i_{st} is given in $\mu A/cm^2$. The

capacitance of the membrane per cm^2 is c and is given in $\mu F/cm^2$. The opening probabilities of ion channels are given as m, n and h, while α and β are voltage-dependent opening and closing rates. (Hodgkin & Huxley, 1952; Rattay, 1990)

There appear to be two main differences between the original Hodgkin-Huxley equations and the equations from the book by Rattay (1990). The first difference is that by Rattay, in order to be independent of the geometric parameters, instead of the currents present in the original Hodgkin-Huxley equations, the currents passing through the 1 cm^2 of the membrane were calculated. In this way, all currents become current densities, and capacity becomes capacity through cm^2. Second difference is that by Rattay there is an additional coefficient k that multiplies the right side of the equations for the gating variables m, n and h. Bearing in mind that the experimental temperature used in the Hodgkin-Huxley model was 6.3 degrees of Celsius (Hodgkin & Huxley, 1952), the temperature coefficient k (also referred to as thermic coefficient) was needed to correct the model in relation to the temperature change. The thermal coefficient can be calculated as in the following equation:

$$k = 3^{0.1T-0.63} \tag{2.5}$$

where T represents the temperature in Celsius. From the equation for k, it can be seen that at a temperature of $T = 6.3\,°C$, k equals 1, which brings us to the original equations of Hodgkin and Huxley. Since Hodgkin and Huxley saw that all gating processes in the giant squid axon react to temperature steps with the same sensitivity, they introduced a special constant $Q_{10} = 3$, which accelerates the membrane behavior of the squid axon membrane for an increase in temperature of 10°C.

2.2 Electrical Stimulation

During the stimulation of cells that are excitable (e.g., neurons) significant changes in the transmembrane voltage may occur in relation to the transmembrane resting voltage. In relation to whether the threshold was reached during the stimulation or not, the changes in the transmembrane voltage take place differently (Kaniusas, 2012):

- In the case when the cell is stimulated so that the threshold is not reached, where the transmembrane voltage becomes higher than the resting voltage, but lower than the threshold, the membrane reacts passively to the stimulation. This is called subthreshold stimulation.
- On the contrary, if the transmembrane voltage during stimulation reaches the threshold or even exceeds it, the membrane reacts actively to the stimulation.

In this case, the membrane generates an action potential. This is called above-threshold stimulation.

When the cell membrane is stimulated, there is a net flow of ions, into or out of the cell. At the point of ion flow, charge separation across the membrane is disturbed (Kaniusas, 2012). As a result, there is a change in the polarization of the membrane, and depolarization or hyperpolarization can occur.

Two types of artificial nerve cell stimulation are present in this thesis. These are intracellular and extracellular electrical stimulation.

2.2.1 Intracellular Electrical Stimulation

Intracellular electrical stimulation in this section is described according to its description by Kaniusas (2012).

During the artificial injection of stimulation current in e.g., axon, a specific voltage distribution along the axon axis is caused by currents flowing through the cell membrane outside the cell.

Upon injection of positive stimulation current, excitatory stimulation occurs. In the places where the current outflows the axon membrane, depolarization occurs. With subthreshold stimulation, the response of the membrane to the stimulus is passive and follows an exponential pattern. This can be seen in Figure 8c for a constant excitation stimulus at time $t<0$. If the stimulus is long enough or strong enough that the transmembrane voltage at a certain location of the membrane reaches or exceeds the threshold, an action potential occurs at that location. Its duration is independent of the duration of stimulation. This can be seen in Figure 8c when $t>0$.

If a negative stimulation current is injected, hyperpolarization of the cell membrane occurs. As with subthreshold positive stimulation, the cell membrane response is passive and exponential in this case as well. In this case, the length of hyperpolarization depends on the length of the stimulus. This can be seen in Figure 8c. Also, the length of depolarization with a subthreshold positive stimulus depends on the stimulus duration, which is not shown in Figure 8c.

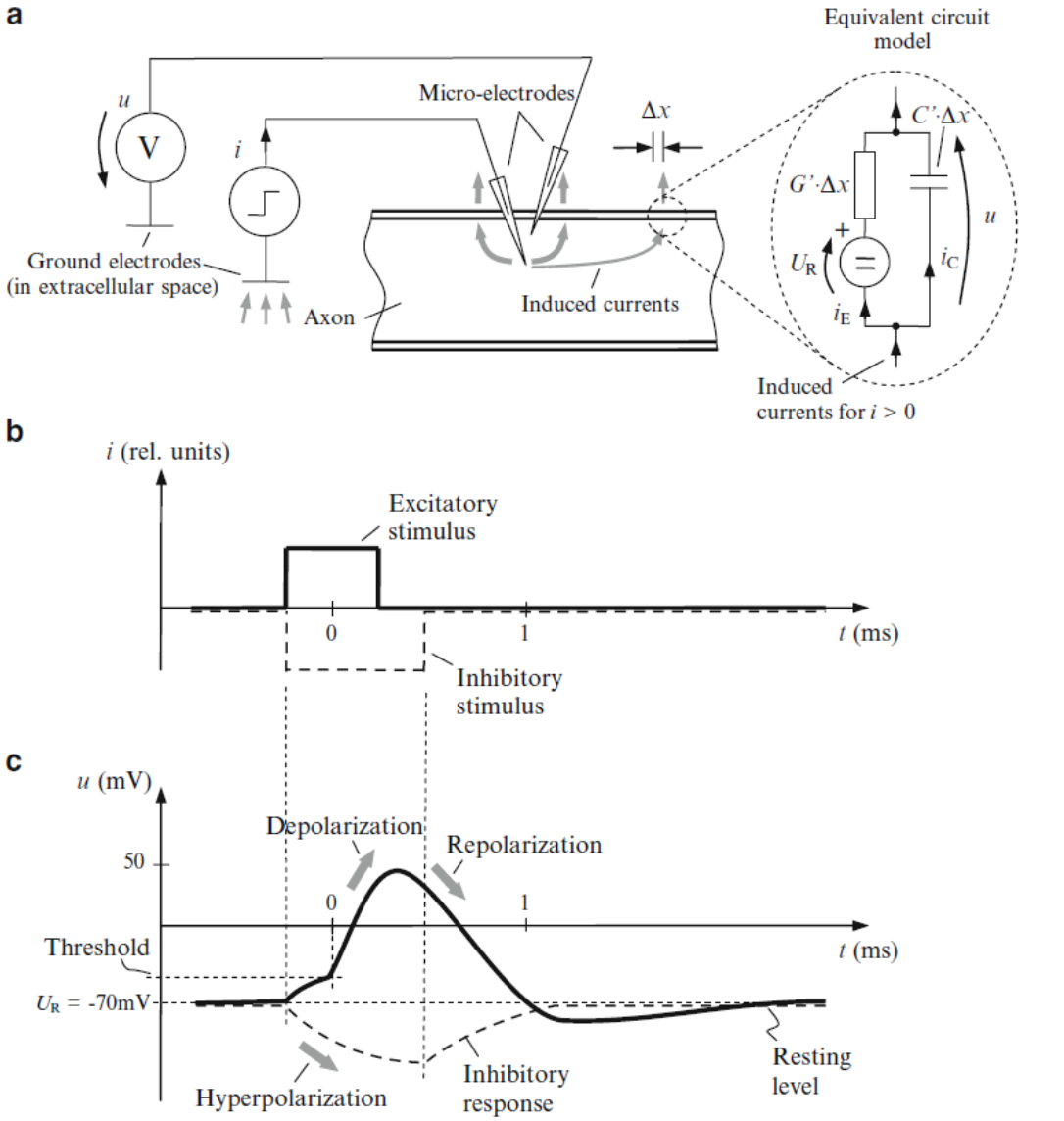

Figure 8: Intracellular stimulation of an axon. (a) Stimulating current i is injected into the cell, while the transmembrane voltage is measured at the same time. The right sub-figure shows the equivalent circuit for the passive response of the membrane. The current i_C represents the capacitive current, while the current i_E represents the electric ionic current. (b) Excitatory and inhibitory intracellular rectangular stimulus. (c) Transmembrane voltage u for an excitatory intracellular stimulus that is depolarizing and above threshold. Transmembrane voltage is also presented for an inhibitory intracellular stimulus that leads to hyperpolarization and shows a passive response of the membrane. Figure and description from Kaniusas (2012).

2.2.2 Extracellular Electrical Stimulation

If not stated differently, the description of the extracellular electrical stimulation is based on the book from Rattay (1990).

Excitatory extracellular stimulation generally requires a stimulus of the opposite sign (negative (cathodal) current) than excitatory intracellular stimulation. It is also possible to produce an action potential with strong positive (anodal) currents. Since in this thesis a monopolar microelectrode is used to stimulate the cell, it is necessary to understand the influence of the monopolar electrode on the extracellular potential.

A practical example is presented here for a better understanding of the effects of extracellular stimulation. The spherical microelectrode is placed at a distance z from the axon, while the ground electrode is relatively far from this electrode. Therefore, the distance z and the shape of the stimulation signal affect the response of the membrane. Assuming that the extracellular medium is homogeneous with a specific resistance of $0.3\ k\Omega \cdot cm$ and a square current pulse is used for stimulation, the sharp rising and falling edges of the used signal are not significantly disturbed by the cell membrane around the electrode, the extracellular potential can be approximated by ohmic resistance via the equation:

$$V_e = \frac{\rho_e I_{el}}{4\pi r} \tag{2.6}$$

where V_e is the extracellular potential, ρ_e is specific ohmic resistance of $0.3\ k\Omega \cdot cm$, $I_{el}(t)$ is the electrode current and the distance to the electrode is represented by r. It is obvious that the extracellular potential is inversely proportional to the electrode distance, i.e., proportional to $1/r$ where $r = \sqrt{x^2 + z^2}$ which can be seen in Figure 9.

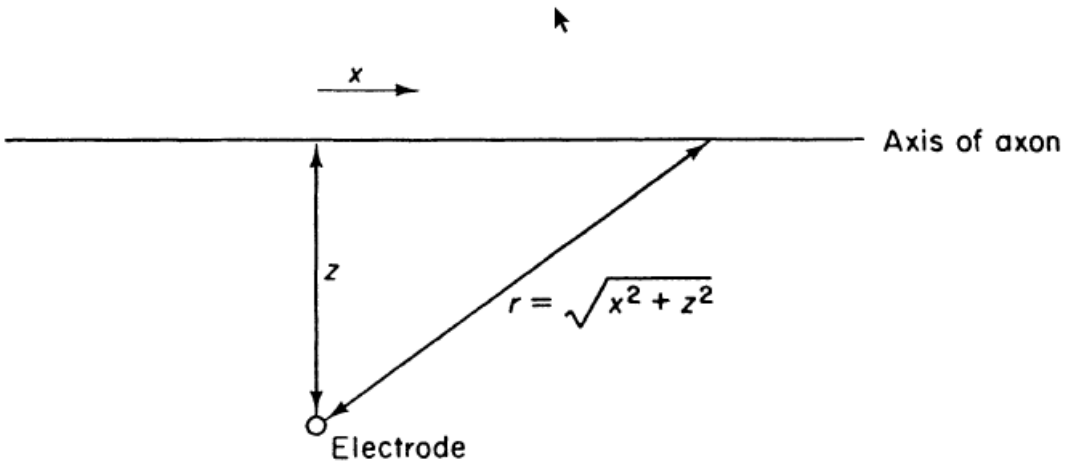

Figure 9: The position of the electrode in relation to the axon and the distance from the electrode r where the extracellular potential V_e is observed. Figure and description from Rattay (1990).

Since the axon extends along the x axis, the activity of the axon can be calculated at the points $x_n = n \cdot \Delta x$. Therefore, in the segmented fiber, the influence of the

extracellular potential on the stimulation can be calculated through the second difference quotient of the extracellular potential along the axon, which reads:

$$\frac{V_{e,n-1} - 2V_{e,n} + V_{e,n+1}}{\Delta x^2} \tag{2.7}$$

The so-called activating function f, which represents the second derivative of the extracellular potential along the fiber, can be used to determine the influence of the extracellular electrode on unmyelinated fibers. Activating function is calculated according to the following equation:

$$f = \frac{\partial^2 V_e}{\partial x^2} \tag{2.8}$$

where V_e and f are functions of x and t.

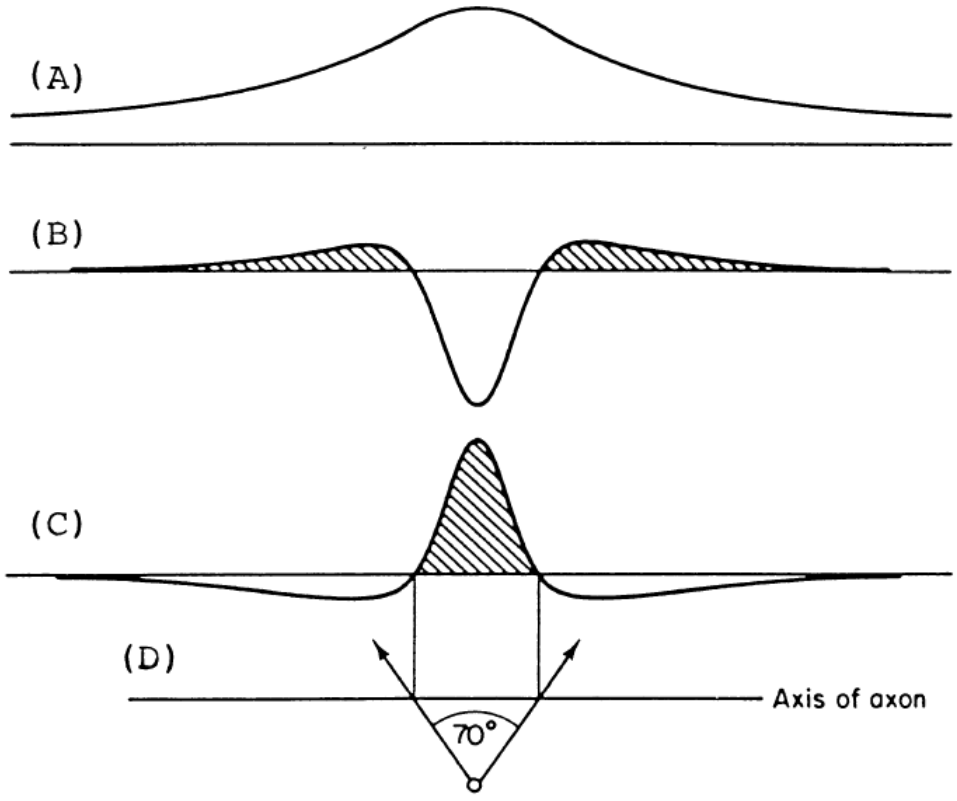

Figure 10: The influence of the microelectrode on the stimulation along the fiber. The horizontal axis represents the x-axis. The electrode is positioned at $x = 0$. (a) Change in extracellular potential during a positive (anodic) stimulus. (b) Activating function for anodic stimulation. (c) Activating function for negative (cathodic) stimulation. (d) Position of the electrode relative to the fiber to obtain the upper sub-figures. An angle of about 70° represents the boundary between the parts of the fiber that are depolarized and

hyperpolarized. Changes in the conductance of the extracellular medium and changes in fiber parameters do not affect this angle, as long as the extracellular medium is homogeneous and isotropic. Figure and description from Rattay (1990), Rattay (1987).

Figure 10 shows the change of extracellular potential during anodic stimulus (a), activating function for anodic *(b)* and cathodic *(c)* stimulation. It can be seen from Figure 10c that the maximum of the activating function during the cathodic stimulus is at the point closest to the electrode, where $x = 0$, which was also proven experimentally. From Figure 10d, it can be seen that the angle of about 70° represents the border between the activated and deactivated part of the fiber. In other words, the length of the stimulated part of the fiber during the cathodic stimulus is $x = \sqrt{2} \cdot z$. From this it can be concluded that the parts of the fiber where the activating function is positive are stimulated, and the voltage of the fiber becomes negative in the parts where the activating function is negative.

Equivalent to intracellular stimulation, if the cathodal stimulus of extracellular stimulation is too weak, too short or the electrode is too far away (subthreshold stimulation), the membrane passively responds to the stimulus and no action potential occurs.

It was mentioned earlier that by extracellular stimulation with sufficiently strong anodic currents, it is possible to cause an action potential. This can be seen from Figure 10b, where next to the strongly expressed hyperpolarized part of the fiber closest to the electrode, where $x = 0$, there are two less pronounced depolarized parts that are a consequence of the flow of capacitive currents. If the voltage in those two parts reaches the threshold voltage, an action potential is generated.

Contrary to the phenomenon mentioned above that it is possible to cause an action potential with a strong extracellular anodic stimulus, there is a phenomenon where a too strong extracellular cathodic stimulus stops the action potential. This can be explained by either blocking the propagation of the action potential which is caused by *anodal surround* effect (Ranck, 1975), also referred to as *blocking phenomenon* (Rattay, 1990), or by stopping the generation of the action potential, which is known as *upper stimulation threshold* (Boinagrov, et al., 2012; Rattay, 2014; Meng, et al., 2018; Fellner, et al., 2019; Sajedi, et al., 2021).

- The explanation of the anodal surround block (blocking phenomenon) given by Ranck (1975) and Rattay (1990) is that with a very strong stimulus in the area closest to the electrode (in Figure 10c where $x = 0$) strong depolarization and opening of sodium channels occurs, but also in the adjacent areas there is a strong hyperpolarization that prevents the propagation of the action potential.

From Figure 10c, this can also be concluded when a stronger stimulus is imagined that emphasizes the hyperpolarized parts even more.

- The explanation of the upper stimulation threshold given by Boinagrov, et al. (2012) is that sodium channels open with a very strong stimulus, but because the electrical force that drives sodium ions outside the cell becomes stronger than the chemical gradient that drives them inside the cell, a sodium current reversal occurs where instead of an influx of sodium ions efflux occurs. This leads to the generation of an action potential not occurring at all.

3 Spiking Efficiency

According to White, et al. (2000), neurons seem to have noisy dynamics. This is caused by the so-called *channel noise*, which arises as a result of the random gating of ion channels. The relationship between channel noise and spiking efficiency has been statistically presented (Lecar & Nossal, 1971).

When stimulating a nerve cell, there is a range of stimulus intensity in which the probability of the occurrence of an action potential increases from 0 (0 %) to 1 (100 %) (Rattay & Tanzer, 2022b). This probability is called spiking efficiency (also referred to as spiking/spike probability, firing probability or firing efficiency) and is defined as the ratio of the number of spikes (action potentials) caused by a train of stimulation pulses to the number of stimulation pulses (Rattay & Tanzer, 2022a). Therefore, for example, a spiking efficiency of 1 (100 %) means that every stimulus of a certain strength causes an action potential, and 0 (0 %) means that an action potential never occurs.

Figure 11 from the experiments (Verveen & Derksen, 1968) show the response of the node of Ranvier membrane stimulated by a train of identical stimuli of strength that leads to a spiking efficiency of about 0.5. Thereby, eight stimuli of 5 ms duration were sent with an interval of 2 s between the pulses. Several interesting observations can be seen from the figure. Eight stimulation pulses elicited five action potentials. The reason for this is the difference in the amplitude and duration of depolarization from trial to trial. There is also a difference in the delay of the generated action potentials.

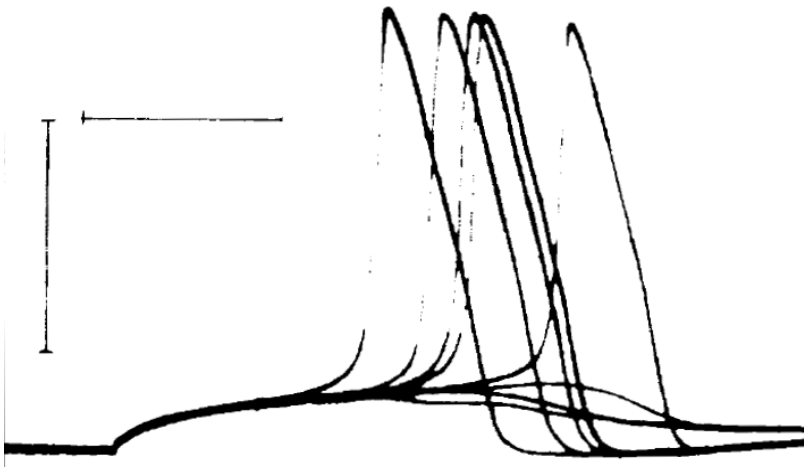

Figure 11: The response of the membrane of the node of Ranvier to a train of eight stimulation pulses. The duration of stimulation is 5 ms, the distance between pulses is 2 ms. A superposition of eight consecutive membrane responses is presented. Figure and description modified from Verveen & Derksen (1968).

In the Verveen's experiments (Verveen, 1960) on the peripheral nerve fiber of the green frog, the relationship between stimulus strength and spiking efficiency was determined. The initial current stimulus was such that the spiking efficiency was 0 (0 %) and was increased in intervals of approximately 0.5 % of the threshold intensity until the spiking efficiency reached the value of 1 (100 %). Threshold is defined as the strength of the stimulus at which the spiking efficiency is 0.5 (50 %). Through statistical tests, Verveen first confirmed that the fluctuations of positive and negative reactions to the stimulus are random and symmetrically distributed around zero and that they do not conflict with the theory that consecutive reactions of neurons are independent. He showed that the relationship between stimulus strength and firing efficiency could be represented by a sigmoid curve (cumulative distribution function of the normal (Gaussian) distribution). In the end, Verveen demonstrated that two parameters could be sufficient to describe the relationship between stimulus strength and spiking efficiency. The first is the previously mentioned threshold. The second is called the spread, which represents the width of the curve (the standard deviation of the distribution function) and has the same units as the stimulus strength. In addition to these two parameters, the so-called relative spread (RS) is presented. The relative spread is defined by Verveen as the ratio of the spread and the threshold, so by definition it is independent of the strength of the stimulus, and it was also observed that the RS is independent of the duration of the stimulus. For a better visualization, see Figure 12.

Figure 12 represents the relationship between spiking efficiency and stimulus intensity (Rattay & Tanzer, 2022b). Their relationship indeed seems to follow the sigmoid relationship mentioned above, which can be seen in the thick black line created by Gaussian fitting of five points of spiking efficiency at intensities of 600, 650, 700, 750 and 800 μA. To obtain each of the five points, a train of 100 stimulation pulses of corresponding stimulus intensity was sent. All the above-mentioned parameters (threshold, spread and relative spread) can be seen in the figure. Threshold is marked with a red line and is found at a stimulus intensity of 700 μA. The relative spread, written as RS, is represented as a percentage and its value is 7 %. With σ, the spread is represented by magenta letters and is 50 μA. The parameter that has not been mentioned so far, and is found in Figure 12, is the dynamic range. Dynamic range (DR) is defined as the range of stimulus intensity in which spiking efficiency increases from 0.1 (10%) to 0.9 (90%) (Shepherd & Javel, 1997). In Figure 12 dynamic range is written in cyan and its value is 128 μA.

One of the important parameters used in this thesis is the dynamic range normalized to threshold and it is calculated, as the name suggests, by dividing the dynamic range

by the threshold. From the evaluation of the cumulative Gaussian curves similar to that in Figure 12, it was concluded and mathematically explained that the dynamic range (DR) normalized to threshold is equal to 2.56 times the relative spread (RS) (Rattay & Tanzer, 2022b).

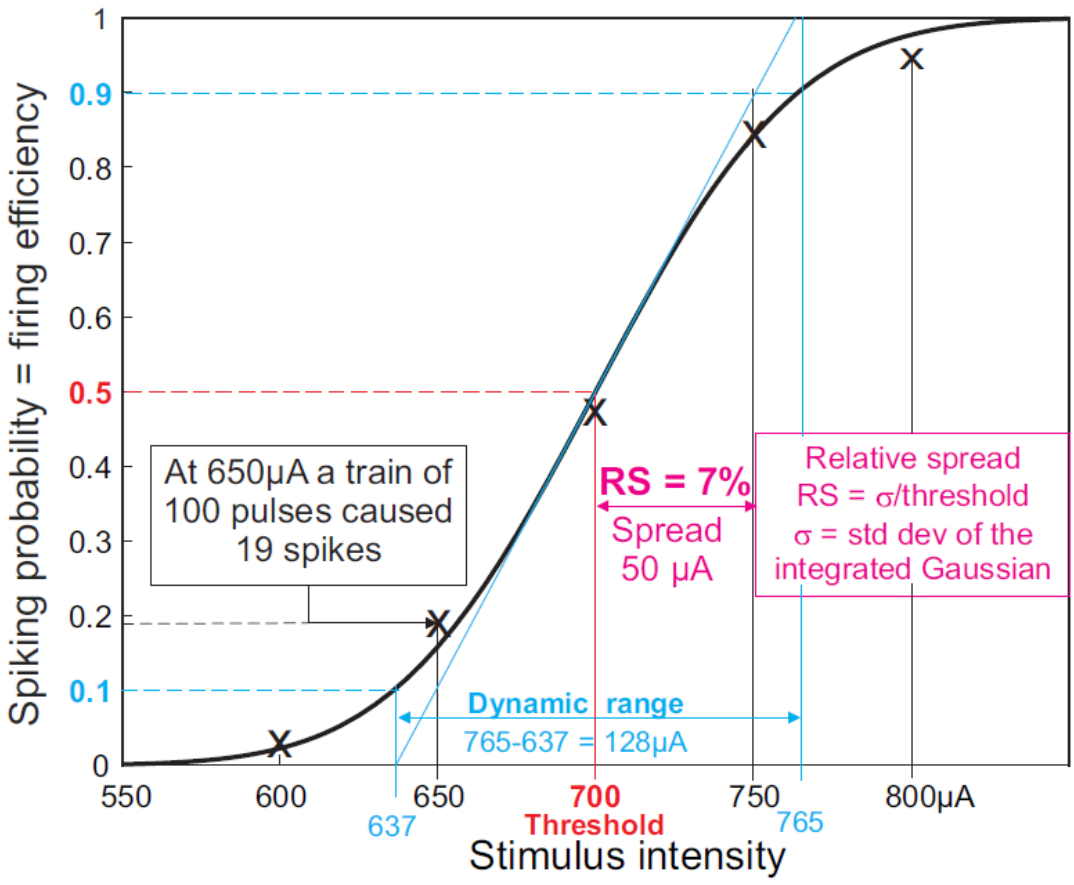

Figure 12: Relationship of spiking efficiency, spread, relative spread and dynamic range to stimulus intensity. From five spiking efficiencies (represented by black x) at intensities of 600, 650, 700, 750 and 800 μA, a black curve was obtained by Gaussian fit. At a threshold of 700 μA, marked in red, the spiking probability is 0. 5. Figure and description from Rattay & Tanzer (2022b).

As stated in the introduction of this section, noisy dynamics of neurons, which is due to the random gating of ion channels embedded in the cell membrane (channel noise), seems to be responsible for the spiking efficiency, and therefore the dynamic range (Lecar & Nossal, 1971).

Since the Hodgkin-Huxley model is deterministic and therefore does not include noisy dynamics, it is necessary to include a noise component in it to obtain a stochastic model. One of the ways to accomplish this is described in Rattay (2000) where the hypothesis from Rubinstein (1995) was used which suggests that the number of sodium channels affects the noise in such a way that the amplitude of the noise is proportional to the root of the number of sodium channels.

Noise current, which is added to every compartment, is defined as (Rattay, 2000):

$$I_{noise} = GAUSS \cdot k_{noise}\sqrt{A_n \cdot g_{Na}} \qquad (3.1)$$

where $GAUSS$ represents variable following a normal (Gaussian) distribution with a mean $\mu = 0$ and standard deviation of $\sigma = 1$ and its value changes every $2.5\ \mu s$. Common to all compartments is standard factor k_{noise} which is given in $\mu A\ mS^{-1/2}$. A_n represents the area of the membrane in cm^2 and g_{Na} the maximum sodium conductance per square unit in $mS\ cm^{-2}$.

In the initial formula for I_{noise} transmission time $Dt = 2.5\ \mu s = 0.0025\ ms$ was used (Rattay, 2000). In order for I_{noise} to be used at other transmission times, the following rule of thumb is suggested for obtaining the k_{noise} parameter at Dt different from $0.0025\ ms$ (Rattay & Tanzer, 2022b):

$$k_{noise}(Dt) = \sqrt{\frac{0.0025}{Dt}} \cdot k_{noise}(Dt) \qquad (3.2)$$

A relationship between relative spread (RS) and axon diameter is presented by Verveen (1962). From his experiments on crag-fish, cuttle-fish and frog axons, Verveen obtained an equation that represents the ratio of the logarithm of RS and the logarithm of the diameter:

$$\log(RS) = -1.50 - 0.80 \cdot \log(d) \qquad (3.3)$$

where diameter d is given in μm.

Similar results as in experimental results from Verveen (1962) were obtained in simulation experiments with three different models (Rattay & Tanzer, 2022b). It was tested which values of the k_{noise} parameter at $Dt = 0.0025\ ms$ give the results closest to Verveen's experiments. Unlike Verveen, in these simulation experiments a distinction was made between myelinated and non-myelinated axons. Two models were used for myelinated axons, HH10 and CRRSS, with diameters of $1\ \mu m$ and $10\ \mu m$. HH10 means tenfold values of the HH model in the nodes of Ranvier ($g_{Na} = 1200$, $gk = 360$, $gl = 3$ with units mS/cm^2). This model describes well the current fluctuations in the active membrane of auditory nerves (Rattay, et al., 2001). The CRRSS model, named after the authors Chui, Richie, Rogert, Stagg and Sweeney, is based on myelinated rabbit nerve data and demonstrated that the potassium ion current can be neglected in the nodes of Ranvier. Thus, it is even simpler than the HH model

and it is often preferred for biomedical simulations at 37°C (Rattay, et al., 2003). For the non-myelinated axon, the HH1 model was used, and in this case diameters of 1 μm, 10 μm and 10 μm were used. In order to be able to adjust the k_{noise} parameter to the experimental data, the current I_{noise} was added to all active compartments (in nodes but not in internodes). The following log-log relations were obtained for fitting k_{noise} values to Verveen's formula (3.3):

$$\text{HH10, } k_{noise} = 0.00042 : \log(RS) = -1.51 - 0.76 \cdot \log(d) \qquad (3.4)$$

$$\text{CRRSS, } k_{noise} = 0.0038 : \log(RS) = -1.54 - 0.80 \cdot \log(d) \qquad (3.5)$$

$$\text{HH1, } k_{noise} = 0.0038 : \log(RS) = -1.51 - 0.76 \cdot \log(d) \qquad (3.6)$$

Figure 13 presents a comparison of three simulation experiments at selected k_{noise} parameters with Verveen's formula.

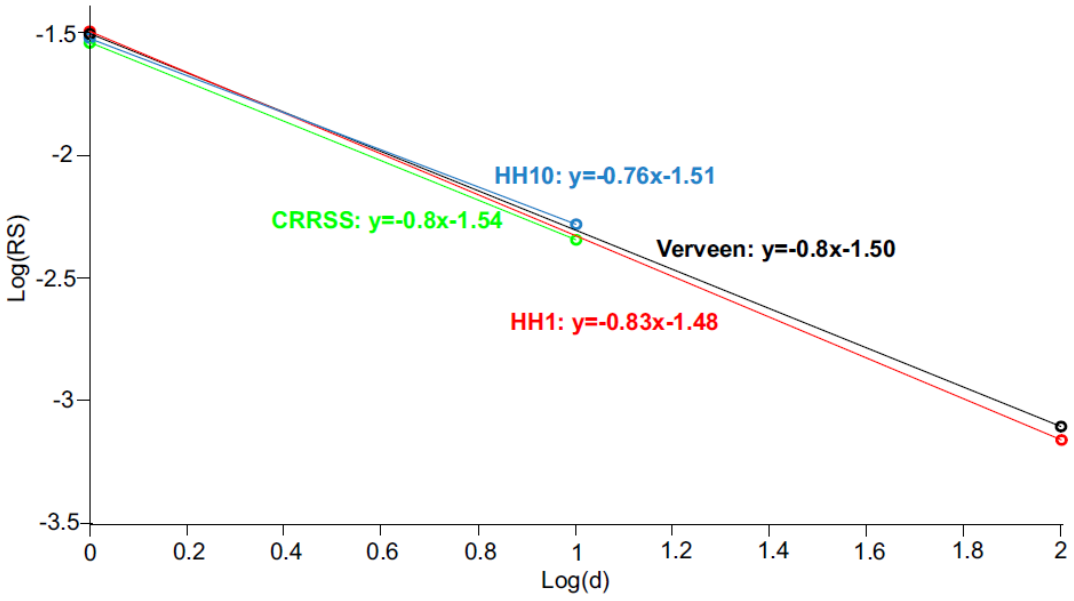

Figure 13: Comparison of three simulation experiments at selected k_{noise} parameters with Verveen's formula, which is represented in black. The CRRSS (myelinated axon, $k_{noise} = 0.0038$) model is represented in green and has the same straight line slopes as Verveen and a small vertical offset. Both the HH10 (myelinated axon, $k_{noise} = 0.00042$) model represented in blue, and the HH1 (non-myelinated axon, $k_{noise} = 0.0038$) model represented in red show little difference in straight line slopes as well as vertical displacement compared to Verveen's formula. Internodes in myelinated models are idealized where $G_m = 0$ and $C_m = 0$. Figure and description from Rattay & Tanzer (2022b).

Figure 14 shows the relationship between spiking efficiency and stimulus intensity normalized to threshold obtained from experiments performed on the HH10 model of myelinated axon, where the diameter of the axon is $d = 1\ \mu m$ and the electrode distance is 500 μm (Rattay & Tanzer, 2022b). The hypothesis that there is a linear relationship between the common factor k_{noise} and RS was tested. The initial k_{noise} used was 0.00025 and was doubled twice. For each k_{noise} value, 100 points obtained from 500 simulations for each stimulus intensity were calculated, and fitted by a cumulative Gaussian function. Current intensities from 0.6 threshold intensity in steps of 0.01 up to 1.6 threshold intensity were used to calculate those 100 points. Noisy current I_{noise} was added to all active compartments.

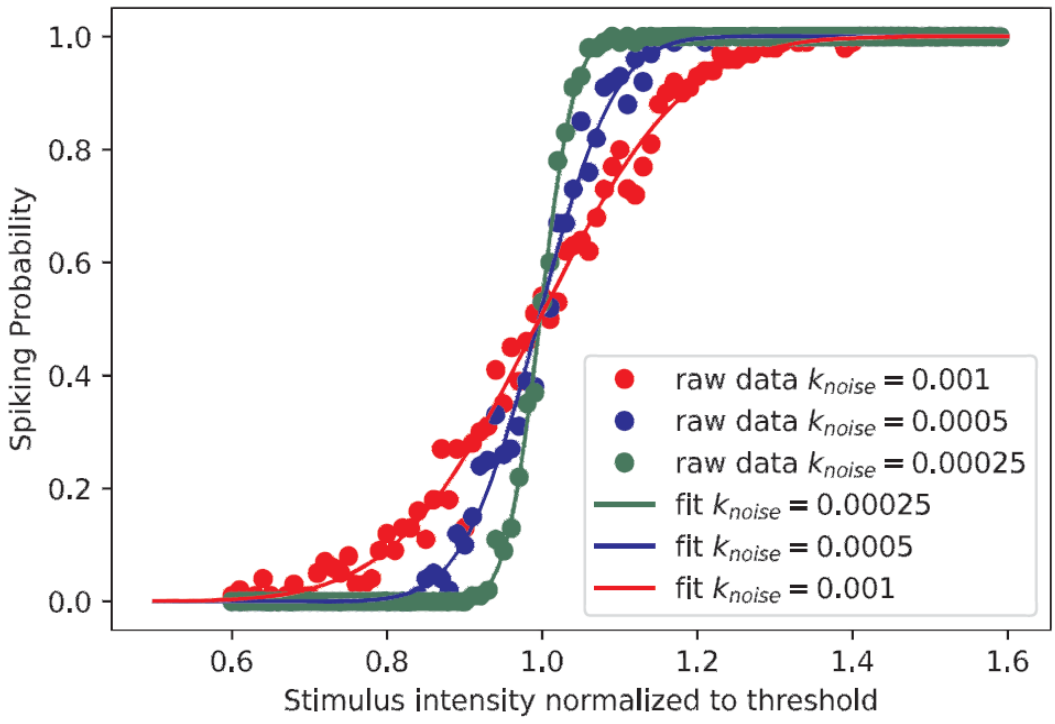

Figure 14: The relationship between spiking efficiency and stimulus intensity normalized to threshold. An increase in k_{noise} leads to a linear increase in RS. Calculations were performed on 100 intensities around the threshold, from an intensity of 0.6 threshold in steps of 0.01 to 1.6 threshold. Spiking efficiency was determined from 500 runs for each point. Cumulative Gaussian fitting of those 100 points was then performed. The simulation experiments were performed on the HH10 model of myelinated axon, where the diameter of the axon is $d = 1\ \mu m$ and the electrode distance is 500 μm. Figure and description from Rattay & Tanzer (2022b).

As well as at lower threshold, DR can also be examined at upper threshold. In contrast to stimulation at lower threshold, with stimulation at upper threshold, spiking efficiency decreases if the strength of the stimulus increases and increases if the strength of the stimulus decreases. The reason for this is the blocking phenomenon, during which the AP propagation/initiation stops when the cathodic stimulus is too

strong (see section 2.2.2). The Cumulative Gaussian curve that describes the change in spiking efficiency in relation to the stimulus intensity would in this case look as if the cumulative Gaussian curve from Figure 12 was reflected over an imaginary line parallel to the y-axis that passes through the threshold (Meng, et al., 2018).

3.1 The Importance of Spiking Efficiency Examination

Models with a stochastic component (noise) are not only more realistic, but also enable research related to spiking efficiency which can be used, for example, to improve the quality of functional electrical nerve stimulation.

When auditory nerve fibers are electrically stimulated with cochlear implant electrodes, the key control element of the input-output relation is the spiking efficiency as a function of the stimulus intensity, whereby an improvement in the quality of sound perception is expected with a higher DR (Rattay & Tanzer, 2022a). Therefore, it is important to investigate which part of the cell has a greater DR. Recent studies suggest that spiking efficiency could be used to improve selective cell stimulation (Tandon, et al., 2021) or that noise could potentially be used to predict the cell's response to electrical stimulation (Madugula, et al., 2022). Although these two studies were performed on retinal ganglion cells (RGCs), it was stated that these approaches may be used also for other neuronal populations such as those stimulated by cortical implants. In recent studies related to cortical (mostly pyramidal) cells and spiking efficiency it has been investigated how cortical stimulation affects the spiking efficiency of neurons in a volume of tissue (Komarov, et al., 2019) or spiking efficiency was presented as part of the investigation of other phenomena as in Radivojevic, et al. (2016).

In the mentioned studies, it can be seen how spiking efficiency is used in different ways and for different purposes. Bearing in mind that this is probably a small number of applications and the potential of spiking efficiency, it can be concluded that more detailed research could be important for further improvements of nerve stimulation.

4 Neuron Software

NEURON is a simulation environment developed for creating realistic models of neurons both in terms of chemical and electrical signaling, where it is possible to simulate both individual neurons and a network of neurons (Hines & Carnevale, 1997). The advantage of NEURON is that it is possible to construct and test numerically stable and computationally efficient models, which does not require extensive knowledge of programming or numerical methods, thus the study of everything from the molecular biology of voltage-gated channels to how a network of thousands of neurons interact with one another is covered (Carnevale & Hines, 2006). The number of NEURON users in the field of neuroscience is increasing daily, along with the number of scientific publications in which NEURON was used[2]. According to data from the official NEURON website[3], more than 2600 research reports have used NEURON at the time of writing this thesis. Thousands of computational neuroscience models along with their publications can be found in NEURON's ModelDB[4]. NEURON is used in many of them as a simulation environment. The reason for that are probably NEURON's many advantages over general purpose simulation programs, since it is exclusively designed for simulating equations related to nerve cells, as described by Hines & Carnevale (1997):

- The NEURON is particularly suitable for models where membrane characteristics are not spatially homogeneous and membrane currents are not constant and are complex.
- Functions in NEURON are developed to control simulations and make graphs of the results of real problems related to neuroscience.
- NEURON's computing engine uses methods and tricks that take into account the structure of neural equations, which makes it very efficient.
- The ability to deal directly with neuroscience-related subjects rather than first translating the problems into another area is one of NEURON's key strengths.

[2] https://www.neuron.yale.edu/neuron/what_is_neuron
[3] https://neuron.yale.edu/neuron/publications/neuron-bibliography
[4] ModelDB is a database where neuroscience models and their detailed description, along with citations of scientific publications where the models are used can be stored and efficiently retrieved. https://senselab.med.yale.edu/ModelDB/default

NEURON is very suitable for branched structures and for problems where it is important to calculate ionic concentrations and extracellular potential near the cell membrane. Additionally, NEURON's model description language NMODL is suitable for developing and inserting new membrane mechanisms and dynamics, such as for example various voltage-gated ion channels into the model (Hines & Carnevale, 1997). Since 2009, in addition to the Hoc interpreter, NEURON also enables the full use of Python as an alternative interpreter alone, or in combination with the Hoc, which brings a lot of benefits such as expressive and more intuitive syntax and modularity support (Hines, et al., 2009).

4.1 Spatial and Temporal Discretization

Unless otherwise noted, the section about Spatial and Temporal Discretization is described according to *The NEURON Book* (Carnevale & Hines, 2006), written by two of the three primary developers of NEURON.

In order to simulate the activity of real neurons, NEURON employs the crucial strategy of time- and space-discretization. Compartmentalization, which describes the representation of the cable equation separated into a number of compartments linked by a resistor, is a common synonym for discretization. The better approach to understand discretization, though, is not in this way. A better definition of discretization would be: a system that is discontinuous in time and space is used to approximate the initial continuous system.

The simulation of a discretized model is accomplished by calculating the values of spatiotemporally continuous variables over a collection of discrete points in space for a limited number of instants in time.

The accuracy, sometimes the stability of the solution, but also how faithfully the behavior of the continuous system is imitated by the computed solution is affected by the size of the time step Δt and how fine the spatial discretization Δx is between neighboring nodes. The necessary accuracy and computing effort needed for a discrete approximation of a continuous system rely on a variety of factors, such as the system's anatomy or biophysics, but in essence everything is specific depending on the problems and tasks under consideration. In order to better approximate the curvature

in space and time of the continuous variables of the original physical system, the discontinuous variables Δt and Δx in the discretized model must be small enough. However, with the decrease in the value of discontinuous variables Δt and Δx computation costs increase. Therefore, it is not always easy to choose the appropriate discretization:

- The discretization can be very "rough" and simple. An example of this would be to find the resting membrane potential of an isopotential model with a passive membrane. In such a case, it would be sufficient to choose several time steps in just one point in space.
- The discretization can be very "fine". In some cases, high spatiotemporal resolution is required, and therefore it can be quite difficult to choose Δt and Δx appropriately. An example of this would be models with an active membrane, which can be very complex and branched, where the time course of the membrane potential is determined as it fires action potentials.

Spatial discretization and integration time step are related to each other and care should be taken during their selection.

4.1.1 Spatial Discretization

Sections are used to model cell morphology. They can vary in shape, their properties can vary in relation to position along their length, and they can be connected to each other and form branched structures. Each section is subdivided into segments that are internally connected by resistors, which model the intracellular resistivity. Each segment has its own geometry and underlying cable model. Therefore, the geometry of the section is determined by the geometry of the connected segments. Sections can be connected to each other, whereby connections can be realized with any segment of the parent section. Each parent section can have multiple child sections, as represented in Figure 15.

By default, sections and segments are cylindrical. It is also possible to create complex structures using 3D point data that determine the exact coordinates of the segments. In this way, truncated cones are obtained which, with sufficient spatial discretization, can represent various irregular surface areas.

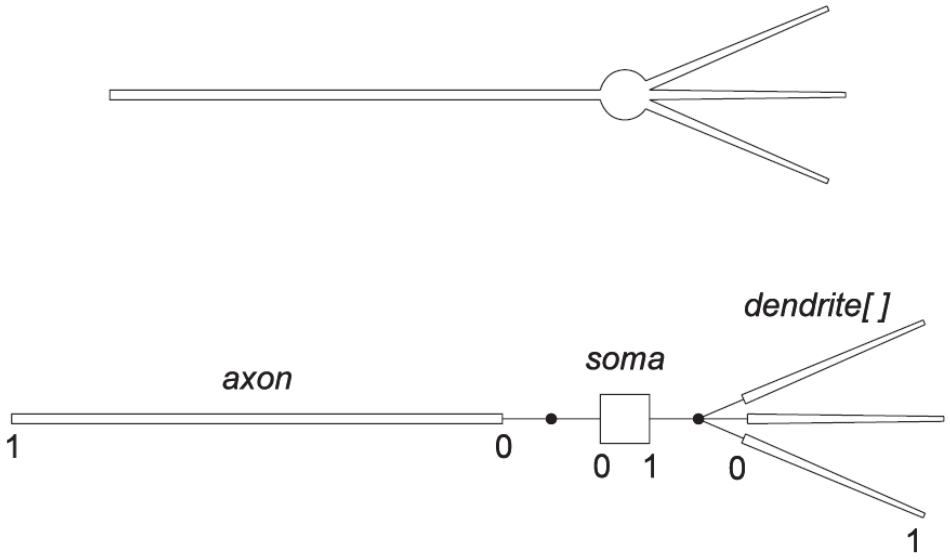

Figure 15: Top: cartoon of a neuron with a soma, three dendrites, and an unmyelinated axon. Bottom: topology of a NEURON model that represents this cell. The morphology of this cell is represented by five sections. An axon is connected to the beginning of the soma, and three dendrites are connected to the end. Figure and description from Hines & Carnevale (1997).

The distance along the section is normalized by the positional parameter x, where $x = 0$ represents the beginning and $x = 1$ the end of the section. The section contains an $nseg$ parameter that represents the number of segments. Adjacent segments of one segment are equidistant, namely $1/nseg$ and the location of the centers of the nodes of the segments are at $x = (2i - 1)/(2nseg)$, where i is an integer in the range $[1, nseg]$ (Hines & Carnevale, 1997).

Figure 16 represents a section with two segments of equal length that span the length $[0, 0.5]$ and $[0.5, 1]$ of the section (Hines & Carnevale, 1997). The centers of the segments are located at $x = 0.25$ and $x = 0.75$ respectively, and those points are assigned membrane characteristics for the above-mentioned spans of x.

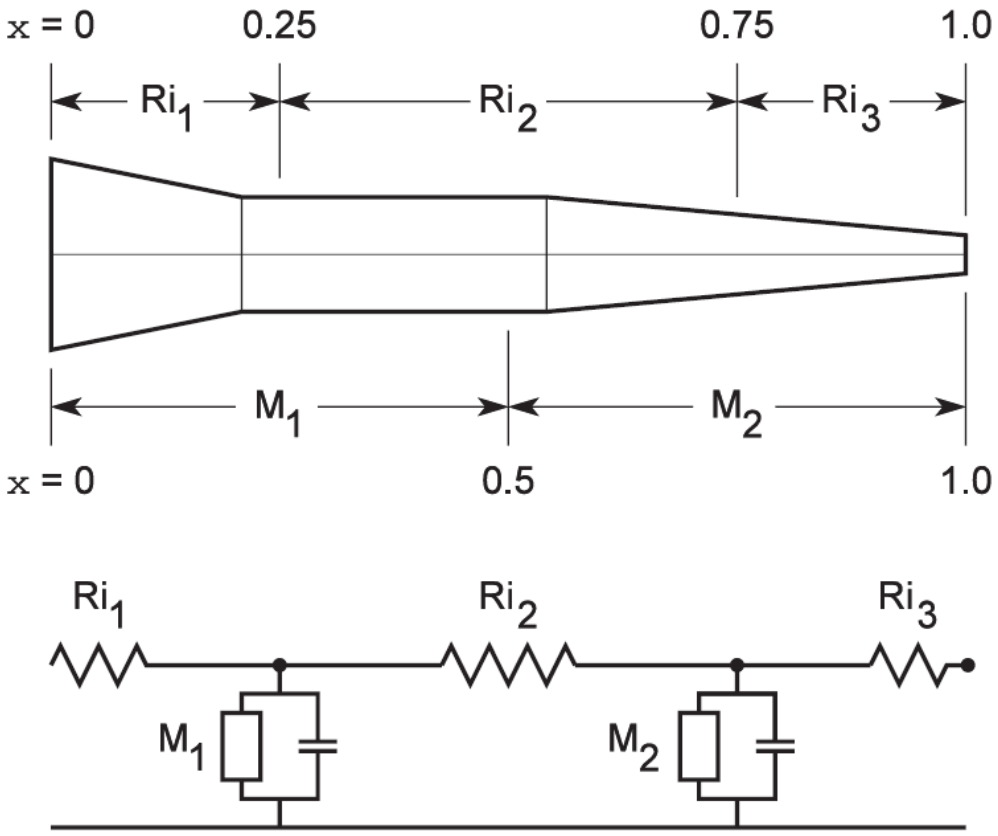

Figure 16: Neurite represented by a section with two segments of equal lengths M_1 and M_2. Membrane characteristics are assigned to nodes at the midpoints of M_1 and M_2. Axial resistances Ri_1, Ri_2 and Ri_3 are determined by integrating the cytoplasmic path resistance over the x intervals $[0, 0.25]$, $[0, 25, 0.75]$ and $[0.75, 1]$. Figure and description from Hines & Carnevale (1997).

4.1.2 Temporal Discretization

In NEURON it is possible to choose one of two stable implicit integration methods (Hines & Carnevale, 1997):

- Backward Euler: It is the default integrator in NEURON. Since it is very stable integration method, it can be used with large time steps Δt. Its numerical error is proportional to Δt.
- Crank-Nicholson: This integration method is more accurate for small time steps Δt. Its numerical error is proportional to Δt^2. It could have stability problems for example for large time steps Δt and for small intracellular resistances.

5 Methodology

In order to examine the spiking efficiency, and thus dynamic range (DR), on a pyramidal cell, a simplified version of a pyramidal cell with all its important parts was modeled. The ultimate goal is to determine how individual neuron characteristics affect DR. These characteristics can be of a geometric nature, such as the shape of the cell and the position of the stimulating electrode, but also of an electrical nature, such as the electrical characteristics of the cell itself, such as sodium ion conductivity, or the type of stimulation current, such as monophasic or biphasic etc.

All the models presented in this thesis are multicompartment cable models made in NEURON (version 8.2.0). NEURON is accessed through Python (version 3.8.3) for easier and more refined model control. Also, all measurements were made with the help of Python, as well as all plots. The geometries and topologies are based on those from Rattay & Tanzer (2022b) and Rattay & Wenger (2010). Stimulations were performed extracellularly with a monopolar micro electrode, monophasically and biphasically, but also intracellularly. The mechanisms and dynamics are done according to the principle of Hu, et al. (2009) and Rattay & Wenger (2010), and are in the style of Hodgkin and Huxley. All details will be presented in the following sections.

All three models in this thesis are one-dimensional (1D). This means that the models are elongated only in one axis, where the axis passes through the center of the model and forms the axis of symmetry. Geometrically, different parts of the cell are represented by different lengths and diameters of cylinders. Therefore, although NEURON is capable of dealing with three-dimensional (3D) coordinates, in this case two-dimensional (2D) coordinates are sufficient. Thus, the y coordinate was eliminated, and the position of the electrode was changed in the x and z coordinates.

The *1D model* of the pyramidal cell allows for parallel computation, so all calculations were performed on a 60-core server at the Vienna University of Technology. This step was necessary due to the complexity and the large number and duration of simulations, which would last incomparably longer on private computers and laptops. All desired stimulation coordinates, amplitudes and other parameters were first of all written in one text file from where the program read them and based on them started simulations. All calculated values were written in another text file next to all initial parameters for easy reference and interpretation. In the end, everything was done in such a way that

it was only necessary to start the server once and, in the end, just take the file with the calculated values.

In order to examine spiking efficiency, it was also necessary to model the noise in the cell. This was done in a similar way as in Rattay & Tanzer (2022a) and Rattay & Tanzer (2022b) where a random Gaussian current with a mean value of 0 and a standard deviation of 1 was injected into the individual segments of the cell. A detailed explanation of spiking efficiency and noise modeling can be found in sections 3 and 5.3.

5.1 Mechanisms and Channel Types

All mechanisms used in this thesis are taken from ModelDB[5] and are used in the model presented in the paper from Hu, et al. (2009). Values are adjusted according to the paper from Rattay & Wenger (2010) and above-mentioned paper from Hu, et al. (2009).

Not counting passive mechanisms, all active mechanisms and channels in this chapter are described in a similar way as in Burian (2017).

As already mentioned earlier, in addition to the phospholipid bilayer, the electrical characteristics of the membrane are also affected by ion transport through the membrane. There are two types of ion transport across the membrane. These are passive diffusion and active transport through ion channels.

5.1.1 Passive Mechanism

In addition to NEURON's general passive parameters such as specific membrane capacitance[6] *cm* (C_m) and specific axial resistance[7] *Ra* (ρ_a), additional passive parameters are required. These are the specific leakage conductance *g_pas* (g_{pas}) and the leakage reversal potential *e_pas* (E_{pas}) related to it. To make additional parameters available, it is necessary to insert new channels into the cell membrane. NEURON already contains a mechanism with these channels, so for this need it is not necessary to insert a new mechanism in the form of a *.mod* file manually. It is only necessary to import the special "pas"[6] channel mechanism. It enables the simulation of membrane resistance and reversal potential. The units for specific membrane conductance and

[5] https://senselab.med.yale.edu/ModelDB/ShowModel?model=123897&file=/HuEtAl2009/
[6] https://www.neuron.yale.edu/neuron/static/docs/help/neuron/neuron/mech.html
[7] https://www.neuron.yale.edu/neuron/static/docs/help/neuron/neuron/geometry.html

reversal leakage potential are given in S/cm^2 and mV respectively. Often, instead of specific membrane conductance, its inverse value, specific membrane resistance is given, whose units are $\Omega \cdot cm^2$.

In addition to the passive mechanism, seven more mechanisms were used in this thesis, two of which are sodium, three potassium and two calcium mechanisms. Six of them represent ion channels, and one calcium mechanism Ca_{cm} is responsible for passive calcium influx and active calcium efflux.

5.1.2 Sodium Channels

As mentioned earlier, voltage gated sodium channels are the most responsible for the first phase of the action potential. All sodium channels in this thesis are voltage gated. Since it was shown that sodium channel subtypes have different thresholds, different biophysical characteristics and are distributed differently in the cell (Rush, et al., 2005), two types of sodium channels were used in this thesis. Those are $Na_v1.2$ and $Na_v1.6$ channels. The index v indicates that it is a voltage-sensitive ion channel.

Both sodium channels have Hodgkin-Huxley style kinetics described by Mainen, et al. (1995). As stated there, kinetics were fit to data from Huguenard, et al. (1988) and Hamill, et al. (1991). The currents through the membrane related to sodium channels are calculated as follows (Mainen, et al., 1995):

$$i_{Na} = t_{adjust}\, g_{Na}\, m^3\, h\, (V - E_{Na}) \qquad (5.1)$$

where i_{Na} represents current density related to sodium channels and is given in mA/cm^2. The maximum conductance is represented by g_{Na}, and its unit is $pS/\mu m^2$ (HH and NEURON dimensions are given in mS/cm^2, $1\ mS/cm^2 = 10\ pS/\mu m^2$). The variables m and h represent the probabilities for open activation gates and the probability for open inactivation gates, respectively. t_{adjust} is the temperature coefficient described in section 5.1.5.

The activation is described by the steady-state variable m_∞ and the time constant τ_m, which depend on the opening and closing rates α and β, as in the following equations (Mainen, et al., 1995):

$$m_\infty = \alpha/(\alpha + \beta) \qquad (5.2)$$

$$\tau_m = 1/(\alpha + \beta) \qquad (5.3)$$

while α and β depend on the local transmembrane potential V_m and are obtained in the following way:

$$\alpha(V_m) = \frac{A \cdot (V_m - V_{1/2})}{1 - e^{-(V_m - V_{1/2})/k}} \tag{5.4}$$

$$\beta(V_m) = \frac{-A \cdot (V_m - V_{1/2})}{1 - e^{(V_m - V_{1/2})/k}} \tag{5.5}$$

where A is the rate constant, k is the slope of the activation curve, and $V_{1/2}$ is the half activation voltage.

The inactivation for the time constant τ_h is described in an analogous way as the time constant τ_m, while the steady state value h_∞ is described in the following way (Mainen, et al., 1995):

$$h_\infty = \frac{1}{1 + e^{(V_m - V_{1/2})/k}} \tag{5.6}$$

The largest number of sodium channels in the *1D model* in this thesis is located in the axon initial segment (AIS) and in the nodes of Ranvier.

Reversal potential of $E_{Na} = 60\ mV$ (Rattay & Wenger, 2010; Hu, et al., 2009) is of such value for both types of sodium channels. From the work of Hu, et al. (2009) published in the NEURON ModelDB the values for the coefficients A, the slopes k and the half (in)activation voltages $V_{1/2}$ were obtained after subtracting the corresponding value for the shift dependence of the kinetics from the voltage as in Rattay & Wenger (2010).

5.1.2.1 $Na_v1.2$ Channel

This type of voltage-gated sodium channels is responsible for the promotion of action potential propagation to the soma (Hu, et al., 2009). These are high-threshold sodium channels. In the *1D model* in this thesis, these channels are located in the dendrite, soma, axon hillock and in the AIS.

The following table shows the values for the coefficients A, the slopes k and the half (in)activation voltages $V_{1/2}$.

$A(\alpha_m)$	0.182	$k(\tau_m)$	7	$V_{1/2}(m)$	-28 mV
$A(\beta_m)$	0.124	$k(m_\infty)$	7	$V_{1/2}(h_\infty)$	-57 mV
$A(\alpha_h)$	0.024	$k(\tau_h)$	5	$V_{1/2}(\alpha_h)$	-35 mV
$A(\beta_h)$	0.0091	$k(h_\infty)$	6.2	$V_{1/2}(\beta_h)$	-60 mV

Table 1: Values for the coefficients A, the slopes k and the half (in)activation voltages $V_{1/2}$ for $Na_v1.2$ channels. Values from Rattay & Wenger (2010).

5.1.2.2 $Na_v1.6$ Channel

This type of voltage-gated sodium channel is responsible for controlling the initiation of the action potential (Hu, et al., 2009). These are low-threshold sodium channels. In the *1D model* in this thesis, these channels are located in the dendrite, soma, AIS, unmyelinated axon and in the nodes of Ranvier.

The following table shows the values for the coefficient A, the slopes k and the half (in)activation voltages $V_{1/2}$.

$A(\alpha_m)$	0.182	$k(\tau_m)$	6	$V_{1/2}(m)$	-41 mV
$A(\beta_m)$	0.124	$k(m_\infty)$	6	$V_{1/2}(h_\infty)$	-70 mV
$A(\alpha_h)$	0.024	$k(\tau_h)$	5	$V_{1/2}(\alpha_h)$	-41 mV
$A(\beta_h)$	0.0091	$k(h_\infty)$	6.2	$V_{1/2}(\beta_h)$	-73 mV

Table 2: Values for the coefficients A, the slopes k and the half (in)activation voltages $V_{1/2}$ for $Na_v1.6$ channels. Values from Rattay & Wenger (2010).

5.1.3 Potassium Channels

Unlike the two types of sodium channels, the number of potassium channels used in this thesis is slightly larger, and there are three of them. One of them is voltage-gated, one is calcium-gated, and the third is a muscarinic potassium channel. As mentioned earlier, potassium channels are mostly responsible for the second phase of the action potential.

All three types of potassium channels have Hodgkin-Huxley style kinetics, so the currents through the membrane related to potassium channels are calculated as follows (Mainen, et al., 1995):

$$i_K = t_{adjust}\, g_K\, n\, (V - E_K) \qquad (5.7)$$

where similar to sodium channels i_K represents current density related to potassium channels and is given in mA/cm^2. The maximum conductance is represented by g_K, and its unit is $pS/\mu m^2$ (HH and NEURON dimensions are given in mS/cm^2, $1\ mS/cm^2 = 10\ pS/\mu m^2$). The variable n represents the probability for open activation gates. Temperature coefficient t_{adjust} is described in section 5.1.5.

Observing the *1D model* in this thesis, voltage-gated potassium channels are present in the axon hillock, AIS and in the unmyelinated axon. However, the other two types of potassium channels were inserted into the soma and dendrite of the *extended 1D model*.

Reversal potential of $E_K = -90\ mV$ (Rattay & Wenger, 2010; Hu, et al., 2009) is of such value for all three types of potassium channels.

5.1.3.1 K_v Channel

As mentioned earlier, voltage-gated potassium channels are essential in the generation and transmission of the action potential, especially in its second phase. When high membrane potentials occur, voltage-gated potassium channels open and an influx of potassium ions occurs. In the *1D model* in this thesis, voltage-gated potassium channels are located in the axon hillock, AIS and unmyelinated axon.

The activation kinetics of the fast K_v channel is analogous to sodium channels (Mainen, et al., 1995). The following table shows the values for the coefficients A, the slopes k and the half activation voltages $V_{1/2}$.

$A(\alpha)$	0.02	$k(\alpha)$	9	$V_{1/2}(\alpha)$	25 mV
$A(\beta)$	0.002	$k(\beta)$	9	$V_{1/2}(\beta)$	25 mV

Table 3: Values for the coefficients A, the slopes k and the half activation voltages $V_{1/2}$ for K_v channels. Values from Rattay & Wenger (2010).

5.1.3.2 K_m Channel

A small, slow noninactivating potassium current is present in muscarinic potassium channels (Yamada, et al., 1998). This current is almost completely inhibited by muscarinic receptor stimulation and can show prolonged activity at potentials that are between the threshold and rest. It can prevent the formation of an AP and thus affect the adaptation of the spike frequency (Yamada, et al., 1998). Neurotransmitters such as acetylcholine through muscarinic receptors may mediate slow intracellular responses, thus intracellular activation of G-proteins, which can affect cell metabolism and ionic current, is induced by these neurotransmitters (Destexhe, et al., 1998).

This type of potassium channel is present in the soma and in the dendrite of the *extended 1D model*.

As for K_v channel activation, kinetics of the K_m channel is also analogous to sodium channels. The following table shows the values for the coefficients A, the slopes k and the half activation voltages $V_{1/2}$.

$A(\alpha)$	0.001	$k(\alpha)$	9	$V_{1/2}(\alpha)$	-30 mV
$A(\beta)$	0.001	$k(\beta)$	9	$V_{1/2}(\beta)$	-30 mV

Table 4: Values for the coefficients A, the slopes k and the half activation voltages $V_{1/2}$ for K_m channels. Values from Hu, et al. (2009).

5.1.3.3 K_{Ca} Channel

Calcium-dependent potassium channels and its current are not voltage dependent and its time course is relatively short. This current belongs to medium-duration afterhyperpolarization currents (Reuveni, et al., 1993).

The activation is described by the steady-state variable n_∞ and the time constant τ_n, which are calculated in the same way as for sodium channels, and depend on the opening and closing rates α and β which are given as in the following equations (Reuveni, et al., 1993):

$$\alpha = A \cdot [Ca^{2+}] \tag{5.8}$$

$$\beta = A \tag{5.9}$$

The mechanism is taken from Reuveni, et al. (1993) and as stated by Reuveni et al. is based on Pennefather, et al. (1990). This type of potassium channel is found in the soma and dendrite of the *extended 1D model*.

The following table shows the values for the coefficients A.

A(α)	0.01	A(β)	0.02

Table 5: Values for the coefficients A for K_{Ca} channels. Values from Hu, et al. (2009).

5.1.4 Calcium Mechanisms

Two types of calcium mechanisms are used in this thesis. One is a calcium channel activated by high voltage, and the other has two purposes, namely, to enable passive influx of calcium, and active transport of calcium outside the cell by the pump.

5.1.4.1 Ca_v Channel

As already mentioned, this type of calcium channel is activated at a high membrane potential, i.e., it is a high-voltage-gated calcium channel. The concentration gradient of calcium ions is high from the outside to the inside of the cell. Therefore, during activation, an influx of calcium ions occurs. Membrane currents related to calcium channels are calculated according to the same principle as for sodium and potassium channels, as can be seen in the following equation (Reuveni, et al., 1993):

$$i_{Ca} = t_{adjust}\, g_{Ca}\, m^2\, h(V - E_{Ca}) \tag{5.10}$$

The maximum conductance is written as g_{Ca}, and its unit is $pS/\mu m^2$ (HH and NEURON dimensions are given in mS/cm^2, $1\, mS/cm^2 = 10\, pS/\mu m^2$). Temperature coefficient t_{adjust} is described in section 5.1.5. Equivalent to sodium channels, calcium channels also have two variables m and h that represent the probabilities for open activation gates and the probability for open inactivation gates, respectively. Both steady-state variables m_∞ and h_∞, as well as both time constants τ_m and τ_h are calculated in the same way as for m in sodium channels (equations 5.2 and 5.3). Opening and closing rates α and β are given as in the following equations (Reuveni, et al., 1993):

$$\alpha_m(V_m) = \frac{0.55 \cdot (-27 - V_m)}{e^{(-27-V_m)/3.8} - 1} \tag{5.11}$$

$$\beta_m(V_m) = 0.94 \cdot e^{(-75-V_m)/17} \tag{5.12}$$

$$\alpha_h(V_m) = 0.000457 \cdot e^{(-13-V_m)/50} \tag{5.13}$$

$$\beta_h(V_m) = \frac{0.0065}{e^{(-V_m-15)/28} + 1} \tag{5.14}$$

where V_m represents local transmembrane potential.

In this thesis, this type of channel can be found in the soma and dendrite of the *extended 1D model*.

Reversal potential of $E_{Ca} = 140\ mV$ (Hu, et al., 2009) is of such value for this type of calcium channel.

5.1.4.2 Ca_{cm} Mechanism

Another type of calcium mechanism used in this thesis is the internal calcium concentration mechanism. One of its tasks is to enable the passive influx of calcium ions, whereby not all calcium ions in the cytoplasm are taken into account, but only ions in the thin shell beneath the membrane. This simplified process is represented by the kinetics presented in the following equation (Destexhe, et al., 1993):

$$[\dot{Ca}^{2+}]_{in} = \frac{-1000\ I_{ca}}{2\ F\ d} \qquad (5.15)$$

where I_{ca} represents the calcium transmembrane current in mA, Faraday constant is given as $F = 96485.3329\ sA/mol$ and the depth of the shell is given as $d = 0.1\ \mu m$.

Another task of this mechanism is to enable the active transport of calcium ions outside the cell with the help of the ATPase pump. The following equation represents the kinetics of this pump:

$$[\dot{Ca}^{2+}]_{in} = \frac{-K_T\ [Ca^{2+}]_{in}}{[Ca^{2+}]_{in} + K_d} \qquad (5.16)$$

$K_T = 10^{-4}\ mM/ms$ and is proportional to the total concentration of the pump. $K_d = 10^{-4}\ mM$ is dissociation constant and it represents the value of the intracellular calcium ion concentration for which the pump is half activated (Destexhe, et al., 1993).

This mechanism is present in the soma of the *extended 1D model*.

5.1.5 Temperature Adjustment

The original temperature of the model is 23°C, and the Q_{10} parameter is 2.3 (Hu, et al., 2009). Since in this thesis a temperature of 37°C is used for all simulations, it is necessary to apply a temperature coefficient of 3.209 when calculating the conductivity and kinetics of the channel (Rattay & Wenger, 2010). This value was obtained using the general version of the equation for calculating the temperature coefficient, which has the form of the equation (2.5) for calculating the temperature coefficient in the Hodgkin-Huxley model:

$$t_{adjust} = Q_{10}^{\frac{T_{Sim}-T_{Orig}}{10}} \quad (5.17)$$

which gives for $T_{Sim} = 37$ °C, $T_{Orig} = 23$°C and $Q_{10} = 2.3$ value of 3.209.

The temperature coefficient is present in all active mechanisms and channels in this thesis except for the internal calcium mechanism.

5.2 Electrode and Stimulation Modeling

A monopolar microelectrode was used for both intracellular and extracellular stimulation. As mentioned in section 2.2.2 the ground electrode is considered to be relatively far from this electrode, which is modeled here as infinitely distant. In all simulations, whether for intracellular or extracellular stimulation, a train of 10,000 stimulations was used to calculate the spiking efficiency.

5.2.1 Intracellular Stimulation

For intracellular stimulation, a modified version of the, already built into NEURON, *IClamp* function was used, which represents the single pulse current clamp point process. This custom-made function was named *IClamp_burst*[8] and is used to send a train of pulses. The code is written in the NMODL language, so it is necessary to load the *IClamp_burst.mod* file into NEURON. The parameters that can be adjusted in the *IClamp_burst* function are the stimulus delay, the number of stimuli, the duration of the stimulus (duration of the ON phase) and the distance between the end of one and the beginning of the second consecutive stimulus (duration of the OFF phase), unlike the original *IClamp* function where it is possible to define a delay, duration and amplitude of the stimulus.

For intracellular stimulation, exclusively anodic current was used, which was injected into the desired segment through the *IClamp_burst* function. The duration of each stimulation (ON phase) was 0.1 ms.

5.2.2 Extracellular Stimulation

Unlike intracellular stimulation, two types of extracellular stimulation were used in this thesis, namely monophasic and biphasic. As mentioned earlier, the stimulations

[8] The *IClamp_burst* function is adapted to send a train of intracellular stimulation pulses. The origin of "burst" in the name is due to the association with burst fire.

were performed with a monopolar micro electrode, which is represented as a point source in the models. The ground electrode should be far enough, which is here considered to be infinitely far. The electrode can be moved arbitrarily in the x and z directions, but it is not allowed to place the electrode inside the neuron. Since the dynamic range of different parts of the pyramidal cell is mainly investigated in this thesis, and the models extend in the direction of the x axis, the biggest variations in the position of the electrode are in the x direction, while the variations in the z direction are much smaller.

These assumptions made for micro electrode in this thesis overlap with the one made for electrode in section 2.2.2 and thus equation (2.6) defined by Rattay (1990) can be used here for calculating extracellular potential:

$$V_e = \frac{\rho_e I_{el}}{4\pi r} \tag{2.6}$$

where extracellular resistivity $\rho_e = 300\ \Omega \cdot cm$ and electrode current I_{el} was set as needed and is given in μA. r represents the distance from the center of the stimulated segment and is given in μm. Although during stimulation, a small gradient of the extracellular potential will arise along or around the surface of a single segment (depending on the relative position of the segment in relation to the electrode), due to the relatively small diameter and short length of the segments, these differences can be ignored, with the center of the segment being a good approximation for calculation of the potential that affects the entire surface of the segment (Fellner, 2017).

Modeling of extracellular stimulation was done in a similar way described in Fellner (2017). Thereby, two mechanisms are loaded into NEURON. The first is NEURON's native *extracellular* mechanism. It extends the model with extracellular potentials by adding two additional membrane layers to the section. In order for the *extracellular* mechanism to be used for extracellular stimulation, it needs extensions. It is the *xtra.mod* mechanism, which is the second mechanism loaded into NEURON.

Extracellular potential V_e is calculated via *xtra*'s transfer resistance R_x, which depends on the extracellular resistivity ρ_e and the distance of the electrode from the stimulation site $r = \sqrt{x^2 + z^2}$, and can be calculated in the following manner:

$$R_x = \frac{\rho_e}{4\pi r} \tag{5.18}$$

Therefore, formula (2.6) takes the following form:

$$V_e = R_x \cdot i_{st} \cdot A \tag{5.19}$$

where i_{st} is the stimulus current density given in mA/cm^2 and A is the respective segment area in μm^2. R_x units are given in $M\Omega$.

In order to stimulate with a train of pulses, it was first necessary to create two vectors, whether it is a monophasic or biphasic stimulation. The first one contains the amplitude of the stimulation current, and the second the exact times when the stimulus should be active. Through NEURON's *Vector.play()* function, the values of the vector of current amplitudes are assigned to *xtra*'s global variable i_s for the times given in the second vector.

Unlike the general computer simulation environments such as NEURON and Python used here, where the modeling of extracellular stimulation works in two stages, where first it is necessary to calculate the extracellular potential V_e, and then transfer it to the multicompartment model, the finite element method frameworks (such as COMSOL) can combine it into one program, which is generally much more precise, but it is very computationally expensive and therefore not so much intended for stochastic influences (Fellner, et al., 2022).

For extracellular stimulation, cathodic current was used for monophasic and anodic followed by cathodic current (+/-) for biphasic stimulation. The reason for anodic-first instead of cathodic-first biphasic stimulation is that it is much easier to distinguish AP from artifacts that way (Meng, et al., 2018). The duration of each pulse was $0.1\ ms$ for monophasic and $0.1\ ms$ for each phase of biphasic stimulation, which gives a total of $0.2\ ms$.

5.3 Adding Noise to Models

Since the model used in this thesis is a deterministic Hodgkin-Huxley based model, it is necessary to insert a stochastic component into the model in order to be able to investigate the phenomenon of spiking efficiency at all. This can be achieved in the manner described in section 3 by injecting the noisy current I_{noise} into each active compartment of the model (Rattay & Tanzer, 2022b). According to equation (3.1), the I_{noise} current is calculated as $I_{noise} = GAUSS \cdot k_{noise}\sqrt{A_n \cdot g_{Na}}$.

The way in which noise was added in this thesis can be seen in Figure 17. Under (a) is presented a sketch of the 1D model used in the thesis, where parts of the cell with passive membrane properties are represented in gray, and with active membrane properties in red and salmon color. Red and salmon color indicate high and low

amounts of sodium channels, respectively. Under (b) the electrical circuit equivalent of the 1D model is presented. Only 4 segments are shown, with omitted segments marked with 3 black dots. Intracellular resistance R, membrane capacitance C_m, membrane conductance G_m and extracellular V_e and intracellular V_i potentials define currents. The lightning-shaped arrows show the injection of I_{noise} current into the segments and are not present in the internodes, which have passive membrane properties.

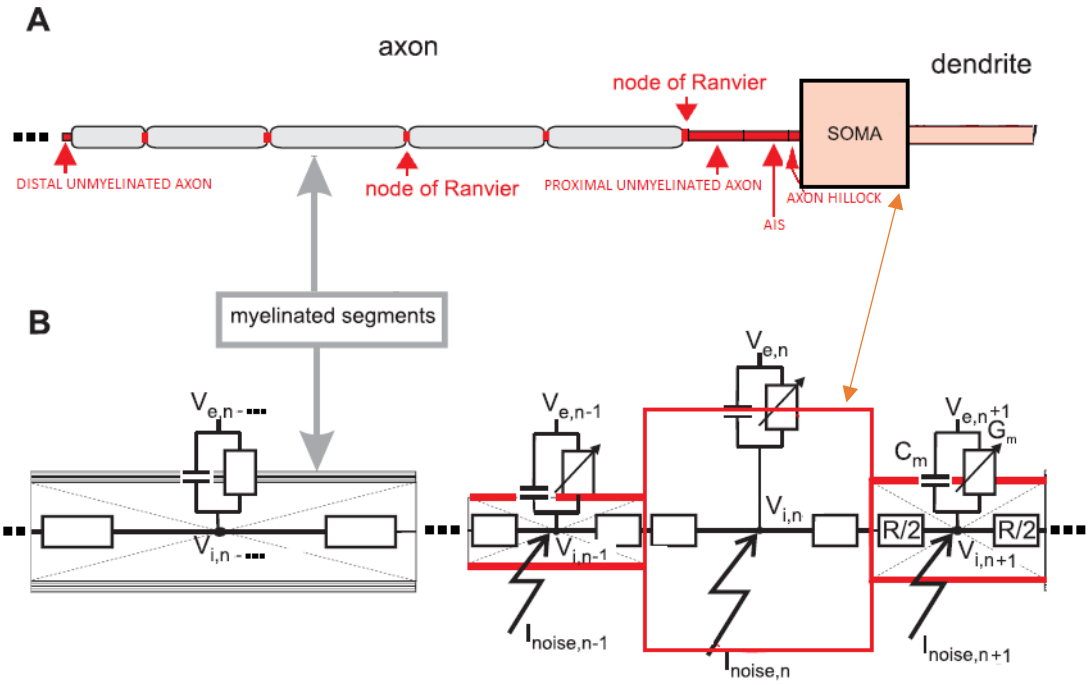

Figure 17: Sketch of the *1D model* used in this thesis. The proportions are not true to size. (a) Geometry of 1D model. Sections with a passive membrane, i.e., internodes, are shown in gray, and there are no sodium channels in them. Sections with an active membrane are represented in red and salmon color. Sections with a large number of sodium channels are represented in red, and sections with a small number of sodium channels are represented in salmon color. (b) Electrical circuit equivalent of the *1D model*. Only 4 segments are shown, and the omitted segments are marked with 3 black dots. Intracellular resistance R, membrane capacitance C_m, membrane conductance G_m and extracellular V_e and intracellular V_i potentials define currents. Noise is injected into segments with an active membrane in the form of noisy current I_{noise}. Figure modified from Rattay & Tanzer (2022b).

Since there are two types of sodium channels in the models in this thesis ($Na_{1.2}$ and $Na_{1.6}$), there are therefore two maximal sodium conductances $g_{Na1.2}$ and $g_{Na1.6}$. Therefore, equation (3.1) for calculating noisy current had to be modified and now has following form:

$$I_{noise,n} = GAUSS \cdot k_{noise}\sqrt{A_n \cdot (g_{Na1.2,n} + g_{Na1.6,n})} \qquad (5.20)$$

where $I_{noise,n}$ represents the noisy current injected into segment n with active membrane properties. As described in section 3, standard factor k_{noise} is common to all compartments and is given in $\mu A\ mS^{-1/2}$. A_n represents the area of the membrane of the segment n in cm^2, while $g_{Na1.2}$ and $g_{Na1.6}$ are maximal sodium conductances per square unit given in $mS\ cm^{-2}$.

It turned out that adding noise significantly increases computational costs, i.e., slows down simulations. As a countermeasure, noise should be added early enough before stimulation for transient to be over and should last long enough to cover all significant changes caused by stimulation in all parts of the cell. Accordingly, noise was added 3 ms before each stimulation and lasted 10 ms. Those times were chosen because it was found that no significant differences in spiking efficiency can be established for those times compared to when noise is present during the entire simulation, but the computational costs have decreased significantly.

As already mentioned in section 5.2, for both intracellular and extracellular stimulation, a train of 10,000 pulses was sent. Therefore, it is also necessary to send 10,000 noise pulses, with each pulse starting 3 ms before each stimulation and lasting 10 ms. For that, the custom made *IClamp_burst* function mentioned in section 5.2.1 was used. First, it was necessary to create two vectors. The first one contains the random values of the noisy current $I_{noise,n}$ calculated according to equation (5.20), and the second one contains the time points when noise should be injected. In order to inject noise in the desired segment n, NURON's *Vector.play()* function was used. With it, the values of the vector with the amplitudes of the noisy current $I_{noise,n}$ are assigned to the current that is injected into the segment at the exact times defined in the second vector.

As for the $GAUSS$ variable, which represents a normal distribution whose value changes with transmission time Dt, its mean value μ and standard deviation σ are, as described in section 3, 0 and 1, respectively. The value of the standard factor k_{noise} was chosen to be 0.0038 $\mu A\ mS^{-1/2}$ (Rattay & Tanzer, 2022b) and it does not need to be further adjusted as described by equation (3.2) because during the presence of noise during simulations $Dt = 0.0025\ ms$. Table 6 presents the values of all the parameters needed for noise modeling in an overview.

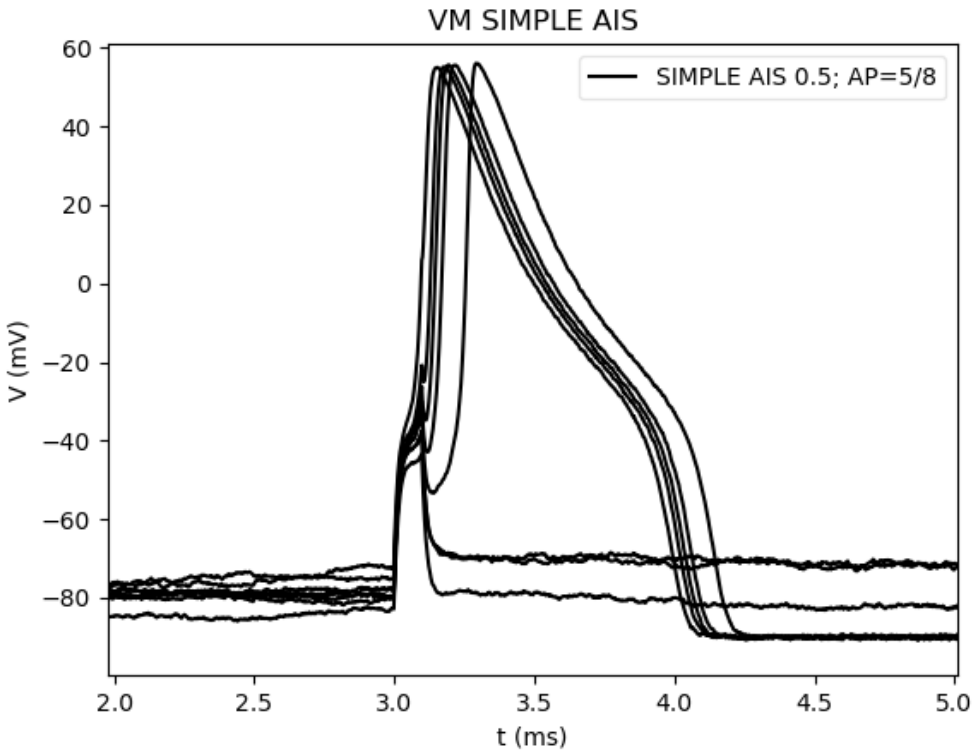

Figure 18: Spiking efficiency of the *single section model*. Extracellular monophasic cathodic stimulation, with a stimulus at the threshold. The distance of the electrode is 50 μm, and it is placed in the middle of the section. 5 action potentials were generated from 8 sent pulses. A superposition of consecutive responses is presented. A similar behavior can be seen as from the experiment (Verveen & Derksen, 1968) shown in Figure 11 and simulation experiments (Rattay & Tanzer, 2022b).

Noise with the parameters given in Table 6 was injected into all segments of the *single section model* described in section 5.4.1. During extracellular cathodic monophasic stimulation with a train of 8 pulses, 5 action potentials were generated (see Figure 18). Since the model behaves similarly for stimulation at the threshold as in experiments from Verveen & Derksen (1968) (Figure 11) and simulation experiments (Rattay & Tanzer, 2022b), it can be assumed that noise is modeled correctly.

k_{noise}	$0.0038\ \mu A\ mS^{-1/2}$	Start noise before stimulus	$3\ ms$
μ (GAUSS)	0		
σ (GAUSS)	1	Noise duration	$10\ ms$

Table 6: Values for the standard noise factor k_{noise}, mean μ and standard deviation σ of the $Gauss$ variable which changes its value with Dt. Noise starts 3 ms before each stimulation and lasts 10 ms.

5.4 Models

Three models with different degrees of complexity are used in this thesis. A detailed description of the models is presented below in this section.

5.4.1 Single Section Model

The *single section model* is based on the axon initial segment of the simplified pyramidal cell model described in Rattay & Wenger (2010), and represents its elongated version. As the name suggests, the model consists of a single section represented in Figure 19 which is further divided into seven segments. Its diameter is $d = 1.22\ \mu m$, and its length is $L = 100\ \mu m$, in contrast to the original length of $50\ \mu m$.

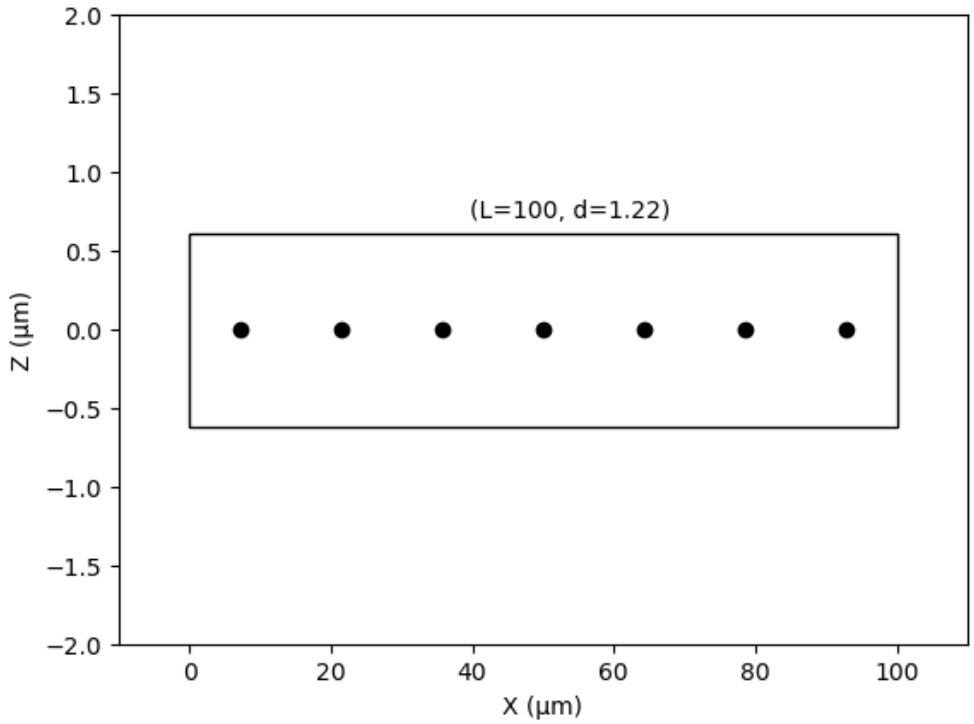

Figure 19: Geometry of the cylindrical *single section model* in x and z coordinates. The model consists of a single section, which is further divided into 7 segments. Centers of segments are marked with black dots. The units of diameter d and length L are μm.

This model contains three types of active ion channels. These are $Na_v1.2$, $Na_v1.6$ and K_v channels described in previous sections. The values of maximum sodium conductances are $g_{Na1.2} = 100\ mS/cm^2$, $g_{Na1.6} = 320\ mS/cm^2$ and $g_{Kv} =$

$100\ mS/cm^2$. Wherein the values for the coefficients A, the slopes k, the half (in)activation voltages $V_{1/2}$ and the reversal potentials are described in sections 5.1.2 and 5.1.3.1.

The values of the passive mechanism are for specific membrane capacitance $C_m = 1\ \mu F/cm^2$, specific leakage conductance $g_{pas} = 0.033\ mS/cm^2$, specific axial resistivity $\rho_a = 150\ \Omega \cdot cm$ and leakage reversal potential $E_{pas} = -70\ mV$. Extracellular resistivity is $\rho_e = 300\ \Omega \cdot cm$.

In Table 7, the electrophysiological properties of the model are summarized, except for the values of the coefficients A, the slopes k and the half (in)activation voltages $V_{1/2}$.

g_{pas}	$0.033\ mS/cm^2$
C_m	$1\ \mu F/cm^2$
ρ_a	$150\ \Omega \cdot cm$
E_{pas}	$-70\ mV$
$g_{Na1.2}$	$100\ mS/cm^2$
$g_{Na1.6}$	$320\ mS/cm^2$
E_{Na}	$60\ mV$
g_{Kv}	$100\ mS/cm^2$
E_K	$-90\ mV$
ρ_e	$300\ \Omega \cdot cm$

Table 7: Summarized electrophysiological properties of the *single section model*. The values of the coefficients *A*, the slopes *k* and the half (in)activation voltages $V_{1/2}$ are not represented (see sections 5.1.2 and 5.1.3.1). Values based on Rattay & Wenger (2010).

5.4.2 Axon Model

The *axon model* is more complex than the *single section* model in the sense that unlike one section of the *single section* model, the *axon model* consists of two types of sections connected alternately, with a total of 101 sections. Those sections represent the nodes of Ranvier and the myelinated internodes of the axon. The model is based

on the models described in Rattay & Tanzer (2022b), Rattay & Wenger (2010) and Hu, et al. (2009).

As already mentioned, the model consists of 101 sections as in Rattay & Tanzer (2022b). Node of Ranvier and internode sections are connected alternately, with the first and last sections being nodes of Ranvier. Therefore, the model consists of 51 sections of the node of Ranvier and 50 sections of the internode. Each section consists of a single segment. Regarding the geometry, the diameter of the axon along its entire length is $d = 1\ um$, while the lengths of the node of Ranvier and the internode are $1\ \mu m$ and $100\ \mu m$, respectively (see Figure 20).

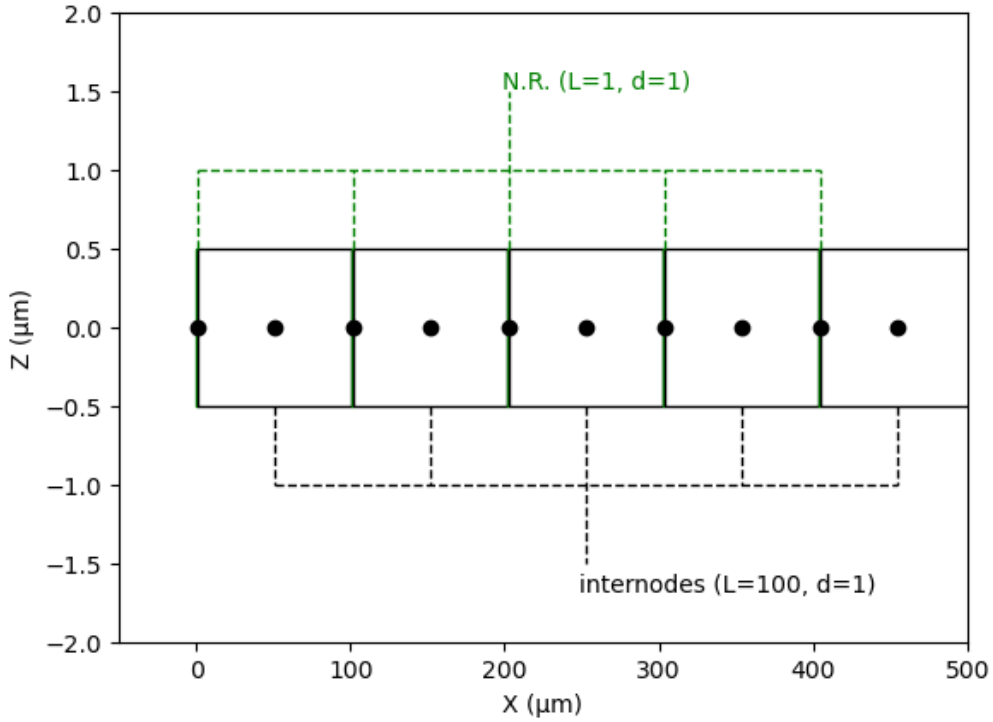

Figure 20: The geometry of the *axon model* in x and z coordinates. N. R.: nodes of Ranvier (green). The model consists of alternately connected 51 nodes and 50 internodes, i.e., a total of 101 sections. The leftmost 10 sections are presented. Every section is cylindrical and composed of a single segment which is represented by a black dot. The units of diameters d and lengths L are μm.

This model contains only one type of active ion channels, $Na_v1.6$ (see section 5.1.2.1). They are located in the nodes of Ranvier. Their maximum sodium conductance is $g_{Na1.6} = 160\ mS/cm^2$, while the sodium potential reversal is $E_{Na} = 60$ mV. Values for the coefficients A, the slopes k and the half (in)activation voltages $V_{1/2}$ are as described in section 5.1.2.1. The values of the passive properties of nodes of Ranvier are: specific membrane capacitance $C_m = 1\ \mu F/cm^2$, specific

leakage conductance $g_{pas} = 0.033\ mS/cm^2$, specific axial resistivity $\rho_a = 150\ \Omega \cdot cm$ and leakage reversal potential $E_{pas} = -70\ mV$.

The myelination of internodes is represented by 17 membrane layers, where each layer has a conductance of $1\ mS/cm^2$ and a capacitance of $1\ mF/cm^2$. The values of specific axial resistivity and leakage reversal potential of internodes are unchanged compared to nodes and have values of $\rho_a = 150\ \Omega \cdot cm$ and $E_{pas} = -70\ mV$, respectively.

The summarized values of the electrophysiological properties of the *axon model* are shown in Table 8. The extracellular resistivity is $\rho_e = 300\ \Omega \cdot cm$. All electrophysiological properties of the *axon model* were chosen as in the model described in Rattay & Wenger (2010), except that the K_v channel was omitted as in the model from Hu, et al. (2009).

Property	Node of Ranvier	Internode
g_{pas}	$0.033\ mS/cm^2$	$\frac{1}{17}\ \mu S/cm^2$
C_m	$1\ \mu F/cm^2$	$\frac{1}{17}\ \mu F/cm^2$
ρ_a	$150\ \Omega \cdot cm$	$150\ \Omega \cdot cm$
E_{pas}	$-70\ mV$	$70\ mV$
$g_{Na1.6}$	$160\ mS/cm^2$	-
E_{Na}	$60\ mV$	-

Table 8: Summarized electrophysiological properties of two building sections of the *axon model*, nodes of Ranvier and internodes. The values of the coefficients A, the slopes k and the half (in)activation voltages $V_{1/2}$ are not represented (see section 5.1.2.2). Each of the 17 membrane layers that make up the myelination of internodes has a conductance of $1\ mS/cm^2$ and a capacitance of $1\ mF/cm^2$. The value of extracellular resistivity is $\rho_e = 300\ \Omega \cdot cm$. Values based on Rattay & Wenger (2010).

5.4.3 1D Model

The most complex model in this thesis is the *1D model*. It contains elements of the previously described *single section model* and *axon model* and represents a simplified version of the pyramidal cell. As for the geometry, the simple compartment model with straight line axis described in Rattay & Wenger (2010) was used. The

electrophysiological properties of the model are based on Rattay & Wenger (2010) and Hu, et al. (2009).

The model is built by connecting 8 different sections, some of which are repeated. All sections are cylindrical (see Figure 21). A single dendrite that does not branch has a diameter of $d = 5\ \mu m$ and a length of $L = 500\ \mu m$. A soma of equal diameter and length $d = L = 20\ um$ is attached to it. Then comes the axon hillock with a diameter of $d = 3.1\ \mu m$ and a length of $L = 10\ \mu m$. The axon initial segment with dimensions $d = 1.22\ \mu m$ and $L = 50\ \mu m$ is attached to it. After it goes an unmyelinated axon with dimensions $d = 1\ \mu m$ and $L = 200\ \mu m$, to which five repetitions of nodes followed by internodes are connected. Both nodes and internodes have the same diameter $d = 1\ \mu m$, with the internode being 100 times longer than the node with lengths of $L = 100\ \mu m$ and $L = 1\ \mu m$, respectively. At the very end, there is an unmyelinated terminal measuring $d = 1\ \mu m$ and $L = 50\ \mu m$. Unmyelinated axon consists of 20 segments, dendrite of 14, AIS and distal unmyelinated axon of 3 each, axon hillock of 2, while soma and all nodes of Ranvier and internodes consist of a single segment each.

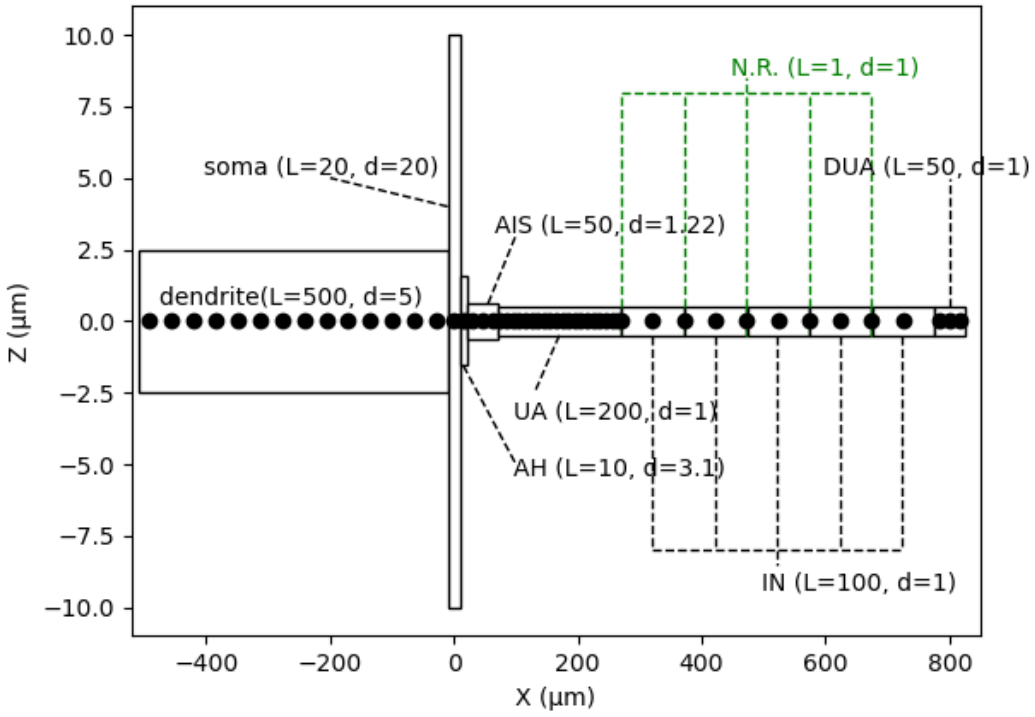

Figure 21: The geometry of the *1D model* in x and z coordinates. AH: axon hillock, UA: unmyelinated axon, IN: internode, N.R.: node of Ranvier (green), DUA: distal unmyelinated axon. All sections are cylindrical. Centers of each segment are marked with a black dot. The units of lengths L and diameters d are μm.

The two main subtypes of *1D model*s in this thesis are the *standard 1D model*, also referred to simply as *1D model* or *reduced 1D model*, and the *extended 1D model*. They differ in electrophysiological properties, more precisely the *extended 1D model* has additional active ion channels and mechanisms compared to the *standard 1D model*.

The passive properties of both *standard 1D model* and *extended 1D model* are the same. All active compartments have values of specific membrane capacitance $C_m = 1\,\mu F/cm^2$, specific leakage conductance $g_{pas} = 0.033\,mS/cm^2$, specific axial resistivity $\rho_a = 150\,\Omega \cdot cm$ and leakage reversal potential $E_{pas} = -70\,mV$. As for *axon model* (see section 5.4.2) myelination of the internodes is simulated by adding 17 layers of the membrane, where each layer has a conductance of $1\,mS/cm^2$ and a capacitance of $1\,mF/cm^2$.

Standard (reduced) 1D model has three types of active ion channels, namely $Na_v1.2$, $Na_v1.6$ and K_v channels. Their distribution differs significantly depending on the part of the cell. There are no $Na_v1.6$ channels in the soma and dendrite, while the concentration of $Na_v1.2$ and K_v channels is relatively low and their maximum conductances are $g_{Na1.2} = 8\,mS/cm^2$ and $g_{Kv} = 10\,mS/cm^2$ for both the soma and the dendrite. $Na_v1.2$ and K_v channels are also installed in the axon hillock, only with a higher concentration, and their maximum conductances are $g_{Na1.2} = 320\,mS/cm^2$ and $g_{Kv} = 100\,mS/cm^2$. AIS contains all three types of channels and their maximum conductances are $g_{Na1.2} = 100\,mS/cm^2$, $g_{Na1.6} = 320\,mS/cm^2$ and $g_{Kv} = 100\,mS/cm^2$. Unmyelinated axons possess $Na_v1.6$ and K_v channels with maximum conductances of $g_{Na1.6} = 300\,mS/cm^2$ and $g_{Kv} = 150\,mS/cm^2$. Nodes of Ranvier also have $Na_v1.6$ and K_v channels, and their maximum conductances are $g_{Na1.6} = 160\,mS/cm^2$ and $g_{Kv} = 20\,mS/cm^2$. Reversal potentials for sodium and potassium ions are $E_{Na} = 60\,mV$ and $E_K = -90\,mV$, respectively. The electrophysiological properties of all sections of the *standard 1D model* are similar to the model described in Rattay & Wenger (2010), except that the K_v channel is excluded from the node of Ranvier as in the model from Hu, et al. (2009).

With the *extended 1D model*, there are no changes regarding already existing mechanisms in the reduced version, but additional mechanisms and channels have been inserted into the model. These are the K_m, K_{Ca} and Ca_v channels that are found in the soma and in the dendrite and the Ca_{cm} mechanism located only in the soma. Their maximum conductances are $g_{Km} = 0.3\,mS/cm^2$, $g_{KCa} = 3\,mS/cm^2$ and $g_{Cav} = 0.3\,mS/cm^2$ according to Hu, et al. (2009). Reversal potentials for potassium and calcium ions are $E_K = -90\,mV$ and $E_{Ca} = 140\,mV$, respectively. Other

parameters such as values of the coefficients A, the slopes k, the half (in)activation voltages $V_{1/2}$ etc. are found in sections 5.1.3.2, 5.1.3.3, 5.1.4.1 and 5.1.4.2.

Table 9 shows the most significant electrophysiological values for both *standard 1D model* and *extended 1D model*.

Property [unit]	Dend	Soma	AH	AIS	Unmy	Node	Intern
g_{pas} $[mS/cm^2]$	0.033	0.033	0.033	0.033	0.033	0.033	1/17
C_m $[\mu F/cm^2]$	1	1	1	1	1	1	1/17
ρ_a $[\Omega \cdot cm]$	150	150	150	150	150	150	150
E_{pas} $[mV]$	-70	-70	-70	-70	-70	-70	-70
$g_{Na1.2}$ $[mS/cm^2]$	8	8	320	100	-	-	-
$g_{Na1.6}$ $[mS/cm^2]$	10	10	-	320	300	160	-
E_{Na} $[mV]$	60	60	60	60	60	60	-
g_{Kv} $[mS/cm^2]$	-	-	100	100	150	-	-
g_{Km} $[mS/cm^2]$	0.03	0.03	-	-	-	-	-
g_{KCa} $[mS/cm^2]$	0.3	0.3	-	-	-	-	-
E_K $[mV]$	-90	-90	-90	-90	-90	-	-
g_{Cav} $[mS/cm^2]$	0.03	0.03					-
E_{Ca} $[mV]$	140	140	-	-	-	-	-

Table 9: Summarized electrophysiological properties of *standard 1D model* (white cells) and *extended 1D model* (white and green cells). Dend: dendrite, AH: axon hillock, Unmy: unmyelinated axon, Intern: internode. The values of the coefficients A, the slopes k, the half (in)activation voltages $V_{1/2}$ etc. are not represented (see section 5.1). Each of the 17 membrane layers that make up the myelination of internodes has a conductance of 1 mS/cm^2 and a capacitance of 1 mF/cm^2. The Ca_{cm} mechanism is present only in the soma of the *extended 1D model*. The value of extracellular resistivity is $\rho_e = 300\ \Omega \cdot cm$. All values in white cells are based on Rattay & Wenger (2010) except from g_{Kv} which is, together with values in green cells based on Hu, et al. (2009).

5.5 Examination of spiking efficiency

Dynamic range (DR) and relative spread (RS) were used to quantify spiking efficiency. DR, as described in section 3 defines the range of stimulus intensity in which spiking efficiency increases from 0.1 (10%) to 0.9 (90%) (Shepherd & Javel, 1997), while RS is defined as DR normalized to threshold divided by 2.56 (Rattay & Tanzer, 2022b).

The usual way of obtaining DR would be as described in section 3. Trains of pulses of different amplitudes are sent. The amplitudes are such that they cause spiking efficiency of 0, then increased in small intervals until spiking efficiency reaches 1. The number of train of pulses determines the number of points (in Figure 22 there are 5 points marked with black X, see also Figure 14) for which cumulative Gaussian fitting is performed (black curve in Figure 22). Cumulative Gaussian curve behaves almost linearly for spiking efficiencies between 0.3 and 0.7, and this feature can be used for a simpler way of calculating DR. This is done through the *2-point method* for calculating the approximate value of DR.

Calculation of DR via the *2-point method* is performed in the following way. First, it is necessary to determine the stimulation threshold (current amplitude) at which an action potential occurs without injected noise. Then simulations are performed with injected noise, during which 2 trains of pulses are sent. The first has an amplitude I_1, which is below the threshold, and causes spiking efficiency f_1 between 30% and 50%. The second one has an amplitude I_2, which is above the threshold, and causes spiking efficiency f_2 between 50% and 70%. After running the simulations, two points with values (I_1, f_1) and (I_2, f_2) are obtained through which the line is fitted (those two points are represented by brown X in Figure 22, while the mentioned line is also brown). Since the cumulative Gaussian curve behaves approximately linearly for spiking efficiency in the range of 0.3 to 0.7, the line fitted through the calculated 2 points also represents the tangent to the turning point of the cumulative Gaussian curve (where spiking efficiency is 0.5). As can be seen in Figure 22 the fitted line has the same stimulus intensities at spiking efficiencies of 0 and 1 as a cumulative Gaussian curve at spiking efficiencies of 0.1 and 0.9, respectively. Since DR, according to the previously mentioned definition, is the range of stimulus intensity in which spiking efficiency increases from 0.1 to 0.9, it is also possible to calculate it as the difference in the intensity of the fitted line at a spiking efficiency of 0 and at a spiking efficiency of 1. This can be described by the following equation:

$$DR = \frac{I_2 - I_1}{f_2 - f_1} \tag{5.21}$$

where DR has the same units as the stimulus intensity (usually μA). In order to determine the DR normalized to threshold DR_N, it is necessary to divide the obtained DR value by the threshold value of the stimulus intensity $I_{0.5}$. That gives:

$$DR_N = \frac{DR}{I_{0.5}} \tag{5.22}$$

and does not have a unit, but is often converted into percentages. Finally, RS can be calculated by dividing DR normalized to threshold by 2.56 (Rattay & Tanzer, 2022b):

$$RS = \frac{DR_N}{2.56} \tag{5.23}$$

and has the same units as DR_N, i.e., percentages.

The more pulses used to calculate spiking efficiencies for given stimulus intensities, the more accurate the approximation of DR via the *2-point* method. Therefore, in this thesis, a train of 10,000 pulses is used to calculate each point.

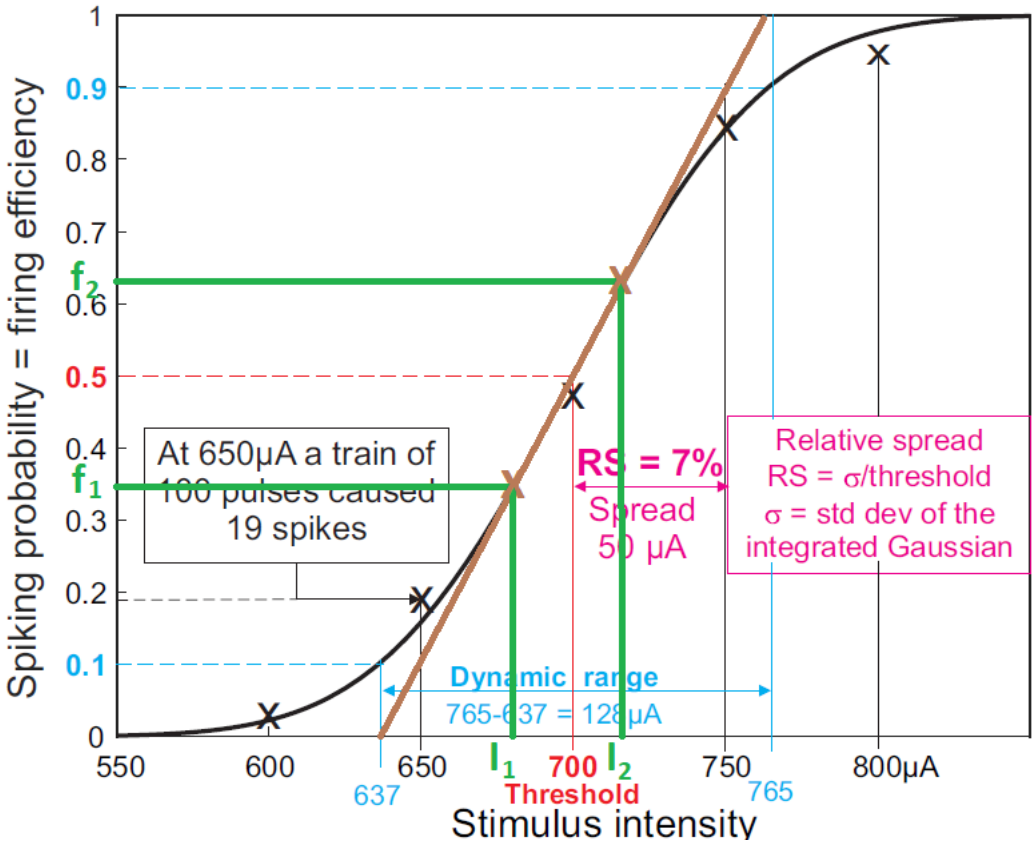

Figure 22: *2-point method* (in comparison with cumulative Gaussian curve fitting; black curve). Two points (I_1, f_1) and (I_2, f_2) (represented by brown X) are calculated by sending two trains of pulses with spiking

efficiencies ranging from 0.3 to 0.5 and from 0.5 to 0.7, respectively (cumulative Gaussian curve behaves approximately linearly for spiking efficiency in the range of 0.3 to 0.7). A straight line is fitted through these points (brown line), which also represents the tangent to the cumulative Gaussian curve at its turning point. For spiking efficiency values of 0 and 1, this line has the same stimulus intensity values as the fitted cumulative Gaussian curve for spiking efficiency values of 0.1 and 0.9, respectively. This can be used to calculate DR according to formula (5.21). Figure modified from Rattay & Tanzer (2022b).

5.6 Common Simulation Procedures and Parameters

This section describes the procedures and general parameters that apply to all three models in this thesis.

All simulations were performed at a temperature of 37°C. At the beginning of each simulation, before the first stimulus, there was a delay of 850 ms, so that the currents in all compartments equalize and the model reaches a stable state. The duration of each monophasic stimulus, whether intracellular or extracellular, was 0.1 ms, while the duration of each biphasic stimulus was 0.1 ms per phase, which gives 0.2 ms in total. Extracellular stimulations were exclusively cathodic and performed both at lower and upper thresholds. Intracellular stimulations were anodic. All simulations contained a train of 10,000 pulses, where the distance between successive pulses was 350 ms. Two simulations with a train of 10,000 pulses are required to obtain one DR value. In order to reduce computational costs, two different time steps Δt, "fine" and "rough", were used. For initial delay and in the intervals between the stimuli, $\Delta t_2 = 1\ ms$ was used. A finer time step $\Delta t_1 = 0.0025\ ms$ started 3 ms before each pulse and lasted 10 ms. Noise was injected in every active compartment only during the fine time step as described in 5.3.

DR was calculated for different electrode positions (different parts of the model were stimulated), while the geometric and electrophysiological properties of the model were also changed. Since the models were developed to support parallel computing, all simulations were performed on a 60-core server at the Vienna University of Technology due to the computational complexity of the simulations. All the parameters of the simulations were pre-designed and the thresholds were found in advance, so it was sufficient to run the simulations only once and collect the results at the end.

6 Results

In this section, the results of various simulation experiments are presented, through which the change in spiking efficiency, i.e., dynamic range (DR), was examined. Two pairs of stimulation current amplitudes and spiking efficiencies are needed to calculate DR (the detailed procedure for calculating DR is explained in section 5.5). For this reason, to determine one DR, two simulations with stimuli of different amplitudes were always performed, and during each simulation a train of 10,000 pulses was sent.

Simulation experiments were performed on different models, starting from simpler to more complex ones. Those are *single section model*, *axon model*, *standard 1D model* and *extended 1D model*. *The single section model* and the *axon model* are essentially the building blocks of the *1D model* and were used to gain insight into the basic behaviors of DR, which can facilitate understanding of the *1D model*.

During the simulations, various geometric and electrophysiological parameters of the models were changed, such as the diameters and number of active channels of a certain section, as well as the position and type of stimulation. Two electrode distances from the model axis were used, $50\,\mu m$ and $100\,\mu m$. Stimulations were performed extracellularly monophasically, in which the stimulus current was cathodic (-), biphasic, in which the stimulus current was anodic followed by cathodic (+/-), and intracellularly monophasic, in which the stimulus current was anodic (+). Cathodic stimulation at upper threshold was also performed. The duration of each pulse was $1\,ms$, while the distance between consecutive pulses was $350\,ms$.

Dynamic range is in the results in its normalized to threshold form, it is marked with *DR*, and it is given as a percentage.

6.1 Single Section Model

The *single section model* represents an elongated version of the AIS of the *1D model* (see Figure 19). On this model, a change in DR was observed if its diameter is doubled from $d = 1.22\,\mu m$ to $d = 2.44\,\mu m$. According to Verveen (1962), there is a relationship between RS and diameter, where with an increase in diameter, RS, and therefore DR should decrease. A monophasic cathodic (-) stimulus was used, while the electrode distance was $z = 50\,\mu m$. The central part of the model was stimulated, i.e.,

at the position $x = 50\ \mu m$. The change in transmembrane voltage, through which action potentials are detected and therefore spiking efficiency is determined, was measured at the end of the model (in the last segment).

With the increase in diameter, the threshold decreased slightly, while the DR decreased noticeably (Figure 23). The diameter-DR relationship appears to match the theory presented by Verveen (1962).

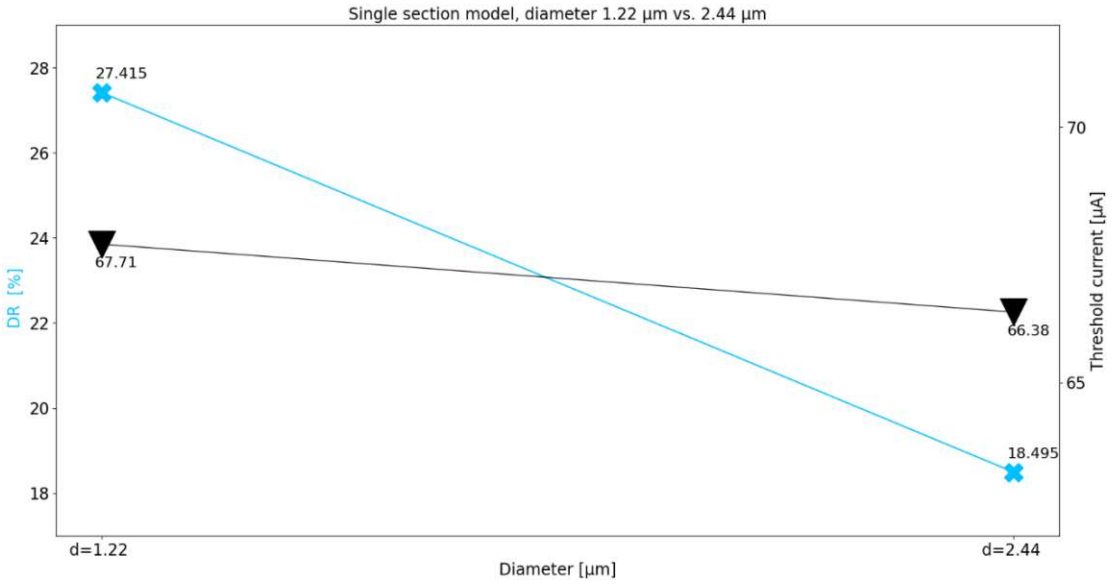

Figure 23: Single section model. DR (cyan) and threshold (black) for diameter $d = 1.22\ \mu m$ vs. $d = 2.44\ \mu m$. Monophasic (-) stimulation, electrode distance is $d = 50\ \mu m$. When doubling the diameter, DR decreased noticeably, while threshold decreased slightly. The relationship between diameter and DR appears to correspond to the theory presented in Verveen (1962) that as diameter increases, RS (and therefore DR) decreases.

6.2 Axon Model

The *axon model* represents an elongated version of the part of the *1D model* where the nodes of Ranvier and internodes alternate. Unlike the *1D model* which has 5 nodes and 5 internodes, the *axon model* has 51 nodes and 50 internodes (see Figure 20). The model was stimulated by monophasic cathodic (-) current above the 26th node at the electrode distance $z = 100\ \mu m$. APs are detected in the last node of Ranvier. In addition to determining the DR, it was observed how the transmembrane voltage changes along the entire axon after stimulation.

DR for the above-mentioned setting of the simulation experiment is $DR = 3.934\%$, while the threshold is 47 μA. The transmission and initiation site of the AP are shown in Figure 24.

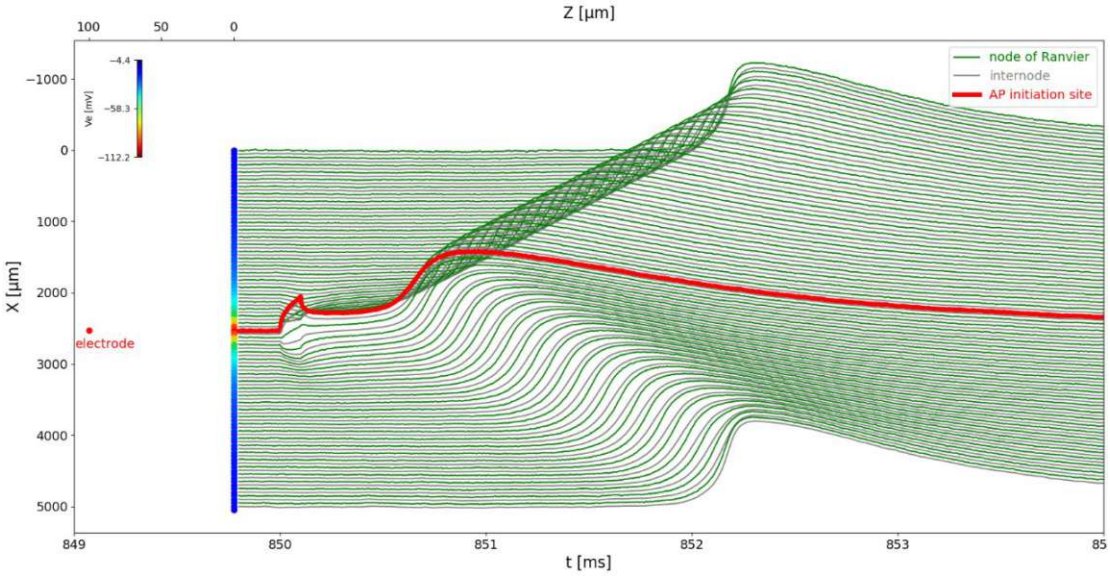

Figure 24: AP initiation site. *Axon model*. The axon was stimulated above the 26th node of Ranvier with a monophasic (-) pulse, the electrode distance is $z = 100\ \mu m$. The time axis (x-axis) and the x-position axis (y-axis) are used to represent the temporal and spatial change of the transmembrane voltage (propagation of AP), and this is represented on the plot by green (node of Ranvier) and gray (internode) lines. The line of the segment where the AP was initiated is thick and red. On the left side, the centers of the segments are arranged vertically, they are represented by dots of different colors depending on the strength of the extracellular potential (color bar is in the upper left corner) caused by the electrode (red dot). For the position of the electrode and the centers of the segments, the x-axis (y-axis on the plot) and z-axis (upper x-axis) are used.

6.3 Standard 1D Model

Most simulations were performed with the *standard 1D model*, and all further variations were compared to it, hence the "standard" in its name. Detection of the change in transmembrane voltage in the *standard 1D model*, and therefore the action potentials responsible for spiking efficiency and DR, is performed in the distal unmyelinated axon.

For the first insight into the change of DR in relation to the stimulated section of the cell, the position of the electrode was moved along the x axis, while the distance of the electrodes along the z axis remained constant and was set to $z = 100\ \mu m$. Different parts of the cell were thereby stimulated and are presented on the x-axis of Figure 25. Stimulations were performed at two points outside the dendritic tree, at the positions $x = -600\ \mu m$ and $x = -550\ \mu m$. The dendrite was stimulated at three points $x = -500\ \mu m$, $x = -300\ \mu m$ and $x = -100\ \mu m$. The soma was stimulated at its border with the dendrite, at its middle and at the border with the axon hillock with electrode positions $x = -10\ \mu m$, $x = 0\ \mu m$ and $x = 10\ \mu m$, respectively. The axon hillock is stimulated at its middle, where $x = 15\ \mu m$. AIS was stimulated at the border with the

axon hillock, at its middle and at the border with the unmyelinated axon, at x positions $x = 20\ \mu m$, $x = 45\ \mu m$ and $x = 70\ \mu m$. Unmyelinated axon, the first four nodes of Ranvier and the first three internodes were stimulated at the positions $x = 170\ \mu m$, $x = 270\ \mu m$, $x = 321\ \mu m$, $x = 371\ \mu m$, $x = 422\ \mu m$, $x = 472\ \mu m$, $x = 523\ \mu m$ and $x = 573\ \mu m$. The cell is stimulated by a monophasic, cathodic (-) train of pulses.

Threshold current (black line in Figure 25) is highest outside the dendritic tree and at the dendrite, while it decreases approaching AIS and nodes of Ranvier. The minimum threshold is at the third node of Ranvier. Threshold behaves very similarly to the threshold presented in Figure 3a from Rattay & Wenger (2010) publication. DR (cyan line in Figure 25) is the lowest outside the dendritic tree and at the dendrite and increases approaching the first node of Ranvier, where it reaches its maximum. After the first node of Ranvier, DR drops sharply and then rises slightly again. RS is also presented (magenta line in Figure 25), which by its definition follows the behavior of DR.

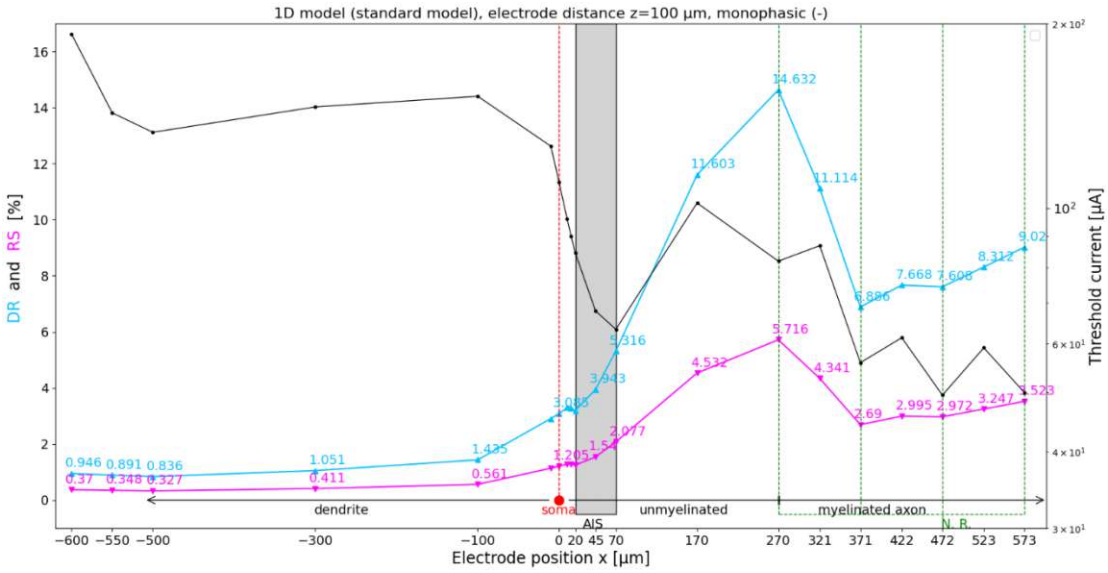

Figure 25: *Standard 1D model*. Monophasic cathodic (-) stimulus, electrode distance $z = 100\ \mu m$. DR (cyan) and RS (magenta), in relation to the electrode position x (x-axis and left y-axis of the plot). Threshold current (black) in relation to the electrode position x (x-axis and right y-axis of the plot). The positions of the soma and nodes of Ranvier (N. R.) are indicated by dashed red and green lines, respectively. AIS along its entire length is represented by a gray rectangle. The positions of the dendrite, unmyelinated axon (unmyelinated) and myelinated axon are represented by black arrows, while the soma is indicated by a red dot.

The most common AP initiation sites are AIS and unmyelinated axon. For the determination of DR, the amplitudes of the stimulation currents are very close to the threshold. When stimulated outside the dendritic tree, the AP usually first occurs in the distal part of the AIS. Although dendritic spikes are possible as presented in Rattay & Wenger (2010) during dendrite stimulation (see Figure 30), if the stimulus amplitude is close to the threshold, and the electrode is placed above the middle of the

dendrite where $x = -300\ \mu m$ is stimulated, the AP first occurs either in the distal part of the AIS or in the proximal part of the unmyelinated axon, from simulation to simulation (see Figure 26). Upon stimulation of the soma, an AP occurs in the AIS, but also sometimes in the unmyelinated axon. By stimulation at the boundary between the AIS and the unmyelinated axon, the AP is initiated in the AIS, but sometimes also in the proximal part of the unmyelinated axon. When stimulating the middle of the unmyelinated axon and the second internode, the AP first appears in the central and distal (just next to the first node of Ranvier) part of the unmyelinated axon, respectively.

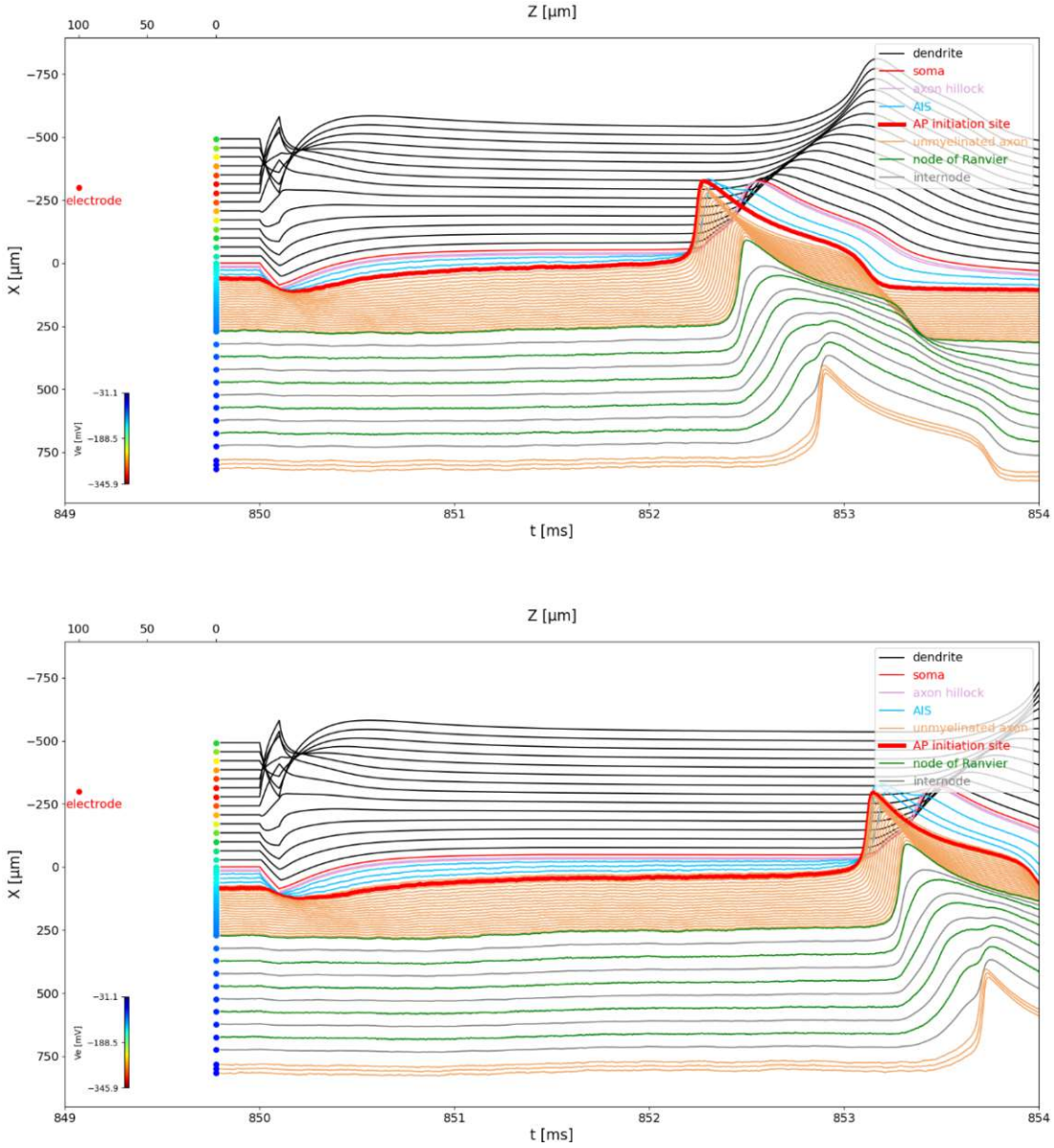

Figure 26: Different AP initiation sites with all identical parameters. *Standard 1D model*. The middle of the dendrite is stimulated by a monophasic cathodic pulse, the electrode distance is $z = 100\ \mu m$. The time axis (x-axis) and the x-position axis (y-axis) are used to represent the temporal and spatial change of the transmembrane voltage (propagation of AP), which is represented on the plot with lines of different colors.

The line of the segment where the AP was initiated is thick and red. On the left side, the centers of the segments are arranged vertically, they are represented by dots of different colors depending on the strength of the extracellular potential (color bar is in the lower left corner) caused by the electrode (red dot). For the position of the electrode and the centers of the segments, the x-axis (y-axis on the plot) and z-axis (upper x-axis) are used. (Top subfigure) AP first arises in the distal part of the AIS and spreads further from there. (Bottom subfigure) AP first occurs in the proximal part of the unmyelinated axon.

Although the nodes of Ranvier are generally quite excitable, when stimulating the third or fourth node, an interesting behavior of the transmembrane voltage can be observed (Figure 27). After stimulation above the third node, depolarization first begins in the third node, where the transmembrane voltage reaches zero the fastest (thick red line), but the maximum of the AP is reached first at the border between the distal part of the unmyelinated axon and the first node of Ranvier. Despite the fact that the isolated myelinated axon (*axon model*, Figure 24) and the myelinated axon of the *1D model* have the same electrophysiological characteristics, the DR here is significantly higher (7.668% vs. 3.934%).

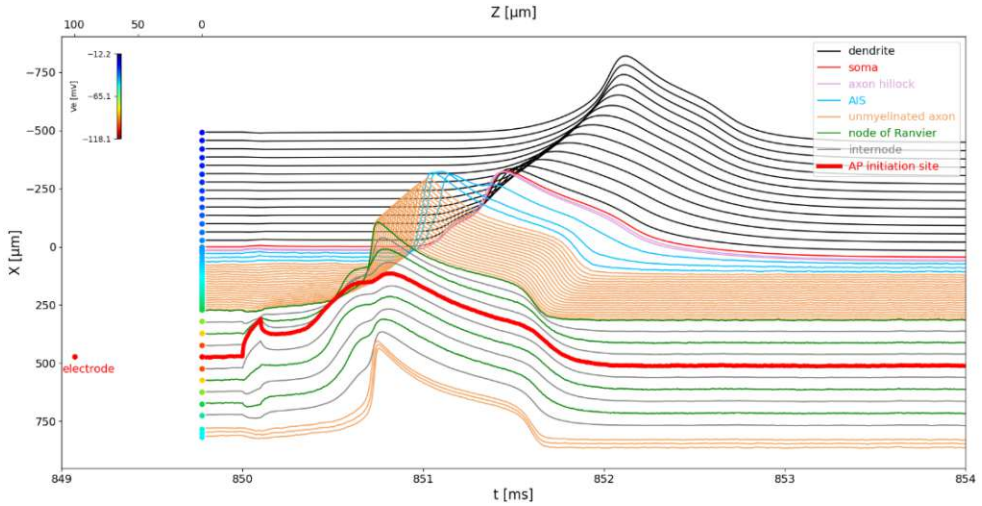

Figure 27: AP initiation site when stimulating the third node of Ranvier. *Standard 1D model*. Electrode distance $z = 100\ \mu m$. Monophasic (-) pulse. Although after stimulation the depolarization of the third node first begins and at that location the transmembrane voltage is the first to reach zero (thick red line), the maximum of AP still first occurs at the border between the distal part of the unmyelinated axon and the first node of Ranvier. Compared to the stimulation of an isolated myelinated axon (*axon model*, Figure 24), the DR here is significantly higher (7.668% vs. 3.934%) even though they have the same electrophysiological properties. Same layout as in Figure 26.

If the electrode distance is reduced from $100\ \mu m$ to $z = 50\ \mu m$, the blocking phenomenon occurs at the dendrite. That is why the points are missing for position $x = -300\ \mu m$ in Figure 28. Threshold, as expected, decreased for each position. Not counting the dendrite DR remained very similar as for the electrode distance of $100\ \mu m$ with a slight decrease in the soma and a slight increase of DR in the unmyelinated axon. During stimulation above the second node of Ranvier and above the border of the AIS and the unmyelinated axon, the DR remained almost unchanged

for the reduced electrode distance compared to stimulation where the electrode distance was $z = 100\ \mu m$.

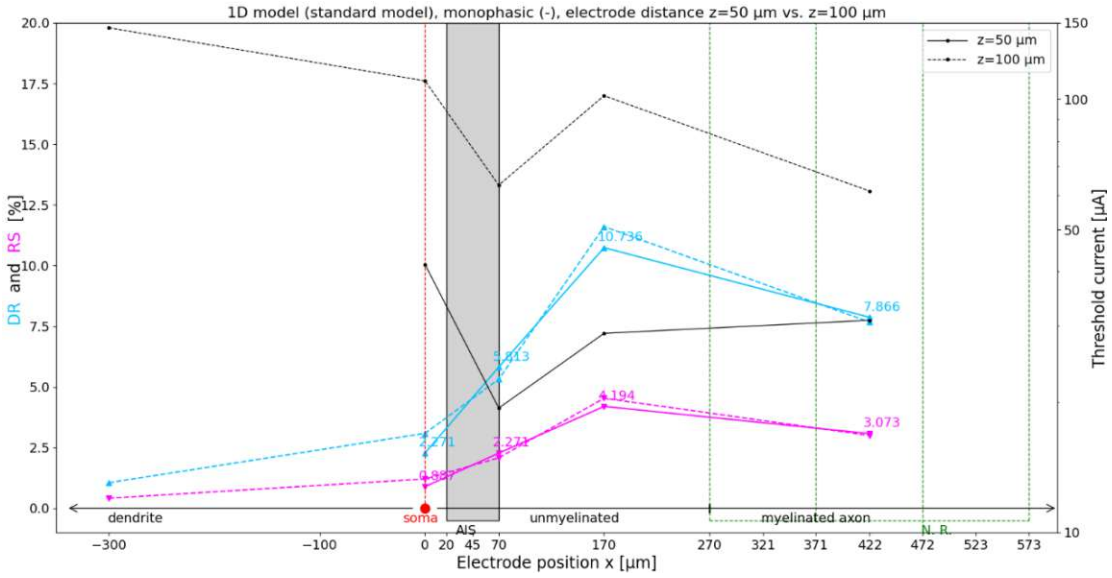

Figure 28: *Standard 1D model*. Monophasic cathodic (-) stimulus, electrode distance $z = 50\ \mu m$ vs. $z = 100\ \mu m$. The blocking phenomenon is present at the position $x = -300\ \mu m$ for the electrode distance $z = 50\ \mu m$, which is why the points at that position are missing. Same layout as in Figure 25.

In following sections, various variations of the *standard 1D model* were presented, in which the diameter of the dendrite and the maximum conductances of the active channels in the AIS were varied. The cell is stimulated extracellularly (monophasically and biphasically) at different electrode distances, but also intracellularly.

6.3.1 Dendrite Diameter Variation

In this section, the change in DR of the standard 1D model is observed if the dendrite diameter is reduced four times, from 5 µm to 1.25 µm (Figure 29). The electrode distance is constant and is $z = 100$ µm. The dendrite ($x = -300$ µm), the soma ($x = 0$ µm), the border of the AIS and unmyelinated axon ($x = 70$ µm) and the middle of the unmyelinated axon ($x = 170$ µm) were stimulated.

In comparison with the standard model, the stimulation threshold increases as the dendrite diameter decreases, especially on the dendrite and soma (note that the threshold current axis is logarithmic). By far the highest threshold value is present on the soma. Moving away from the dendrite, in the case of the unmyelinated axon, the thresholds almost coincide. As dendrite diameter decreased, DR increased. The greatest increase in DR is also visible at the soma, and then at the border between AIS

and unmyelinated axon. A slight increase in DR is present in the dendrite and unmyelinated axon.

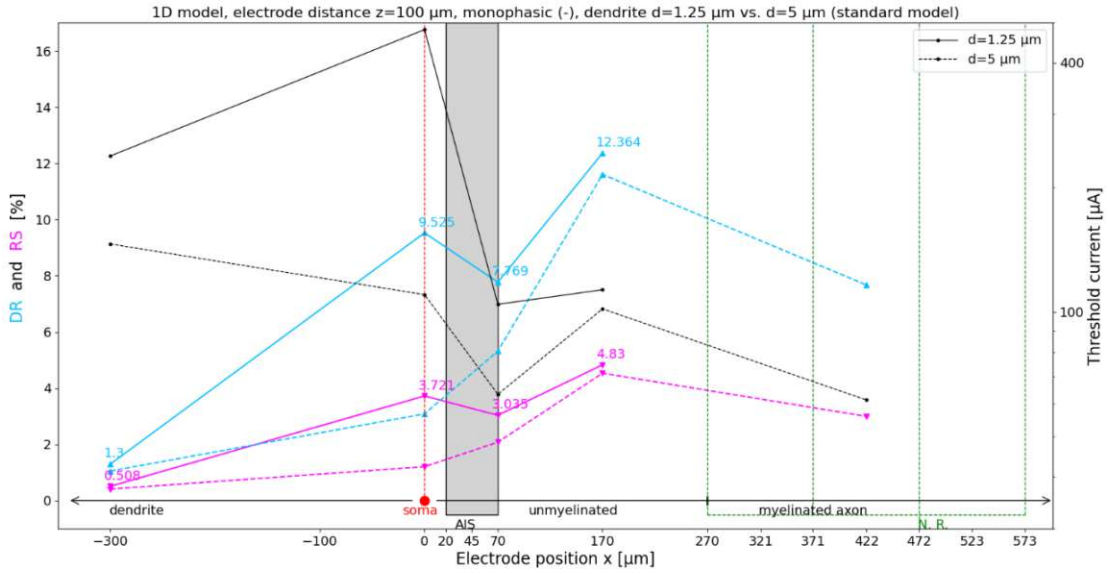

Figure 29: *Standard 1D model* with dendrite diameter of 5 μm (dashed lines) vs. 1.25 μm (solid lines). Monophasic cathodic (-) stimulus, electrode distance $z = 100\ \mu m$. With the decrease in dendrite diameter, DR increased the most at the soma, then at the AIS. Same layout as in Figure 25.

When stimulating a reduced dendrite with a diameter of $d = 1.25\ \mu m$ with pulses of amplitude near the threshold, there are dendritic spikes (see Figure 30), unlike the dendrite with a diameter of $d = 5\ \mu m$ presented in Figure 26, where the AP is initiated either in the distal part of the AIS or in the proximal part of the unmyelinated axon. When simulating soma, unlike the standard model, AP is initiated only in the AIS.

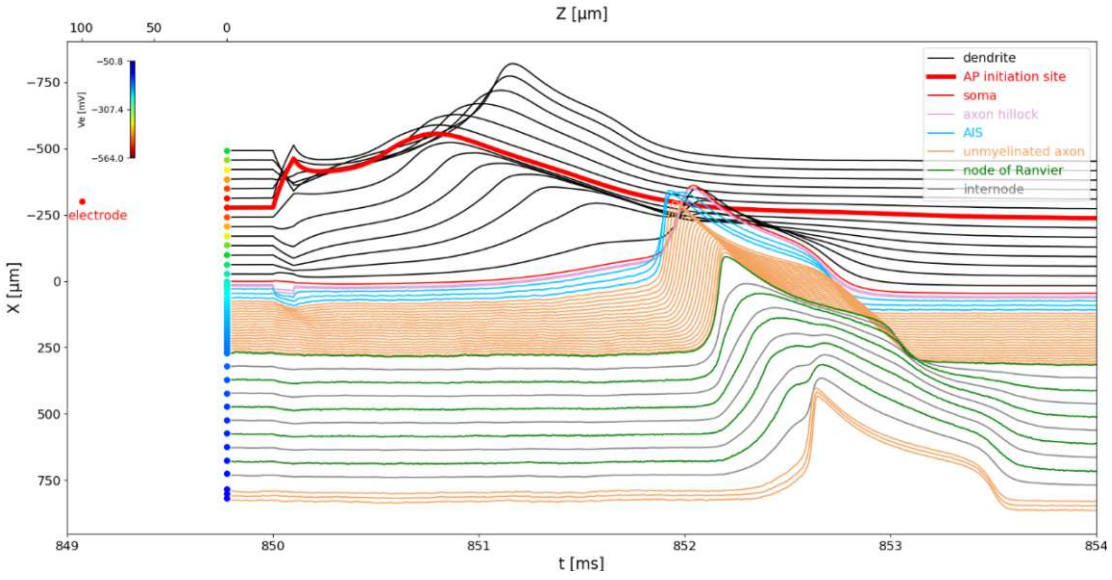

Figure 30: Stimulation of the dendrite with a reduced diameter to $d = 1.25\ \mu m$ with a pulse near the threshold results in dendritic spike (thick red line). Compare with Figure 26, where upon stimulation of the

dendrite of original diameter $d = 5\ \mu m$, AP is initiated in either the distal AIS or the proximal part of the unmyelinated axon. Same layout as in Figure 26.

6.3.2 Doubled Maximal Conductances of Active Channels in AIS

In this section, the DR and threshold of the *standard 1D model* with doubled maximum conductances of active channels in AIS are compared with the original model. The geometric and the electrophysiological properties of the entire model, excluding AIS, remained unchanged compared to the original model. Changed values of maximum conductances of the new model are $g_{Na1.2} = 200\ mS/cm^2$, $g_{Na1.6} = 640\ mS/cm^2$ and $g_{Kv} = 200\ mS/cm^2$ (compare with the values from Table 9).

The cell was stimulated at a constant electrode distance $z = 100\ \mu m$, at the locations $x = -300\ \mu m$, $x = 0$, $x = 70\ \mu m$, $x = 170\ \mu m$ and $x = 422\ \mu m$. Threshold slightly decreased at the soma ($x = 0$) and at the border of AIS and unmyelinated axon ($x = 70\ \mu m$), while it remained almost the same at other positions. DR increased everywhere, the most at the unmyelinated axon ($x = 170\ \mu m$), then at the soma ($x = 0$). The smallest increase in DR was recorded at the dendrite ($x = -300\ \mu m$). See Figure 31 for a better understanding of the data.

The amplitude of the threshold current decreased slightly at the soma and at the border of AIS and unmyelinated axon, while it remained almost the same at other positions. DR increased slightly everywhere, while it was the highest at the unmyelinated axon and soma (Figure 31).

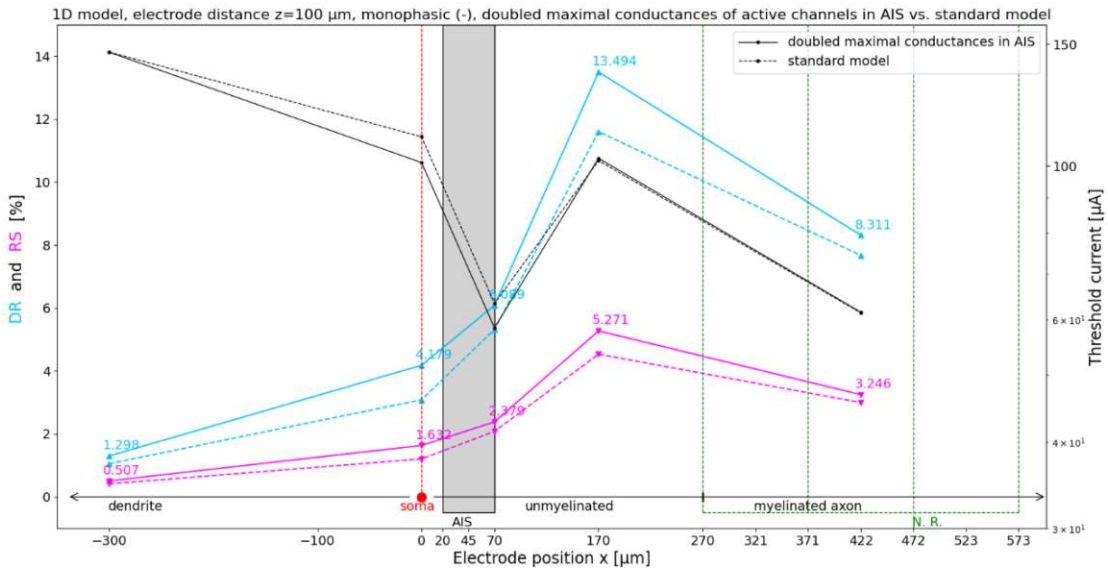

Figure 31: *Standard 1D model* (dashed lines) vs. model with doubled maximum conductances of active channels in AIS (solid lines). Monophasic cathodic (-) stimulus, electrode distance $z = 100\ \mu m$. Compared to the standard model, the DR increased slightly everywhere, the most at the unmyelinated axon and at the soma. Same layout as in Figure 25.

The AP initiation site in the model with doubled maximum conductances of active channels in the AIS upon stimulation at the boundary between the AIS and unmyelinated axon ($x = 70\ \mu m$) is in the distal part of the AIS, unlike the *standard 1D model* where AP first occurs in the proximal part of the unmyelinated axon.

6.3.3 Monophasic (-) vs. Biphasic (+/-) Extracellular Stimulation

In this section, the geometrical and electrophysiological properties of the *standard 1D model* were not changed, but the behavior of DR and threshold is compared in relation to whether the cell is stimulated monophasically with cathodic (-) stimulus, or biphasically with anodic followed by cathodic (+/-) stimulus. In both cases, it is an extracellular stimulation.

The positions on the x-axis where the electrode was placed are above the dendrite ($x = -300\ \mu m$), above the soma ($x = 0\ \mu m$), above the border of the AIS and unmyelinated axon ($x = 70\ \mu m$), above the unmyelinated axon ($x = 170\ \mu m$) and above the second internode ($x = 422\ \mu m$). The position of the electrode in the z-axis was constant all the time and was $z = 100\ \mu m$ (Figure 32).

The following can be seen from Figure 32. Stimulus threshold is consistently higher for biphasic (+/-) than for monophasic (-) stimulus. By far the largest difference between the threshold of monophasic and biphasic stimuli is at the soma, while the smallest is at the second internode. A different trend can be seen for DR. DR is almost the same for both monophasic and biphasic stimulation at the dendrite and at the second internode (at the dendrite for a biphasic stimulus the DR is slightly higher, and at the second internode DR is slightly lower). Compared to the monophasic stimulus, with the biphasic stimulus, the DR at the soma, at the border of the AIS and unmyelinated axon and at the unmyelinated axon is lower, while the difference is by far the biggest at the unmyelinated axon.

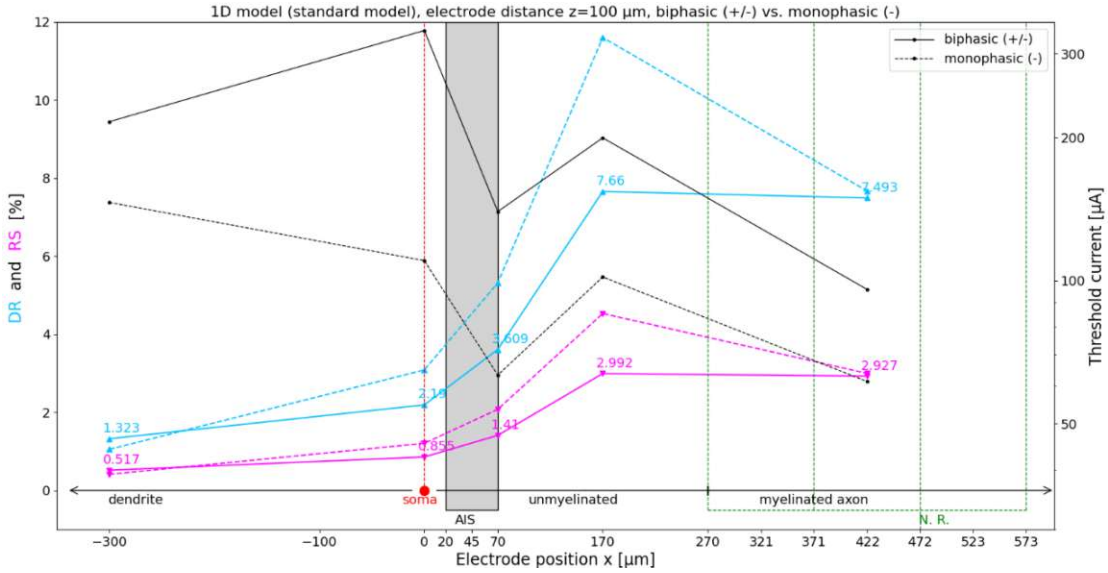

Figure 32: *Standard 1D model*, monophasic (-) stimulation (dashed lines) vs. biphasic (+/-) stimulation (solid lines). Electrode distance $z = 100\ \mu m$. With biphasic (+/-) stimulation, DR decreased at the soma and AIS, and especially at the unmyelinated axon. Same layout as in Figure 25.

It was observed that the site of AP initiation during stimulation of an unmyelinated axon ($x = 170\ \mu m$) for a biphasic stimulus is the distal part of the unmyelinated axon on the border with the first node (the greatest depolarization is in the second node of Ranvier), while for a monophasic stimulus it is the central part of the unmyelinated axon when electrode distance $z = 100\ \mu m$. By reducing the distance of the electrode to $z = 50\ \mu m$, the place of AP initiation becomes, as with the monophasic stimulus, the central part of the unmyelinated axon. When the AIS is stimulated, AP initiation occurs exclusively in the proximal or middle part of the AIS.

If the electrode distance is reduced from $100\ \mu m$ to $z = 50\ \mu m$, a blocking phenomenon occurs at the dendrite, so that the points for threshold, DR and RS are missing in Figure 33, which shows the influence of biphasic (+/-) stimulation of *standard 1D model* if the distance is reduced from $100\ \mu m$ to $50\ \mu m$. With reduced electrode distance, the threshold is, as expected, consistently much lower. In contrast to that, DR increased when stimulating the unmyelinated axon and at the border of the AIS and unmyelinated axon, while it slightly decreased at the second node of Ranvier and at the soma.

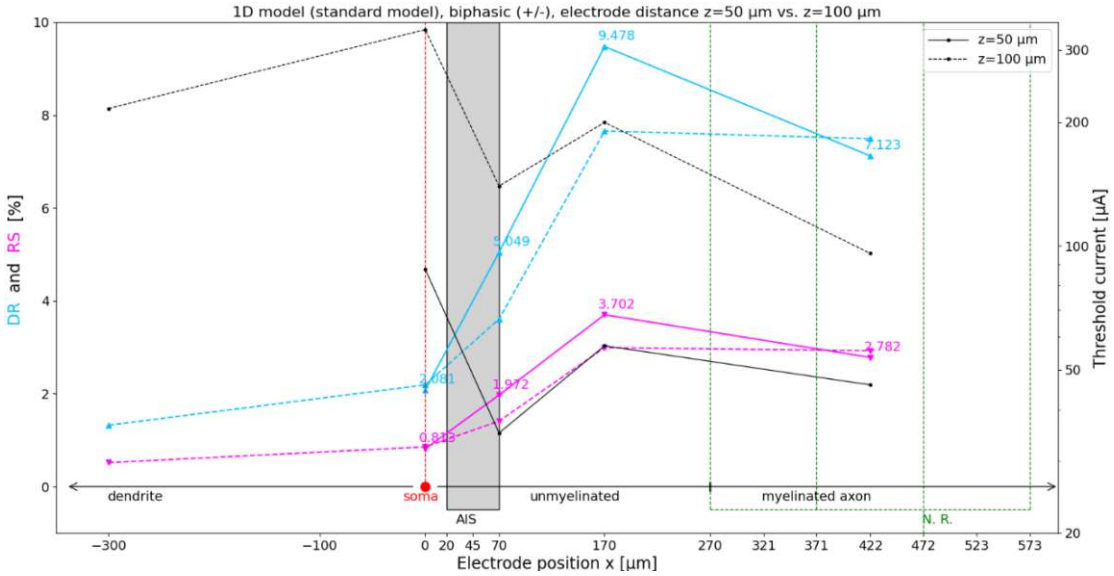

Figure 33: *Standard 1D model*, biphasic (+/-) stimulation, electrode distance $z = 100$ µm (dashed lines) vs. $z = 50$ µm (solid lines). Due to the blocking phenomenon, the points at $x = -300$ μm are missing for the electrode distance $z = 50$ μm. When the electrode distance decreased, the DR increased at the AIS and at the unmyelinated axon. Same layout as in Figure 25.

6.3.4 Intracellular vs. Extracellular Stimulation

In this section, DR is compared during intracellular anodic (+) stimulation with extracellular cathodic (-) stimulation at two electrode distances, 50 µm and 100 µm.

The x-axis positions for extracellular stimulation are -300 µm, 0 µm, 70 µm, 170 µm and 422 µm for electrode distance $z = 100$ µm. For the electrode distance $z = 50$ μm, the points for the position $x = -300$ μm are missing due to the blocking phenomenon. Intracellular stimulation is performed in the middle of the corresponding sections that are stimulated. At the dendrite it is $x = -260$ μm, at the soma $x = 0$ μm, at the AIS $x = 45$ μm, at the unmyelinated axon it is $x = 170$ μm and at the second internode it is $x = 422$ μm.

The results of the simulations are presented in Figure 34. Thresholds, as expected, decrease with decreasing electrode distance and are the smallest with intracellular stimulation. In soma, DR is the largest for intracellular stimulation, followed by $z = 100$ μm, and finally $z = 50$ μm. Similar behavior can be seen when stimulating the middle of the unmyelinated axon. When stimulating the second internode, the DR for intracellular stimulation is lower than the DR for $z = 50$ μm and $z = 100$ μm. By far the biggest differences can be seen when stimulating the middle of the dendrite. DR during intracellular stimulation of the dendrite is about five times higher than for the electrode distance $z = 100$ μm, and it is even higher than DR during intracellular stimulation of soma and AIS.

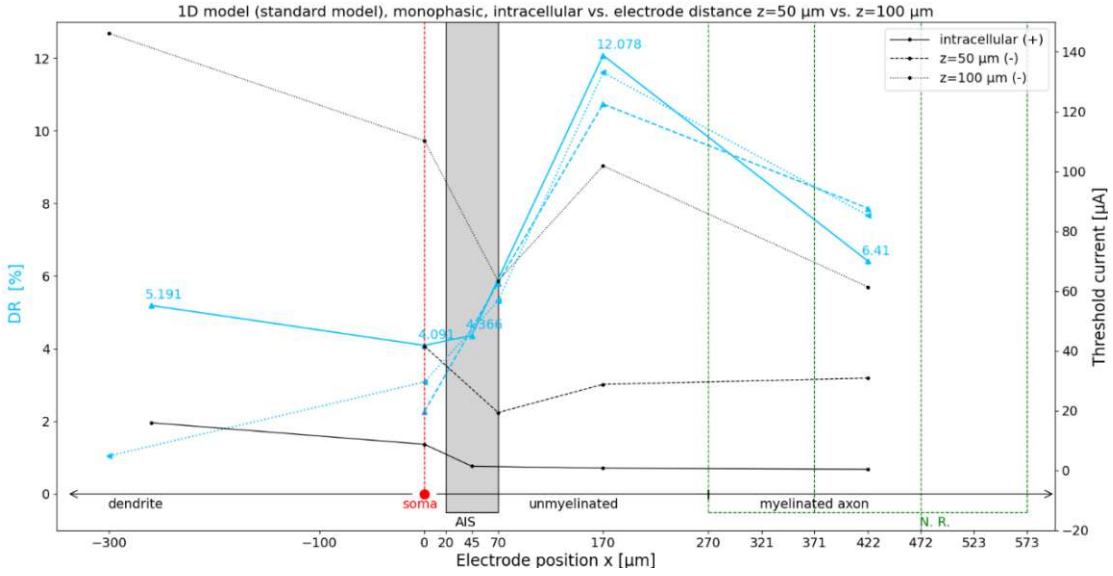

Figure 34: *Standard 1D model,* monophasic (+) intracellular stimulation (solid lines) vs. monophasic (-) extracellular stimulation for electrode distances of 50 μm (dashed lines) and 100 μm (dotted lines). Due to the blocking phenomenon, the points at $x = -300\ \mu m$ are missing for the electrode distance $z = 50\ \mu m$. DR for intracellular stimulation of the dendrite is much higher than for the distance $z = 100\ \mu m$. Same layout as in Figure 25.

6.4 Extended 1D Model

In this section, DR was examined on the *extended 1D model* which has additional active channels and mechanisms in the soma and dendrite. Stimulations were performed at different electrode distances, $z = 100\,\mu m$ and $z = 50\,\mu m$ for extracellular monophasic and biphasic stimulation, but also intracellularly. The DR is mainly compared to the DR of an equivalent simulation experiment with a *standard 1D model*. As with the *standard 1D model*, changes in transmembrane voltage, and therefore action potentials which are responsible for spiking efficiency and DR, are detected in the distal unmyelinated axon.

During monophasic stimulation with a cathodic (-) train of pulses for an electrode distance of $z = 100\ \mu m$ (Figure 35), the threshold almost perfectly coincides with the threshold of the *standard 1D model*. The DR also closely matches the DR of the standard model, with the exception of the unmyelinated axon where the DR is smaller than in the standard model.

Unlike the standard model, where when stimulating an unmyelinated axon for an electrode distance of $z = 100\,\mu m$, the AP is initiated in the middle of the unmyelinated axon, in the extended model, the AP is initiated in the middle of the AIS.

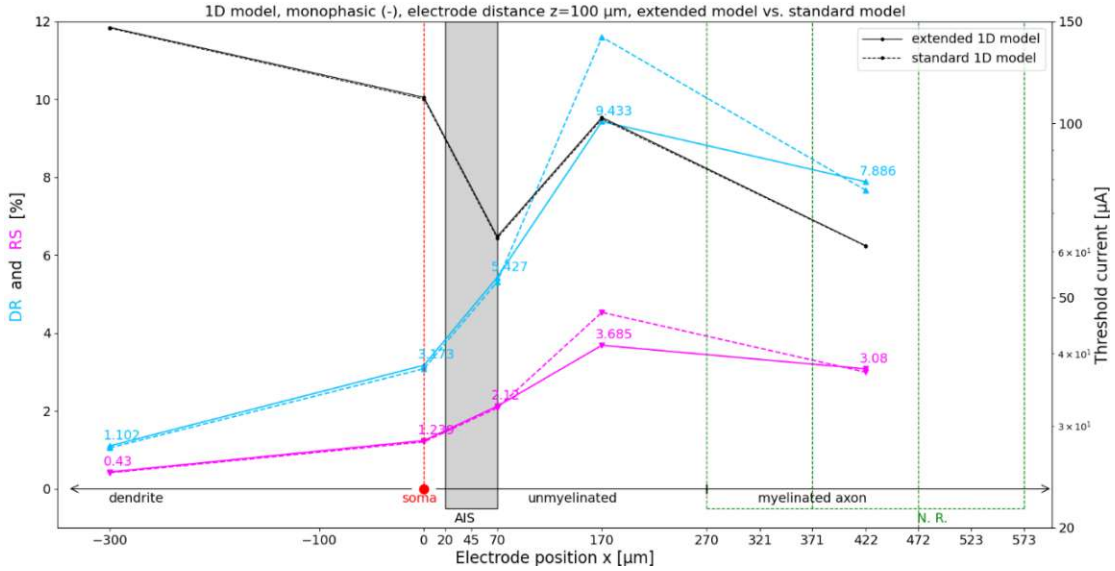

Figure 35: *Extended 1D model* (solid lines) vs. *Standard 1D model* (dashed lines). Monophasic (-) extracellular stimulation for electrode distance $z = 100\ \mu m$. DR of the extended model decreased at unmyelinated axon. Same layout as in Figure 25.

When the electrode distance is reduced from $100\ \mu m$ to $z = 50\ \mu m$, the extended model behaves even more similar to the standard model (Figure 36). Thresholds at a reduced distance are almost the same as in the standard model. DR is also very similar with a very slight increase at the unmyelinated axon and a very slight decrease at the second internode.

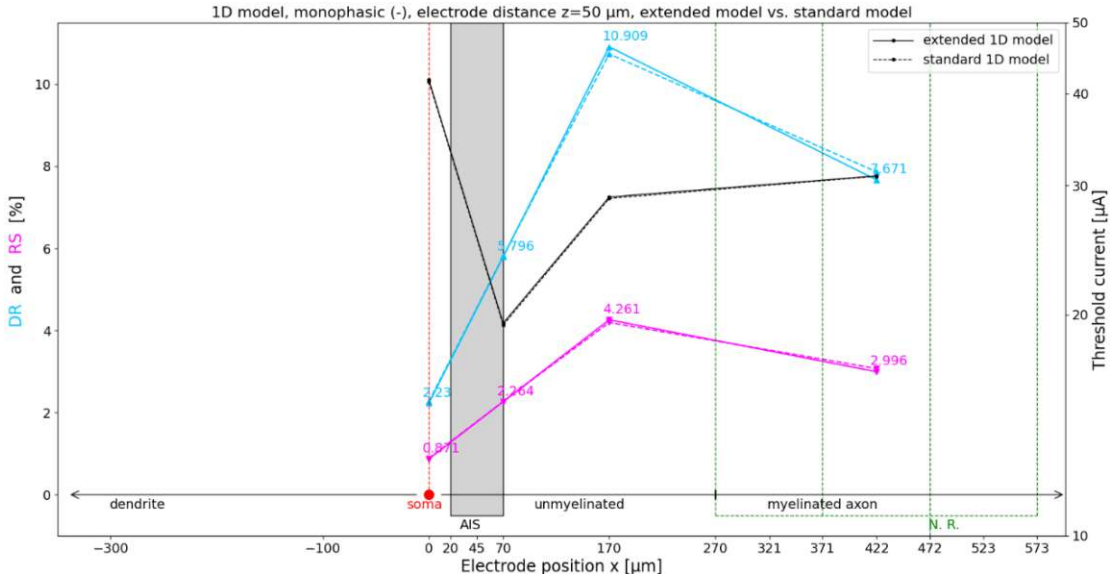

Figure 36: *Extended 1D model* (solid lines) vs. *Standard 1D model* (dashed lines). Monophasic (-) extracellular stimulation for electrode distance $z = 50\ \mu m$. DR of the extended model is nearly the same as that of the standard model. Same layout as in Figure 25.

Biphasic (+/-) stimulation of the extended model also gives almost the same thresholds as biphasic stimulation of the standard model (Figure 37). The same could be said for

DR in the area from the dendrite to the unmyelinated axon. At the unmyelinated axon and at the second internode, the DR of the extended model decreased compared to the DR of the standard model.

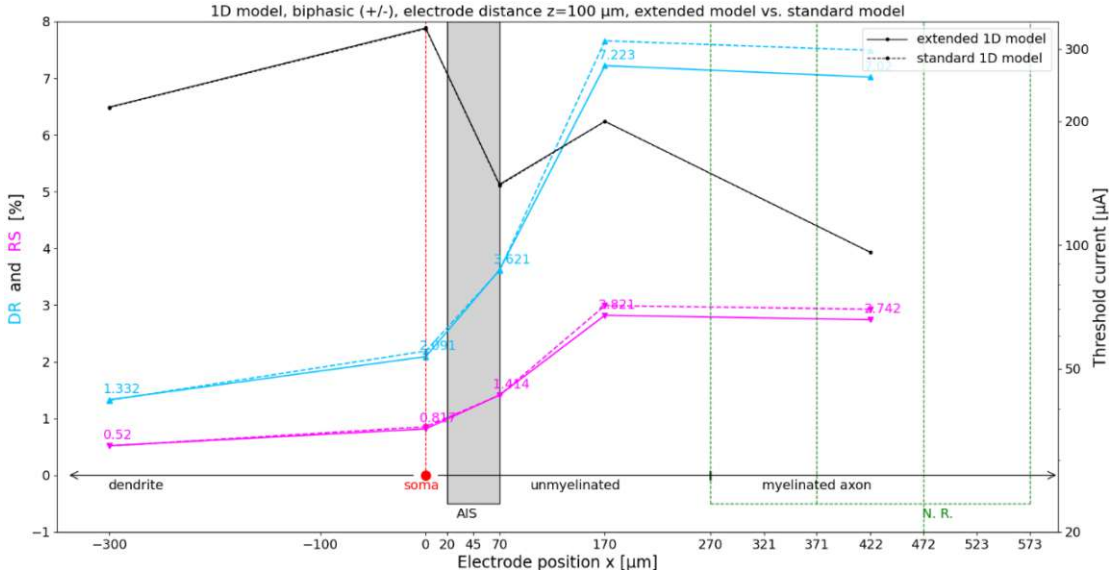

Figure 37: *Extended 1D model* (solid lines) vs. *Standard 1D model* (dashed lines). Biphasic (+/-) extracellular stimulation for electrode distance $z = 100\ \mu m$. DR of the extended model decreased at the unmyelinated axon and at the second internode compared to the standard model. Same layout as in Figure 25.

.

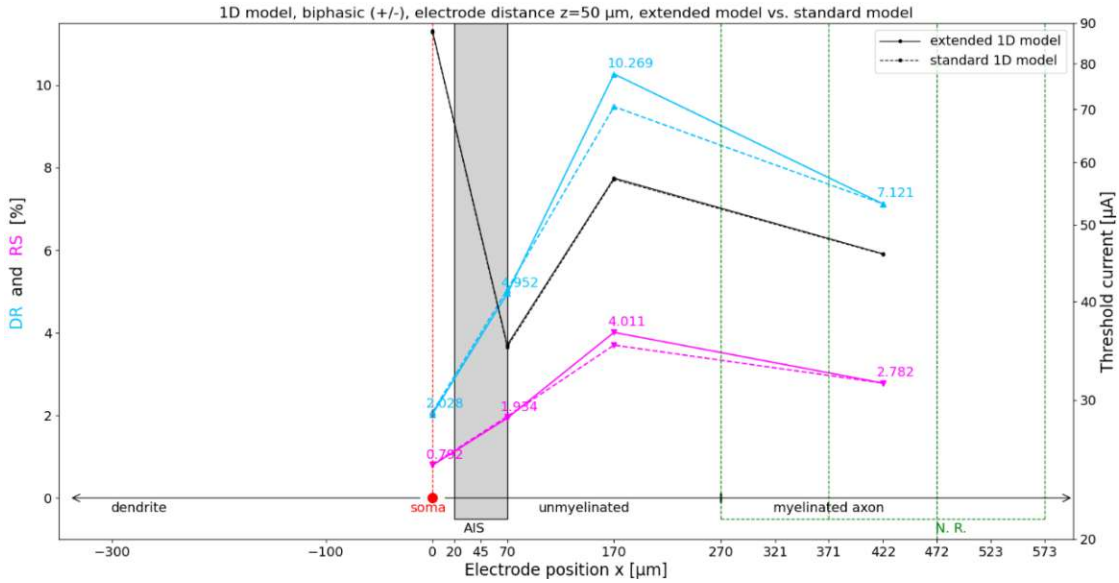

Figure 38: *Extended 1D model* (solid lines) vs. *Standard 1D model* (dashed lines). Biphasic (+/-) extracellular stimulation for electrode distance $z = 50\ \mu m$. DR of the extended model increased at the unmyelinated axon compared to the standard model. Same layout as in Figure 25.

If the electrode distance is reduced from $100\ \mu m$ to $z = 50\ \mu m$, and the cell is stimulated with a biphasic (+/-) train of pulses (Figure 38), the blocking phenomenon occurs in the dendrite of both the extended model and the standard model. The

thresholds of both models overlap. DR at the soma, at the border of the AIS and unmyelinated axon and at the second internode has very similar values as the DR of the standard model at the same positions. The DR of the extended model increased compared to the DR of the standard model when stimulating an unmyelinated axon.

Intracellular anodic (+) stimulation, as well as other types of stimulation of the extended model, give almost the same thresholds as intracellular stimulation of the standard model. In Figure 39, three different forms of monophasic stimulation of the extended model are compared. Intracellular anodic stimulation was compared with extracellular cathodic (-) stimulation for two electrode distances, 50 µm and 100 µm. All thresholds match the thresholds of the standard model. The DR of the extended model has a similar form as the DR of the standard model for the equivalent simulation experiment. The biggest difference is seen in the DR during intracellular stimulation of the second internode, where the DR of the extended model is greater than that of the standard model.

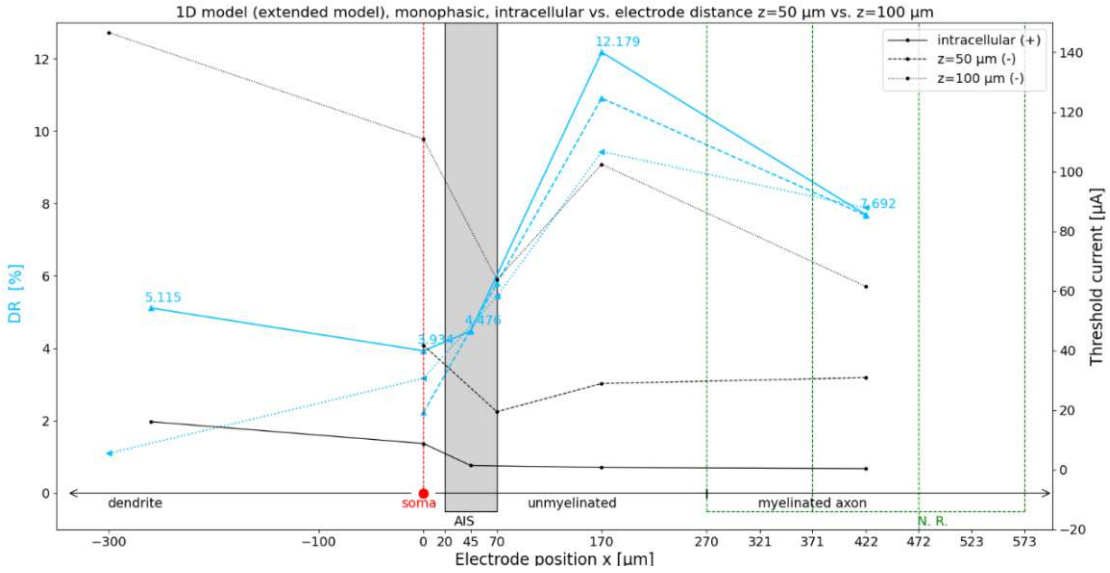

Figure 39: *Extended 1D model,* monophasic (+) intracellular stimulation (solid lines) vs. monophasic (-) extracellular stimulation for electrode distances of 50 μm (dashed lines) and 100 μm (dotted lines). DR from the extended model for all three types of stimulation has a similar trend as DR from the standard model (compare with Figure 34). DR for intracellular stimulation behaves similarly to the standard model, except that it is larger at the second internode. Same layout as in Figure 25.

6.5 Increased Standard Deviation of the Noise in the Soma of the *1D model*

In this section, the change in DR during soma stimulation is examined if the standard deviation of the noise in the soma is increased 4 times, from $\sigma = 1$ to $\sigma = 4$. The

reason for this are the methods from a recent study (Madugula, et al., 2022) in which noise was modeled in such a way that a larger noise was injected into the soma than into the rest of the cell in order to increase DR during soma stimulation. Their simulation experiments were performed on the retinal ganglion cell (RGC), and the goal here is to see how it would be reflected on the pyramidal cell.

Different types of stimulation and two models are used for this purpose (Figure 40). The *standard 1D model* is stimulated extracellularly monophasically (-) and biphasically (+/-), where the distance of the electrode from the soma is $z = 100\ \mu m$. The soma of the standard model is also stimulated intracellularly monophasically (+). The second model is the *extended 1D model* and its soma is stimulated intracellularly monophasically (+).

DR increased from case to case between 7% and 18% with an average of about 12.5%.

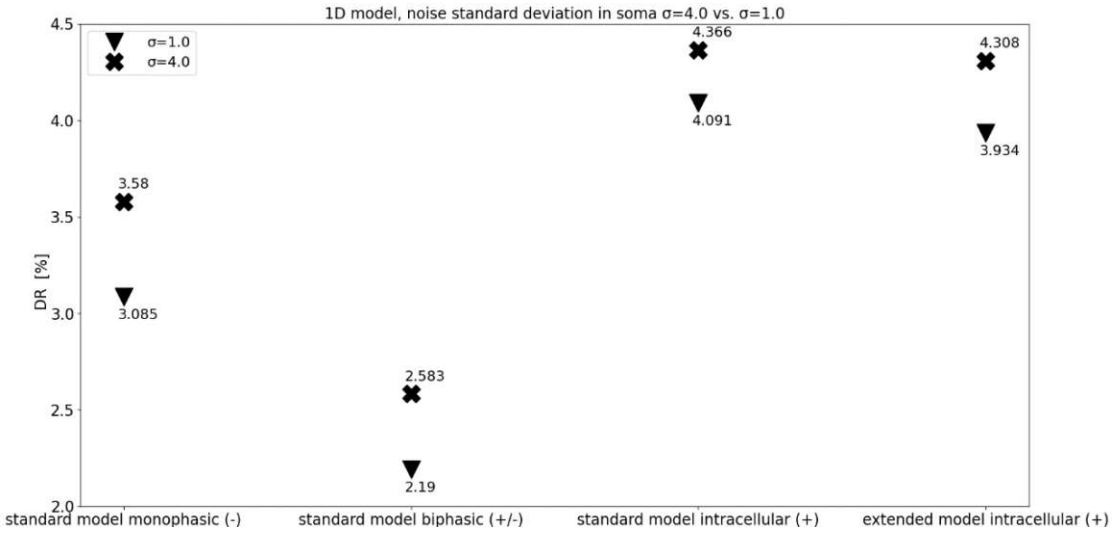

Figure 40: Comparison of DR during stimulation of the soma if the noise standard deviation in the soma is $\sigma = 1$ (marked by inverted triangles) vs. 4 times the standard deviation $\sigma = 4$ (marked by black x). From left to right: three times standard model, monophasic (-), then biphasic (+/-) stimulation at electrode distance electrode distances $z = 100\ \mu m$, then intracellular monophasic (+) stimulation, far right is intracellular monophasic (+) stimulation of the extended model. The average increase in DR if the noise standard deviation is increased from 1 to 4 is about 12.5%.

6.6 DR at the Upper Threshold of the *Standard 1D Model*

As mentioned in section 3, spiking efficiency decreases due to the blocking phenomenon (see section 2.2.2) as the stimulus approaches the upper threshold, and if the stimulus is strong enough, spiking efficiency becomes 0. That is why it is possible to examine DR for upper threshold stimulations.

The cell was stimulated monophasically (-) at positions $x = -300\ \mu m$, $x = 0\ \mu m$, $x = 70\ \mu m$, $x = 170\ \mu m$ and $x = 422\ \mu m$, with the electrode distance $d = 100\ \mu m$. The obtained DRs and thresholds were compared with their equivalents for lower threshold stimulation (Figure 41).

The upper threshold is everywhere more than 20 times higher than the lower threshold, except at $x = -300\ \mu m$ at the dendrite, where the upper threshold is approximately twice as high as the lower threshold. The biggest difference between upper and lower threshold is at the border between AIS and unmyelinated axon where $x = 70\ \mu m$ and at the soma where $x = 0\ \mu m$, where the upper threshold is about 80 and 60 times higher than the lower threshold, respectively. DR significantly decreased at the dendrite, soma and unmyelinated axon, while it increased at the second internode.

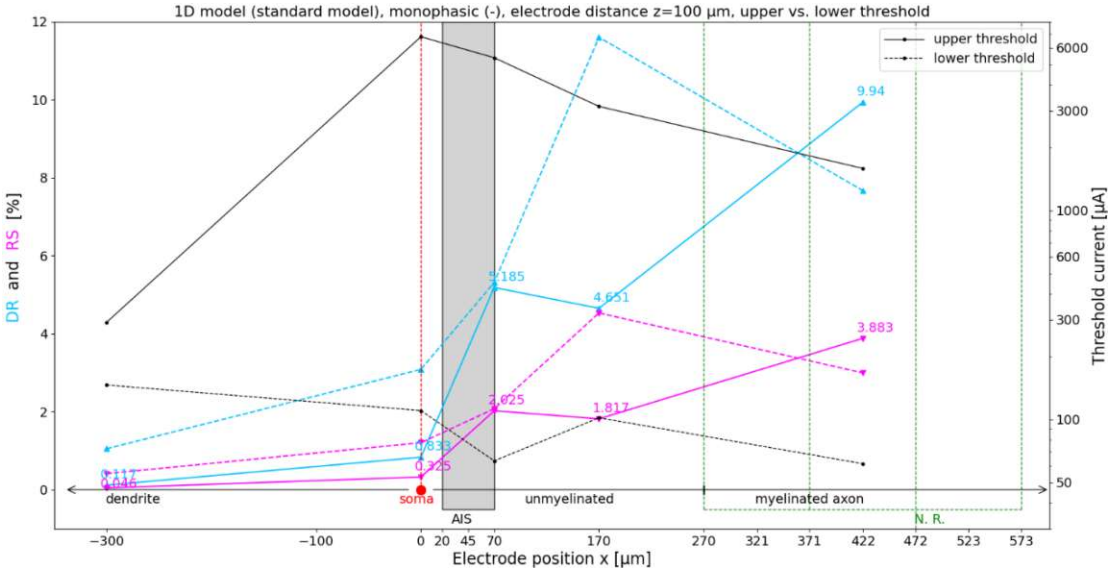

Figure 41: *Standard 1D model* upper threshold (solid lines) vs. lower threshold (dashed lines) stimulation. Monophasic (-) extracellular stimulation for electrode distance $z = 100\ \mu m$. DR decreased at the dendrite, soma and unmyelinated axon, while it increased at the second internode. Same layout as in Figure 25.

7 Discussion

In this section the results presented in previous section are discussed together with model limitations and possible suggestions for further investigations.

As expected, the thresholds are the lowest when stimulating AIS and nodes of Ranvier, which coincides with the simulation experiments of Rattay & Wenger (2010), Rattay, et al. (2012) and Werginz, et al. (2020) and with the experiments from Gustafsson & Jankowska (1976).

There are several possible factors that could influence DR variations in relation to different positions and configurations of the stimulation electrode. The most obvious one is the maximum sodium conductance ($g_{Na} = g_{Na1.2} + g_{Na1.6}$) of the corresponding stimulated section (with the increase in the maximum sodium conductance, the noise also increases, and therefore the DR). When stimulating a very responsive section (with a large g_{Na}, such as AIS), it seems that there is a rivalry between responsiveness and noisiness, which can reduce DR. Also, the stimulated area of the cell, which can be determined through the activating function, appears to have an impact on DR. Another thing that could affect the DR is the geometry of the model (diameter and length of the fiber). As the diameter of the fiber decreases, the DR increases, but so does its axial resistance (Yi, et al., 2017) and the fiber becomes harder to stimulate (Rattay, et al., 2017). The origin of AP initiation could also contribute to the magnitude of DR.

The reasons for the lowest DR observed during extracellular stimulation of the dendrite could be its low g_{Na} and large diameter. Interestingly, although the soma and dendrite have the same electrophysiological properties and the soma has a much larger diameter, stimulation above the soma increases the DR (Figure 25). A possible explanation for this might be that the soma is closer to more excitable segments such as the AIS, which, taking into account the activating function, are also stimulated. Therefore, with the reduction of the distance of the electrode from the soma, the DR also decreases because a smaller part of the more excitable segments is stimulated (Figure 28), and a similar behavior can be seen in the unmyelinated axon as well. Although AIS has the highest g_{Na}, its stimulation does not result in the highest DR, and the reason may be its great responsiveness. A better ratio of responsiveness to noisiness in favor of DR may be responsible for relatively high DR in the unmyelinated axon, with its peak at the first node of Ranvier. The reason for the reduction of DR when the myelinated axon is stimulated could be the low average g_{Na} of the stimulated

part of the axon and the fact that noise is not modeled in the myelinated internodes. In favor of the theory that the origin of AP initiation can influence the DR is that when stimulating the middle node of the *axon model* (Figure 24) and the third node of the *1D model* (Figure 27), the DR of the latter is almost twice as large, even though they have the same electrophysiological properties. The third node of the *1D model* is far enough from the parts of the cell with properties different from those of the node-internode sequence which, taking into account the activating function, are not directly stimulated. The difference is that in the *axon model* AP initiation occurs in the node itself, while in the *1D model* AP initiates at the border of the distal part of the unmyelinated axon with the first node of Ranvier.

With a decrease in the diameter of the dendrite, an increase in DR is expected, which is not the case here (Figure 29), and the reason for this could be that the origin of AP initiation is in the dendrite, and not in the AIS. The reason for the increase in DR in the soma may be a stronger stimulus threshold required for AP initiation, which also affects the more excitable parts of the cell.

Doubling g_{Na} in the AIS led to a slight increase in DR in the surrounding parts of the cell, while when stimulating the AIS itself, the increase in DR is a bit smaller, and the rivalry between responsiveness and noise may be the reason for that.

With biphasic (+/-) extracellular stimulation, DR is generally smaller than with monophasic (-). Although DR in μA (non-normalized to threshold) is generally higher than with monophasic stimulation, possibly because the anodic phase of the pulse depolarizes a larger part of the cell (see Figure 10b), due to the higher stimulation threshold, normalization reduces DR. The greatest reduction of DR is when simulating the unmyelinated axon, and the possible reason for this may be the fact that the anodic phase of the pulse depolarizes the beginning of the myelinated axon the most (especially the second internode) and the AP is initiated at the border of the unmyelinated axon and the first node.

Intracellular stimulation of the dendrite, although it has the highest threshold, gives a higher DR than stimulation of the soma and AIS. A possible explanation is that the stimulated part of the dendrite has a relatively low responsiveness and is far from highly responsive segments.

Additional ion channels and mechanisms in the *extended 1D model* give almost the same thresholds as the standard model. It seems that these channels do not affect the threshold, partly because of low conductances (Rattay & Wenger, 2010), and partly because these channels influence the amplification of AP after depolarization (and cause the generation of spike bursts), which has no effect when determining the

threshold (Royeck, et al., 2008). Not so pronounced changes in the DR, depending on the distance and configuration of the stimulation electrode, compared to the standard model can be seen when stimulating an unmyelinated or myelinated axon. When stimulating other parts of the cell, the DR almost does not change at all compared to the standard model, which is especially interesting for the dendrite and soma because additional channels and mechanisms are only present there. It can therefore be assumed that K_m, K_{Ca} and Ca_v channels in the soma and dendrite and the Ca_{cm} mechanism found in the soma have very low impact on DR in general.

As reported in Madugula, et al. (2022), DR in retinal ganglion cells (RGCs) should be the highest in the soma and thus noise injected into soma compartments should be higher than in the rest of the modeled cell. Although similarities between RGCs and PCs regarding axon length, soma size and AIS properties were reported in Rattay, et al. (2017), after increasing noise current in the soma, as suggested in Madugula, et al. (2022), a *1D model* of PC in this thesis shows no significant change in DR value observed at soma. The different response of the PC to increased noise current injected in the soma may be due to the fact that the maximum sodium conductance in the soma in PC is much lower compared to that in RGC.

The upper thresholds during extracellular monophasic (-) stimulation are, not counting the dendrite, even 25 to 60 times higher than the lower thresholds which is in accordance with values reported for PC (Sajedi, et al., 2021). The change in transmembrane voltage was measured at the distal part of the axon (furthest from the soma). As expected, the values of DR normalized to threshold along the entire cell are lower than for the lower threshold (except at the second internode where DR is slightly higher than for the lower threshold) since upper thresholds are much higher than lower thresholds. In contrast to that, DR values not normalized to threshold (in μA) are significantly higher than at the lower threshold, except for the dendrite. To explain such behavior further studies are needed. The reason for the lower DR in the dendrite may be the dendritic spike and the fact that the dendrite is farthest from the highly responsive segments (with high g_{Na} values) than any other section, so responsive segments, considering the activating function, are not directly stimulated.

Due to some similarities between the PC model in this thesis and the RGC model from Dizdar (2022) where DR was also examined, a similar behavior of DR in relation to the threshold was observed, namely their somewhat inverse relationship. This behavior is most striking in the part of the cell from the dendrite to the AIS. Distal from the AIS, there is a noticeable greater deviation from this behavior in the case of the PC than in the case of the RGC, and the reason may be the different structure of the PC's axon, which contains nodes of Ranvier and myelinated internodes.

There are several limitations of the *1D model* such as its simplified geometry and the lack of more recently developed ion channels and mechanisms. For further work it is suggested to use more complex 3D morphologies like in Mainen & Sejnowski (1996) and Almog & Korngreen (2014) and more recent mechanisms as in Keren, et al. (2005), Keren, et al. (2009) and Almog & Korngreen (2014).

Neurons in an intact brain are as a consequence of network activity constantly affected by synaptic background noise, which leads to an increase in membrane conductance and noisy fluctuations of the transmembrane voltage (Destexhe & Paré, 1999; Destexhe, et al., 2003). Many modeling studies and experiments where spiking efficiency is considered do not take into account this background noise, which according to Fellous, et al. (2003) and Khubieh, et al. (2016) affects the DR, i.e., increases it compared to the DR of an isolated cell. Background noise should also be kept in mind in future research, because in the living intact brain, the nerve cells are not isolated and there is an influence of network activity.

In general, there is a lack of modeling and experimental studies considering spiking efficiency and DR of PCs. This is one of the reasons why it is difficult to explain or find causes for some of the obtained results. Therefore, all the examined points in this thesis should be investigated more deeply and confirmed with new experimental studies.

8 Appendix Model Parameters

Electrophysiological properties							
Property [unit]	Dend	Soma	AH	AIS	Unmy	Node	Intern
$g_{pas}\ [mS/cm^2]$	0.033	0.033	0.033	0.033	0.033	0.033	1/17
$C_m\ [\mu F/cm^2]$	1	1	1	1	1	1	1/17
$\rho_a\ [\Omega \cdot cm]$	150	150	150	150	150	150	150
$E_{pas}\ [mV]$	-70	-70	-70	-70	-70	-70	-70
$g_{Na1.2}\ [mS/cm^2]$	8	8	320	100	-	-	-
$g_{Na1.6}\ [mS/cm^2]$	10	10	-	320	300	160	-
$E_{Na}\ [mV]$	60	60	60	60	60	60	-
$g_{Kv}\ [mS/cm^2]$	-	-	100	100	150	-	-
$g_{Km}\ [mS/cm^2]$	0.03	0.03	-	-	-	-	-
$g_{KCa}\ [mS/cm^2]$	0.3	0.3	-	-	-	-	-
$E_K\ [mV]$	-90	-90	-90	-90	-90	-	-
$g_{Cav}\ [mS/cm^2]$	0.03	0.03					-
$E_{Ca}\ [mV]$	140	140	-	-	-	-	-
Geometry							
$L\ [\mu m]$	500	20	10	50*	200	1	100
$d\ [\mu m]$	5	20	3.1	1.22	1	1	1

Table 10: Electrophysiological and geometric properties of all models. Dend: dendrite, AH: axon hillock, Unmy: unmyelinated axon, Node: node of Ranvier, Intern: internode. Blue cells are for the *single section model*, with the exception of the length (*) $L = 100\ \mu m$ for the *single section model*. Orange cells are for the *axon model*. White, blue and orange cells are for the *standard 1D model*, while all cells are for the *extended 1D model*.

General parameters				Noise	
ρ_e $[\Omega \cdot cm]$	300	Number of pulses per simulation	10,000	μ	1
T [°C]	37	Distance between pulses $[ms]$	350	σ	1
Δt_1 $[ms]$	0.0025	Start noise before stimulus $[ms]$	3	k $[\mu A\ mS^{-1/2}]$	0.0038
Δt_2 $[ms]$	1	Noise duration $[ms]$	10		
Stimulus duration monophasic or biphasic per phase $[ms]$			0.1		

Table 11: General and noise parameters for all models.

References

Almog, M. & Korngreen, A., 2014. A quantitative description of dendritic conductances and its application to dendritic excitation in layer 5 pyramidal neurons. *The Journal of Neuroscience,* 34(1), pp. 182-196.

Bekkers, J. M., 2011. Pyramidal neurons. *Current Biology,* 21(24), p. R975.

Bitanihirwe, B. K. Y. & Woo, T.-U. W., 2021. Chapter 37 - Pyramidal neurons: physiology, pathophysiology, and postnatal development. In: C. R. Martin, V. R. Preedy & R. Rajendram, eds. *Factors affecting neurodevelopment.* s.l.:Academic Press, pp. 433-445.

Boinagrov, D. et al., 2012. Upper threshold of extracellular neural stimulation. *Journal of Neurophysiology,* 108(12), pp. 3233-3238.

Bolsover, S. R., Hyams, J. S., Shephard, H. A. W. & Wiedemann, C. G., 2003. The action potential. In: *Cell biology: a short course.* 2nd ed. Hoboken, New Jersey: John Wiley & Sons, Ltd, pp. 325-340.

Burian, I., 2017. *The upper threshold phenomenon in a pyramidal neuron simulated with a multicompartment model.* Master's thesis. Vienna University of Technology.

Carnevale, N. T. & Hines, M. L., 2006. *The NEURON book.* Cambridge: Cambridge University Press.

Destexhe, A., Babloyantz, A. & Sejnowski, T. J., 1993. Ionic mechanisms for intrinsic slow oscillations in thalamic relay neurons. *Biophysical Journal,* 65(4), pp. 1538-1552.

Destexhe, A., Mainen, Z. F. & Sejnowski, T. J., 1998. Kinetic models of synaptic transmission. In: C. Koch & I. Sagev, eds. *Methods in neuronal modeling: from ions to networks.* 2nd ed. Cambridge, MA: MIT Press, pp. 1-26.

Destexhe, A. & Paré, D., 1999. Impact of network activity on the integrative properties of neocortical pyramidal neurons in vivo. *Journal of Neurophysiology,* 81(4), pp. 1531-1547.

Destexhe, A., Rudolph, M. & Paré, D., 2003. The high-conductance state of neocortical neurons in vivo. *Nature Reviews. Neuroscience,* 4(9), pp. 739-751.

Dizdar, F., 2022. *Simulation of the dynamic range of retinal ganglion cells during microelectrode stimulation.* Unpublished master's thesis. Vienna University of Technology.

Fellner, A., 2017. *Modelling block of excitation of a retinal ganglion cell stimulated with microelectrodes using python and neuron.* Master's thesis. Vienna University of Technology.

Fellner, A., Heshmat, A., Werginz, P. & Rattay, F., 2022. A finite element method framework to model extracellular neural stimulation. *Journal of Neural Engineering,* 19(2), p. 022001.

Fellner, A., Stiennon, I. & Rattay, F., 2019. Analysis of upper threshold mechanisms of spherical neurons during extracellular stimulation. *Journal of Neurophysiology,* 121(4), pp. 1315-1328.

Fellous, J. M., Rudolph, M., Destexhe, A. & Sejnowski, T. J., 2003. Synaptic background noise controls the input/output characteristics of single cells in an in vitro model of in vivo activity. *Neuroscience,* 122(3), pp. 811-829.

Ferrante, M. A., 2018. Anatomy and physiology of neurons. In: *Comprehensive electromyography: with clinical correlations and case ctudies.* Cambridge: Cambridge University Press, pp. 49-67.

Foutz, T. J. & Wong, M., 2022. Brain stimulation treatments in epilepsy: basic mechanisms and clinical advances. *Biomedical Journal,* 45(1), pp. 27-37.

Fried, S. I. & Lee, S. W., 2016. Responses of L5 pyramidal neurons of V1 to electrical stimulation. *Investigative Ophthalmology & Visual Science,* 57(12), p. 5328.

Gustafsson, B. & Jankowska, E., 1976. Direct and indirect activation of nerve cells by electrical pulses applied extracellularly. *The Journal of Physiology,* 258(1), pp. 33-61.

Hamill, O. P., Huguenard, J. R. & Prince, D. A., 1991. Patch-clamp studies of voltage-gated currents in identified neurons of the rat cerebral cortex. *Cerebral Cortex,* 1(1), pp. 48-61.

Hines, M., Davison, A. & Muller, E., 2009. NEURON and Python. *Frontiers in Neuroinformatics,* 3(1).

Hines, M. L. & Carnevale, N. T., 1997. The NEURON simulation environment. *Neural Computation,* 9(6), pp. 1179-1209.

Hodgkin, A. L. & Huxley, A. F., 1952. A quantitative description of membrane current and its aplication to conduction and excitation in nerve. *The Journal of Physiology,* 117(4), pp. 500-544.

Huguenard, J. R., Hamill, O. P. & Prince, D. A., 1988. Developmental changes in Na+ conductances in rat neocortical neurons: appearance of a slowly inactivating component. *Journal of Neurophysiology,* 59(3), pp. 778-795.

Hu, W. et al., 2009. Distinct contributions of Na(v)1.6 and Na(v)1.2 in action potential initiation and backpropagation. *Nature Neuroscience,* 12(8), pp. 996-1002.

Kaniusas, E., 2012. *Biomedical signals and sensors I: linking physiological phenomena and biosignals.* Berlin, Heidelberg: Springer.

Keren, N., Bar-Yehuda, D. & Korngreen, A., 2009. Experimentally guided modelling of dendritic excitability in rat neocortical pyramidal neurones. *The Journal of Physiology,* 587(7), pp. 1413-1437.

Keren, N., Peled, N. & Korngreen, A., 2005. Constraining compartmental models using multiple voltage recordings and genetic algorithms. *Journal of Neurophysiology,* 94(6), p. 3730–3742.

Khubieh, A., Ratté, S., Lankarany, M. & Prescott, S. A., 2016. Regulation of cortical dynamic range by background synaptic noise and feedforward inhibition. *Cerebral Cortex,* 26(8), p. 3357–3369.

Komarov, M. et al., 2019. Selective recruitment of cortical neurons by electrical stimulation. *PLoS Computational Biology,* 15(8), p. e1007277.

LaBerge, D., 2005. Sustained attention and apical dendrite activity in recurrent circuits. *Brain Research Reviews,* 50(1), pp. 86-99.

Lecar, H. & Nossal, R., 1971. Theory of threshold fluctuations in nerves. I. Relationships between electrical noise and fluctuations in axon firing. *Biophysical Journal,* 11(12), pp. 1048-1067.

Liu, X. et al., 2022. A narrative review of cortical visual prosthesis systems: the latest progress and significance of nanotechnology for the future. *Annals of Translational Medicine,* 10(12), p. 716.

Madugula, S. S. et al., 2022. Inference of electrical stimulation sensitivity from recorded activity of primate retinal ganglion cells. *BioRxiv.*

Mainen, Z. F., Jeorges, J., Huguenard, J. R. & Sejnowski, T. J., 1995. A model of spike initiation in neocortical pyramidal neurons. *Neuron,* 15(6), pp. 1427-1439.

Mainen, Z. F. & Sejnowski, T. J., 1996. Influence of dendritic structure on firing pattern in model neocortical neurons. *Nature,* 382(6589), pp. 363-366.

Meng, K. et al., 2018. Upper stimulation threshold for retinal ganglion cell activation. *Journal of Neural Engineering,* 15(4), p. 046012.

National Institute of Neurological Disorders and Stroke, n.d. *National Institute of Neurological Disorders and Stroke.* [Online] Available at: https://www.ninds.nih.gov/health-information/public-education/brain-basics/brain-basics-know-your-brain
[Accessed 5 11 2022].

Pennefather, P., Sala, F. & Hernandez-cruz, A., 1990. A computer simulation of IAHP kinetics. *Abstr Soc Neurosci,* Volume 10, p. 10.

Purves, D. et al. eds., 2005. *Neuroscience.* 3rd ed. Sunderland, MA: Sinauer Associates.

Radivojevic, M. et al., 2016. Electrical identification and selective microstimulation of neuronal compartments based on features of extracellular action potentials. *Scientific Reports,* Volume 6, p. 31332.

Ranck, J. B., 1975. Which elements are excited in electrical stimulation of mammalian central nervous system: a review. *Brain Research,* 98(3), pp. 417-440.

Rattay, F., 1987. Ways to approximate current-distance relations for electrically stimulated fibers. *Journal of Theoretical Biology,* 125(3), pp. 339-349.

Rattay, F., 1990. *Electrical nerve stimulation: Theory, experiments and applications.* Vienna: Springer.

Rattay, F., 2000. Basics of hearing theory and noise in cochlear implants. *Chaos, Solitons & Fractals,* 11(12), pp. 1875-1884.

Rattay, F., 2014. On the upper threshold phenomenon of extracellular neural stimulation. *Journal of Neurophysiology,* 112(10), pp. 2664-2665.

Rattay, F., Bassereh, H. & Fellner, A., 2017. Impact of electrode position on the elicitation of sodium spikes in retinal bipolar cells. *Scientific Reports,* 7(1), p. 17590.

Rattay, F., Greenberg, R. J. & Resatz, S., 2003. Neuron modeling. In: W. E. Finn & P. G. LoPresti, eds. *Handbook of neuroprosthetic methods.* s.l.:CRC Press, pp. 39-71.

Rattay, F., Lutter, P. & Felix, H., 2001. A model of the electrically excited human cochlear neuron: I. Contribution of neural substructures to the generation and propagation of spikes. *Hearing Research,* 153(1-2), pp. 43-63.

Rattay, F., Paredes, L. P. & Leao, R. N., 2012. Strength–duration relationship for intra- versus extracellular stimulation with microelectrodes. *Neuroscience,* Volume 214, pp. 1-13.

Rattay, F. & Tanzer, T., 2022a. Impact of electrode position on the dynamic range of a human auditory nerve fiber. *Journal of Neural Engineering,* Volume 19, p. 016025.

Rattay, F. & Tanzer, T., 2022b. A simple model considering spiking probability during extracellular axon stimulation. *PLoS One,* 17(4), p. e0264735.

Rattay, F. & Wenger, C., 2010. Which elements of the mammalian central nervous system are excited by low current stimulation with microelectrodes?. *Neuroscience,* 170(2), pp. 399-407.

Reuveni, I., Friedman, A., Amitai, Y. & Gutnick, M. J., 1993. Stepwise repolarization from Ca2+ plateaus in neocortical pyramidal cells: evidence for nonhomogeneous distribution of HVA Ca2+ channels in dendrites. *The Journal of Neuroscience,* 13(11), pp. 4609-4621.

Royeck, M. et al., 2008. Role of axonal NaV1.6 sodium channels in action potential initiation of CA1 pyramidal neurons. *Journal of Neurophysiology,* 100(4), p. 2361–2380.

Rubinstein, J. T., 1995. Threshold fluctuations in an N sodium channel model of the node of Ranvier. *Biophysical Journal,* 68(3), pp. 779-785.

Rush, A. M., Dib-Hajj, S. D. & Waxman, S. G., 2005. Electrophysiological properties of two axonal sodium channels, Nav1.2 and Nav1.6, expressed in mouse spinal sensory neurones. *The Journal of Physiology,* 564(3), pp. 803-815.

Sajedi, S., Fellner, A., Werginz, P. & Rattay, F., 2021. Block phenomena during electric micro-stimulation of pyramidal cells and retinal ganglion cells. *Frontiers in Cellular Neuroscience,* Volume 15, p. 771600.

Shepherd, R. K. & Javel, E., 1997. Electrical stimulation of the auditory nerve. I. Correlation of physiological responses with cochlear status. *Hearing Research,* 108(1-2), pp. 112-144.

Summers, J. J., Kang, N. & Cauraugh, J. H., 2016. Does transcranial direct current stimulation enhance cognitive and motor functions in the ageing brain? A systematic review and meta- analysis. *Ageing Research Reviews,* Volume 25, pp. 42-54.

Tandon, P. et al., 2021. Automatic identification of axon bundle activation for epiretinal prosthesis. *IEEE Transactions on Neural Systems and Rehabilitation Engineering,* Volume 29, p. 2496–2502.

Valverde, S. et al., 2020. Deep brain stimulation-guided optogenetic rescue of parkinsonian symptoms. *Nature Communications,* 11(1), p. 2388.

Verveen, A. A., 1960. On the fluctuation of threshold of the nerve fibre. *Structure and Function of the Cerebral Cortex,* pp. 282-288.

Verveen, A. A., 1962. Axon diameter and fluctuation in excitability. *Acta Morphologica Neerlando-Scandinavica,* 5(1), pp. 79-85.

Verveen, A. A. & Derksen, H. E., 1968. Fluctuation phenomena in nerve membrane. *Proceedings of the IEEE,* 56(6), pp. 906-916.

Werginz, P., Raghuram, V. & Fried, S. I., 2020. The relationship between morphological properties and thresholds to extracellular electric stimulation in α RGCs. *Journal of Neural Engineering,* Volume 17, p. 045015.

White, J. A., Rubinstein, J. T. & Kay, A. R., 2000. Channel noise in neurons. *Trends in Neurosciences,* 23(3), pp. 131-137.

Yamada, W. M., Koch, C. & Adams, P. R., 1998. Multiple channels and calcium dynamics. In: C. Koch & I. Sagev, eds. *Methods in neuronal modeling: from ions to networks.* 2nd ed. Cambridge, MA: MIT Press, pp. 137-170.

Yi, G. S., Wang, J., Deng, B. & Wei, X. L., 2017. Morphology controls how hippocampal CA1 pyramidal neuron responds to uniform electric fields: a biophysical modeling study. *Scientific Reports,* 7(1), p. 3210.